OPTICAL CLASSIFICATION AND RECONSTRUCTION THROUGH
MULTIMODE FIBERS

A THESIS SUBMITTED TO
THE GRADUATE SCHOOL OF NATURAL AND APPLIED SCIENCES
OF
MIDDLE EAST TECHNICAL UNIVERSITY

BY

ŞAHIN KÜREKCI

IN PARTIAL FULFILLMENT OF THE REQUIREMENTS
FOR
THE DEGREE OF DOCTOR OF PHILOSOPHY
IN
PHYSICS

DECEMBER 2022

Approval of the thesis:

OPTICAL CLASSIFICATION AND RECONSTRUCTION THROUGH MULTIMODE FIBERS

submitted by **ŞAHIN KÜREKCI** in partial fulfillment of the requirements for the degree of **Doctor of Philosophy in Physics Department, Middle East Technical University** by,

Prof. Dr. Halil Kalıpçılar
Dean, Graduate School of **Natural and Applied Sciences**   ——————

Prof. Dr. Seçkin Kürkçüoğlu
Head of Department, **Physics**   ——————

Assoc. Prof. Dr. Emre Yüce
Supervisor, **Physics, METU**   ——————

Examining Committee Members:

Prof. Dr. Alpan Bek
Physics, METU   ——————

Assoc. Prof. Dr. Emre Yüce
Physics, METU   ——————

Prof. Dr. İsa Navruz
Electrical and Electronics Engineering, Ankara University   ——————

Prof. Dr. Mehmet Emre Taşgın
Institute of Nuclear Sciences, Hacettepe University   ——————

Assoc. Prof. Dr. Serdar Kocaman
Electrical and Electronics Engineering, METU   ——————

Date: 06.12.2022

I hereby declare that all information in this document has been obtained and presented in accordance with academic rules and ethical conduct. I also declare that, as required by these rules and conduct, I have fully cited and referenced all material and results that are not original to this work.

Name, Surname: Şahin Kürekci

Signature   :

ABSTRACT

**OPTICAL CLASSIFICATION AND RECONSTRUCTION THROUGH
MULTIMODE FIBERS**

Kürekci, Şahin

Ph.D., Department of Physics

Supervisor: Assoc. Prof. Dr. Emre Yüce

December 2022, 116 pages

When a light beam travels through a highly scattering medium, two-dimensional random intensity distributions (speckle patterns) are formed due to the complex scattering within the medium. Although they contain valuable information about the input signal and the characteristics of the propagation medium, the speckle patterns are difficult to unscramble, which makes imaging through scattering media an extremely challenging task. Multimode fibers behave similarly to scattering media since they scramble the input information through modal dispersion and create speckle patterns at the distal end. Because multimode fibers are compact and low-cost structures with the ability to transmit large amounts of data simultaneously for long distances, decoding the speckle patterns formed by a multimode fiber and reconstructing the input information has great implications in a wide range of applications, including fiber optic communication, sensor technology, optical imaging, and invasive biomedical applications such as endoscopy. In this thesis, we decode the speckle patterns and reconstruct the input information on the proximal end of a multimode fiber in three different scenarios. Our choice of input signals consists of numbers encoded as binary digits, handwritten letters, and optical frequencies. We train a deep learning model to classify

and reconstruct the handwritten letters, while for the rest of the cases, we construct a transmission matrix between the input signals and the output speckle patterns, and solve the inverse propagation equation algebraically. In all cases, the relation between a speckle pattern and the corresponding input signal is learned with low error rates; thus, the signals are classified and reconstructed successfully using the speckle patterns they created. Classifying digits, letters, or images with speckle information aims to build useful systems in optical imaging, communication, and cryptography, while the classification of optical frequencies paves the way for building novel spectrometers. In addition to replicating the currently existing compact, low-budget, and high-resolution multimode fiber spectrometer, we also build a single-pixel fiber spectrometer in order to increase the compactness on the detection side and expand the application areas of the system. The single-pixel spectrometer we offer is based on the integrated intensity measurements of a fixed target region, where the light is focused by shaping the wavefront with a spatial light modulator. Spatial light modulators and wavefront shaping techniques are also utilized in other classification tasks in this thesis to generate the desired input signals.

Keywords: fiber optics, multimode fibers, speckle pattern, propagation, imaging, classification, reconstruction, wavefront shaping, spatial light modulator, cryptography, encryption, deep learning, neural networks, spectrometer, single-pixel, high resolution

ÖZ

ÇOK MODLU FİBERLER ÜZERİNDEN OPTİK SINIFLANDIRMA VE YENİDEN OLUŞTURMA

Kürekci, Şahin

Doktora, Fizik Bölümü

Tez Yöneticisi: Doç. Dr. Emre Yüce

Bir ışık demeti yüksek saçıcılık özelliklerine sahip bir ortamdan geçtiğinde, ortam içerisindeki karmaşık saçıcılıktan ötürü iki boyutlu düzensiz şiddet dağılımları (benek desenleri) oluşur. Giriş sinyali ve yayılma ortamının karakteristiği hakkında değerli bilgiler içermelerine rağmen benek desenlerini çözümlemenin zor olması saçıcı ortam üzerinden görüntülemeyi oldukça zorlayıcı bir hâle getirir. Kipsel dağılım yoluyla girişteki bilgiyi karıştırmaları ve uzak uçta benek desenleri yaratmaları sebebiyle çok modlu fiberler de saçıcı ortamlara benzer davranışlar gösterirler. Çok modlu fiberlerin büyük miktarda veriyi eşzamanlı olarak uzun mesafeler boyunca iletme yeteneğine sahip kompakt ve düşük maliyetli yapılar olmaları sebebiyle, bir çok modlu fiber tarafından yaratılan benek desenini çözümlemenin ve girişteki bilgiyi tekrar oluşturmanın fiber optik iletişim, sensör teknolojisi, optik görüntüleme ve endoskopi gibi invazif biyomedikal uygulamaları içeren geniş uygulama alanlarına büyük etkileri vardır. Bu tez çalışmasında, benek desenlerini çözümlüyoruz ve bir çok modlu fiberin yakın ucundaki giriş bilgisini üç farklı senaryoda yeniden oluşturuyoruz. Giriş sinyallerimiz ikili rakamlar şeklinde kodlanmış sayıları, el yazısıyla yazılmış harfleri ve optik frekansları

içeriyor. El yazısıyla yazılmış harfleri sınıflandırmak ve yeniden oluşturmak için bir derin öğrenme modeli eğitirken diğer durumlar için girişteki sinyalleri ve çıkıştaki benekli desenleri birbiriyle ilişkilendiren bir iletim matrisi oluşturarak ters yayılım problemini cebirsel olarak çözdük. Tüm durumlarda benek deseni ile o desene ait giriş sinyali arasındaki ilişki düşük hata oranlarıyla öğrenildi, dolayısıyla sinyaller kendileri tarafından oluşturulan benek desenleri kullanılarak başarılı bir şekilde sınıflandırıldı ve yeniden oluşturuldu. Rakamları, harfleri ya da görüntüleri benek deseni bilgisi ile sınıflandırmak optik görüntülemede, optik iletişimde ve kriptografide faydalı olabilecek sistemler inşa etmeyi amaçlamaktayken optik frekansların sınıflandırılması ise özgün spektrometreler inşa etmenin önünü açmaktadır. Halihazırda mevcut olan kompakt, düşük bütçeli ve yüksek çözünürlüklü çok modlu fiber spektrometreyi tekrarlamanın yanı sıra, algılama tarafındaki kompaktlığı artırmak ve sistemin uygulama alanlarını genişletmek amacıyla tek pikselli bir fiber spektrometre inşa ediyoruz. Sunduğumuz tek pikselli spektrometre, dalga önünü uzaysal bir ışık modülatörü ile şekillendirerek ışığın odaklandığı sabit bir hedef bölgenin entegre yoğunluk ölçümlerine dayanmaktadır. Uzaysal ışık modülatörleri ve dalga önü şekillendirme teknikleri, istenen giriş sinyallerini oluşturmak için bu tezdeki diğer sınıflandırma çalışmalarında da kullanılmıştır.

Anahtar Kelimeler: fiber optik, çok modlu fiber, benek deseni, yayılma, görüntüleme, sınıflandırma, yeniden yapılandırma, dalga önü şekillendirme, uzaysal ışık modülatörü, kriptografi, şifreleme, derin öğrenme, sinir ağları, spektrometre, tek piksek, yüksek çözünürlük

> *Muvaffakiyet biliyorsunuz ki teşebbüsün başlangıcıyla oluyor. Bir teşebbüs edin bakalım...*
>
> — Öztürk Serengil [1933-1999]

> *Yolu yürümeye başlarsan yol kendini gösterir.*
>
> — Mevlânâ Celâleddîn-i Rûmî [1207-1273]

Öztürk Serengil was born 660 years after Mevlânâ Celâleddîn-i Rûmî's death. They both lived 66 years.

ACKNOWLEDGMENTS

I have benefited greatly from working as a member of a group during my Ph.D. I learned a lot from my group members, both during and outside the group meetings, and that had great returns for my career and personal development. I am highly grateful to Elif Cemre Yiğit and Deniz Bender for proofreading this thesis and for their great efforts to overcome the intensity I experienced in the last couple of months. I would like to thank the current members of our group Berk Nezir Gün, Parisa Naghinazhad, Ahmet Azgın, Zafer Çılgın, Sena Atila, Anıl Jean Pekgöz, and former members Dr. Âlim Yolalmaz, Mustafa Safa Dal, Çağdaş Anıl Yüksel, Yalın Başay, Halil İbrahim Binici for their support, fruitful discussions, and helpful comments.

I would like to thank Fırat Yalçın, Gözdenur Toraman, Âlim Yolalmaz, Berk Nezir Gün, Aydın Emiraghbali, Gilda Afshari, Berk Berkan Turgut, Çağdaş Anıl Yüksel, Ali Murat Sözen, Tuğba Andaç, Kamran Allahverdiyev, Kutlu Kağan Türkarslan, Suat İçli, Mustafa Safa Dal, Yalın Başay, Özge Demirtaş, Hüseyin Tepe, Sedanur Toraman, Yasemin Özmen, Özden Başar Balbaşı, Göksu Okar, Kemal Oktay Balıkçı, Dilek Kızılören (*and Damla*), Namig Alasgarzade, Adem Emre Karaoğuz, Mustafa Elçi, Mehmet Enes Tolgay for their friendship and support. With most of the people in this list, we have spent pleasant moments in *SOBİ* as members of *ODTÜ Food Club*. I have shared some great moments of my life with these great people, and their contribution to my life is priceless.

I would like to thank my family for their support. I have not been able to devote enough time to them in the last six years. I hope I will have the opportunity to close this gap from now on.

Lastly, I would like to thank *her* for being part of my life with her endless love, endless patience, and endless support. I love her three thousand!

TABLE OF CONTENTS

LIST OF TABLES

TABLES

xxii

LIST OF ABBREVIATIONS

SMF	Single-Mode Fiber
MMF	Multimode Fiber
WFS	Wavefront Shaping
SLM	Spatial Light Modulator
DMD	Digital Micromirror Device
LP	Linearly Polarized
PBR	Peak-to-Background Ratio
CCD	Charge Coupled Device
FPA	Focal Plane Array
SNR	Signal-to-Noise Ratio
FWHM	Full-Width at Half-Maximum
RMSE	Root-Mean-Square Error

CHAPTER 1

INTRODUCTION

1.1   Motivation and Problem Definition

Although we are often not consciously aware of them, there are several important concepts and equations that govern our lives. "Propagation" is one of these concepts, and it is described by the propagation equation

$$y = \mathrm{T} * x, \tag{1.1}$$

where x is the input information, y is the output information, T is the propagation medium, and $*$ denotes multiplication. A general diagram of propagation is shown in Fig. 1.1, where the sender and the receiver are named Alice and Bob.
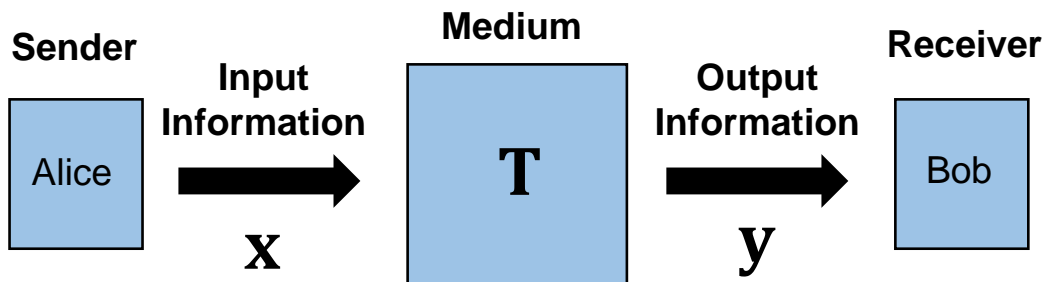
Figure 1.1: A general diagram describing propagation. The input information x is sent by the sender, Alice, and after propagating through medium T, the output information is read as y by the receiver, Bob. The input and output information might be different due to noise gained by propagation in the medium.

Many daily life phenomena can be explained by the propagation equation, including communication and vision. In the case of oral communication, the sound is propagated through the air, and vibrations of air molecules transmit the words to the receiver. In online communication, the input information is sent as digital signals from data centers to our computers with optical fibers. We can see the world thanks to the light reflected from the objects and propagated to our eyes. However, most of the time, the propagation of information from one point to another is not perfect. The information gains noise due to the propagation medium, and this results in the difference between the input information x and the output information y, e.g., it is highly possible for a receiver to hear something else than what we actually speak in a noisy environment. The rate of difference between x and y depends on the propagation medium as well as the input information itself. In general, the input information can be recovered at the receiver side with high accuracy if it is sent with an amplitude higher than the amplitude of the noise gained during propagation.

In this thesis, we will concentrate on the propagation of light (electromagnetic waves) in a multimode fiber. Electromagnetic waves are used almost in all parts of modern communication and technology for information transfer, imaging, health, and security purposes. In general terms, electromagnetic waves travel undistorted, almost along straight lines, in free space, as shown in Fig. 1.2(a). Any medium allowing the light to propagate undistorted (such as air and glass) seems transparent to the human eye; hence an object behind them is clearly visible. However, in our daily life, we also encounter a lot of opaque (non-transparent, complex, or disordered) media. Clear imaging across an opaque media is not possible due to complex interactions of light and matter, known as the scattering of light (scattering of light can be considered as the total effect of reflections, refractions, and diffractions of light from microscopic small particles inside the material). Interaction of light with such disordered media results in a random intensity distribution, known as speckle pattern, instead of a clear image of the light source, as shown in Fig. 1.2(b).
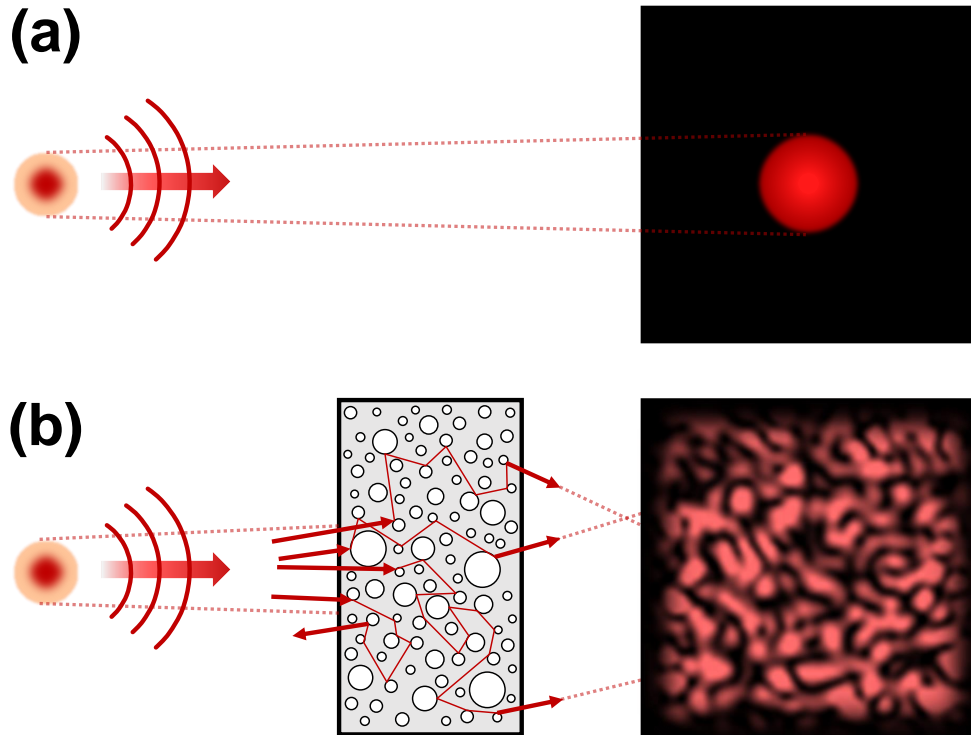
Figure 1.2: Interaction of light with matter. **(a)** A light source in free space travels undistorted and follows an almost straight line to form a sharp image of the light source. **(b)** The same light source creates a speckle pattern when it encounters a complex, disordered material due to the multiple scattering inside the medium.

Clearly, scattering of light is a very fundamental limitation for optical imaging across complex disordered media since all the input information is transformed into a random speckle image. Still, increasing the imaging quality across scattering media or recovering images behind them is highly desirable since such media are commonly encountered in daily life, as shown in Fig. 1.3. Increasing the visibility across fog, mist, and clouds can reduce traffic risks, and similarly, increasing the imaging quality across biological tissue can be useful in the biomedical diagnosis and treatment [1]. Due to its significance in so many various areas, multiple light scattering has been widely studied in numerous works in the past decades [2–24]. The unending popularity of these studies is based on the fact that although the speckle patterns are highly disordered intensity distributions, multiple scattering itself is a deterministic process, and it can be described with the principles of wave diffusion theories, thus using Maxwell's equations [6].
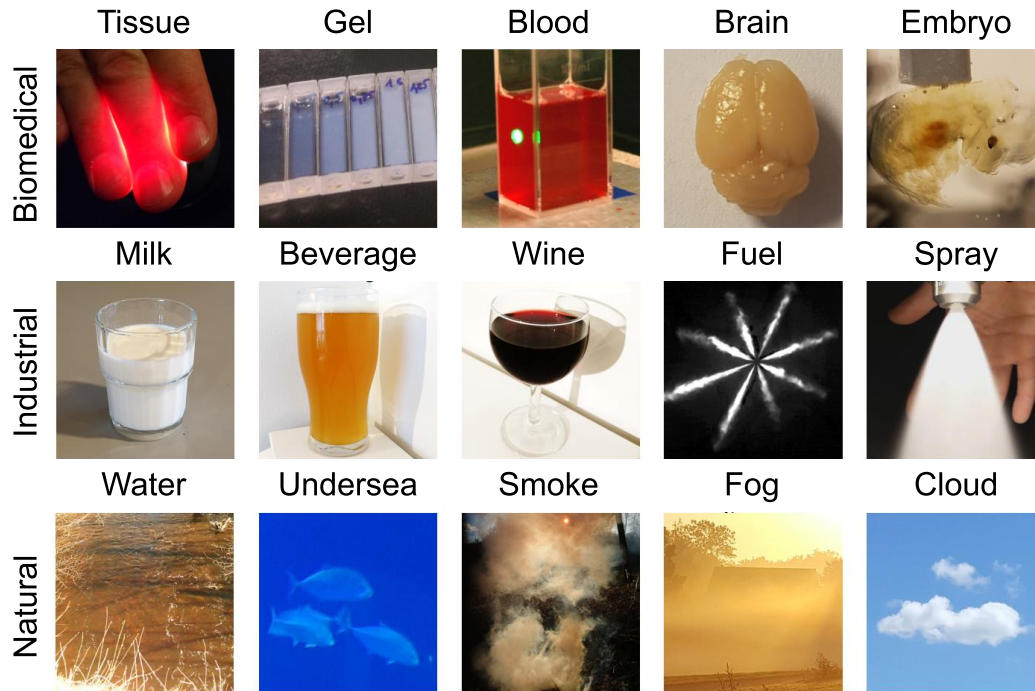
Figure 1.3: Examples of scattering media in daily life. Despite the existence of scattering media in all areas of life, detailed optical examinations are difficult since they scatter light and form a speckle pattern. The figure is adapted from [1].

Multimode fibers behave similarly to scattering media in several aspects. The light coupled to a multimode fiber is carried to the other end of the fiber with total internal reflections, and a speckle pattern is observed. Compared to ordinary scattering media, multimode fibers possess lower losses since they prevent the scattering of light to high angles. However, in most applications, single-mode fibers are preferred instead of multimode fibers due to the speckle pattern formation, i.e., information loss, exhibited by multimode fibers. Although current applications of multimode fibers are limited due to speckle formation, there is a great effort for their implementation in optical fiber systems for several reasons. Three of these reasons can be listed as follows:

1. In single-mode fibers, the amount of information that can be transmitted simultaneously is restricted to one channel. However, multimode fibers have multiple channels to carry information; hence they allow parallel transmission. This property of multimode fibers allows carrying larger data simultaneously and can revolutionize telecommunication and biomedicine applications.

2. Although single-mode fibers are compact structures with sizes around 9 μm, for most practical applications, bundles (collection) of single-mode fibers are used to carry signals in order to transmit larger data. The size of single-mode fiber bundles generally reaches millimeters thickness. The same tasks can be done with a single multimode fiber whose thickness is around 50-100 μm. Thus, multimode fibers can offer more compact solutions for current optical fiber systems.

3. The speckle patterns created by the multimode fibers resemble multiple scattering from a scattering media. Therefore, studying multimode fibers is insightful for applications involving scattering media similar to the ones listed in Fig. 1.3.

In order to properly investigate the multimode fibers (or any other scattering medium) and use them in imaging applications, the scattering properties of the medium need to be understood or controlled. Wavefront shaping is a powerful method developed for controlling light propagation in scattering media [25–58]. The basic principle of the wavefront shaping method is to utilize modulators to change the phase (or the amplitude) of the incident light. The control over the phase of the light leads to striking applications such as the optimization of light across scattering media (see Fig. 1.4). Thus, the scattering medium is forced to act as a focusing lens and safely transmits the signal to the other side instead of scrambling it into a speckle pattern.

Our purpose in this thesis is to classify and reconstruct different types of spatial and spectral information traveled across a multimode fiber using wavefront shaping methods (see Fig. 1.5). Classification can be described as identifying and grouping similar objects (or signals), and reconstruction is the task of rebuilding the actual input information which gained noise during the propagation. For both classification and reconstruction tasks, the propagation of the information from one end to the other needs to be handled carefully, and the propagation medium (or part of it that will be useful for the current task) needs to be learned. We develop methods to statistically or algebraically learn the propagation medium T for specific tasks and then reconstruct the input information x by inverting Eq. (1.1),

$$x = \mathrm{T}^{-1} * y. \tag{1.2}$$
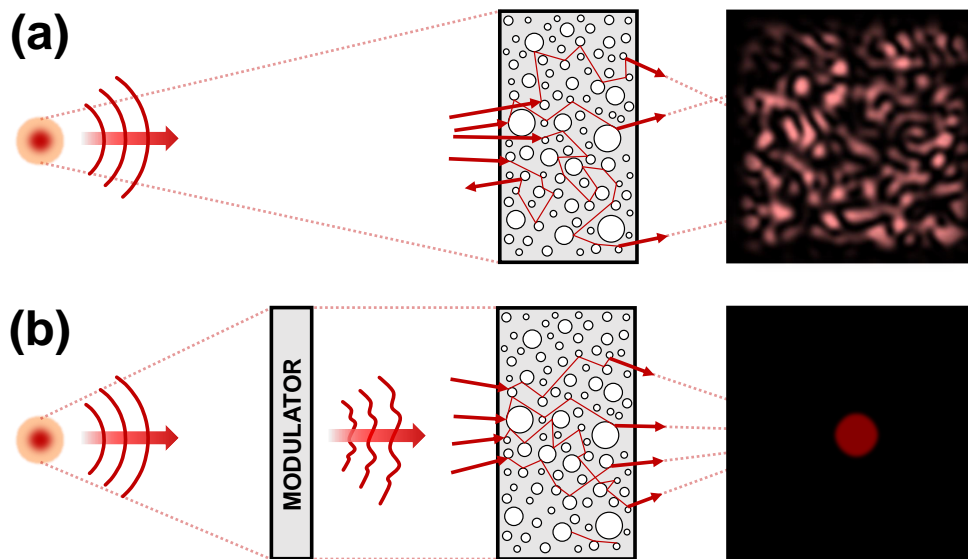
Figure 1.4: Demonstration of wavefront shaping across a scattering medium. **(a)** The light incident on a scattering medium undergoes multiple scatterings and creates a speckle pattern. All information on the input of the scattering medium is lost in this process. **(b)** The scattering of light can be controlled by shaping the wavefront with a modulator. In this case, light can be focused across the medium, and the input information can be carried safely.
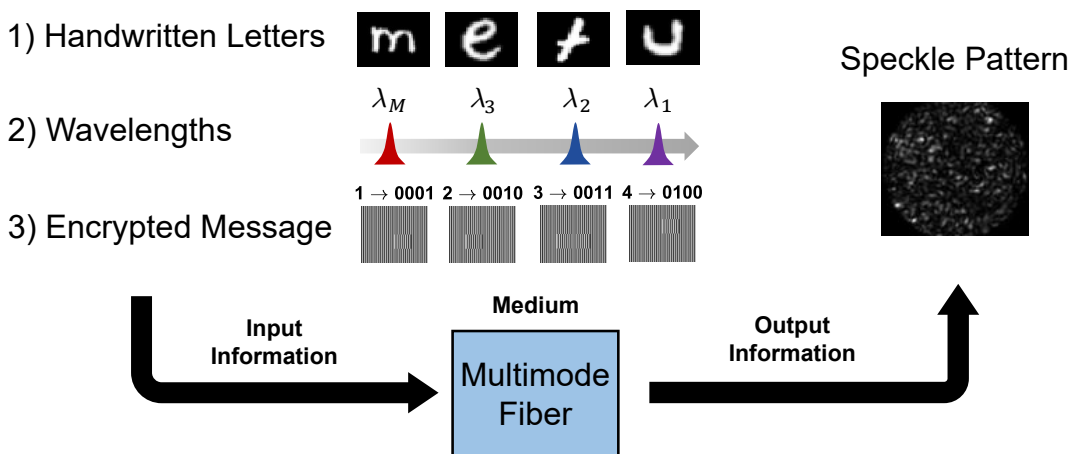
Figure 1.5: Visual outline of the thesis. By using the speckle patterns formed at the distal end, we classify and reconstruct different types of input information (spatial and spectral signals) transmitted through multimode fibers.

1.2 Contributions and Novelties

Our contributions in the context of this thesis are as follows:

- **S. Kürekci**, S. S. Kahraman, and E. Yüce, "Single-Pixel Multimode Fiber Spectrometer via Wavefront Shaping," arXiv.2210.13292 [Preprint]

- **S. Kürekci**, A. T. Temür, M. E. Odabas, G. Afshari, and E. Yüce, "Deep learning-based image transmission through a multi-mode fiber," Proc. SPIE 11351, Unconventional Optical Imaging II, 1135126 (2020)

- E. Yüce, and **S. Kürekci**, "Interference-based spectrometer with multimode medium," (Pending-patent, International application number: PCT/TR2021/051305)

- E. Yüce, and **S. Kürekci**, "Compact Holographic SLM Spectrometer," (Pending-patent, Turkish Patent and Trademark Office application number: 2020/22701. International application number: PCT/TR2021/051613)

1.3 The Outline of the Thesis

In Chapter 2, we review the theory of optical fibers, introduce key fiber parameters, and investigate light propagation inside multimode fibers. The formation of speckles is explained in this chapter with various examples.

In Chapter 3, we introduce the experimental setup and methods applied during the thesis. We explain the details of spatial light modulators and introduce two algorithms to focus light across a multimode fiber.

In Chapter 4, we show the first demonstration of the use of a multimode fiber in a classification task where we classify digits between 1-9 by observing the corresponding speckle patterns.

In Chapter 5, we show image classification and reconstruction through a multimode fiber by training a deep neural network. We compare the performance of three con-

volutional neural network architectures in terms of prediction accuracy and training time.

In Chapter 6, we introduce a high-resolution low-loss multimode fiber spectrometer. We use speckles captured for different wavelengths to construct a calibration set, and test the reconstruction ability of the spectrometer by simulating various light sources.

In Chapter 7, we show that a multimode fiber can also be used to build a single-pixel spectrometer. Here, the light is focused on a chosen target point at the distal end of the fiber, and the integrated intensity of the target region is used to reconstruct the unknown input spectra.

In Chapter 8, we give a brief summary and make concluding remarks.

CHAPTER 2

OPTICAL FIBER THEORY

In this chapter, we review the theory of step-index optical fibers and light propagation inside multimode fibers. We start with the geometry of an optical fiber and explain critical fiber parameters such as the acceptance angle, the numerical aperture, and the V number. We then attempt to solve Maxwell's equations to investigate light propagation. Depending on the geometrical parameters of the fiber, the wavelength of the input light, and the boundary conditions, Maxwell's equations may have many solutions, which are called modes of the fiber. A field entering the fiber is decomposed into the modes and carried to the other end of the fiber. Since each mode has a distinct propagation constant (modal dispersion), the transmitted light forms random intensity distributions (speckle patterns) at the other end of the fiber. We conclude the chapter by simulating the formation of a speckle pattern with the transmission of an image through a step-index multimode fiber. Unless stated otherwise, the same fiber parameters (core size = 105 μm, core refractive index = 1.463, cladding refractive index = 1.446) and the same input wavelength (λ = 1550 nm) are used in all simulation results and visualizations presented throughout the thesis.

2.1 Geometry of a Step-Index Optical Fiber

Optical fibers are useful tools for many areas of science, engineering, and biomedicine, with applications in optical trapping [59–61], fiber laser technology [62–65], fiber interferometers and sensors [66–73], optical fiber telecommunication [74–80], health monitoring sensors [81–89], and endoscopy [90–95]. Fig. 2.1 shows the simple geometry of a step-index optical fiber where a high-index core region is surrounded by a low-index cladding and a jacket. The geometrical relations in this section can be understood more clearly by using the ray model of light, but we will switch to the wave model in Section 2.2 when studying the mode profiles of the fiber.
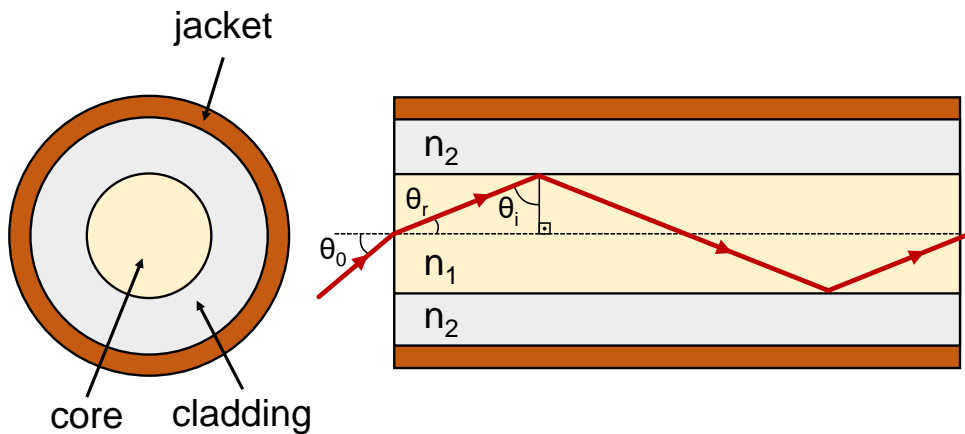
Figure 2.1: Geometry of a step-index optical fiber. A core region with refractive index n_1 is surrounded by a lower-index cladding region, $n_2 < n_1$. The refractive indices of core and cladding regions are adjusted for the optimal propagation of light by total internal reflections.

When light is coupled to the optical fiber, it propagates in the core region by undergoing successive total internal reflections at the core-cladding boundary. Thus, the light is *guided* inside the core region and cladding is responsible for the confinement of the light inside the core. The outermost jacket of the fiber is used to protect the inner part of the fiber and is generally made of plastic.

For total internal reflection (hence the propagation of light) to take place inside a step-index optical fiber, the refractive index of the core, n_1, has to be greater than that of the cladding, n_2. Applying Snell's law at the core-cladding boundary also requires

10

the angle θ_i to be greater than the critical angle,

$$\theta_i^{\min} = \theta_c = \arcsin(n_2/n_1). \tag{2.1}$$

The propagation condition (total internal reflection) brings additional restrictions on the coupling of light into the fiber. If the medium surrounding the fiber has refractive index n_0, Snell's law applied on the fiber boundary requires $\sin\theta_0 = (n_1/n_0)\sin\theta_r$. Using the geometrical relations between the angles θ_r and θ_i together with Eq. (2.1) yields

$$\theta_a = \theta_0^{\max} = \arcsin\left(\frac{1}{n_0}\sqrt{n_1^2 - n_2^2}\right), \tag{2.2}$$

where θ_a is the maximum entrance angle, called **acceptance angle**. An optical beam entering the fiber at an angle smaller than the acceptance angle can be guided fully through the optical fiber, i.e., it propagates inside the fiber by undergoing total internal reflections. For the light rays whose entrance angle θ_0 is greater than the acceptance angle θ_a, the light will not be guided inside the core region of the fiber but will be refracted into the cladding. These rays can travel inside the cladding for very short distances, and they do not contribute to the guided light inside the core. In a fiber coupling where most of the beam enters the light at angles higher than θ_a, higher losses occur in the transmitted intensity, and thus only partial transmittance of light is expected. Figure 2.2 shows the amount of power coupled to a 105 μm diameter fiber ($n_{\text{core}} = 1.463$, $n_{\text{clad}} = 1.446$) as a function of entrance angle for a plane wave of 1550 nm wavelength. For the chosen fiber parameters, the acceptance angle is $12.9°$, and only %10 percent of the light can couple into the fiber at the acceptance angle.

Although the acceptance angle is a good indicator of how well the light is coupled into the optical fiber, a more common figure of merit to describe the light-gathering capacity of the fiber is **numerical aperture**,

$$\text{NA} = n_0 \sin\theta_a = \sqrt{n_1^2 - n_2^2}. \tag{2.3}$$

Unlike the acceptance angle, the numerical aperture is independent of the refractive index of the outer region, n_0, and a more definitive parameter for the fiber geometry. A fiber with a high numerical aperture accepts more light from the source; thus, more power can be transferred through the fiber. For efficient coupling of light into the fiber,

the NA of the focusing lens (the lens used to couple light into the fiber) should be equal or close to the NA of the fiber.
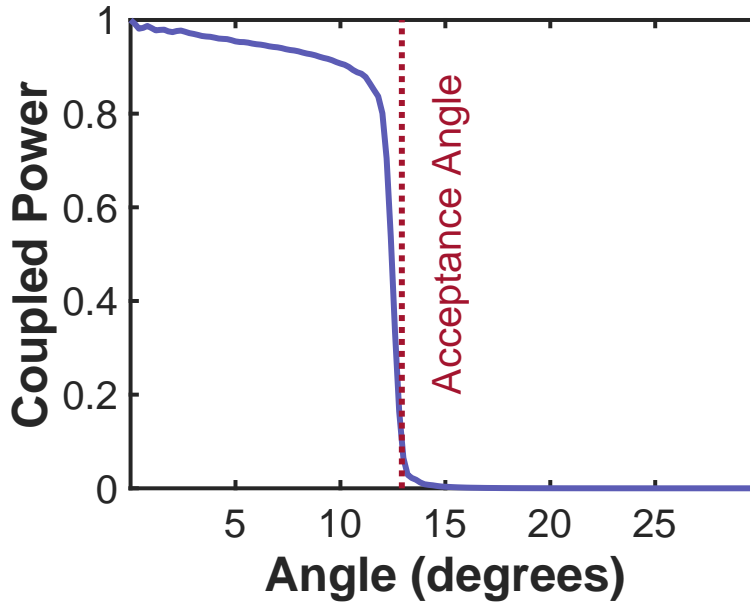
Figure 2.2: Amount of light power coupled into a 105 μm core diameter fiber as a function of entrance angle. The incident light is assumed to be a plane wave with 1550 nm wavelength. The acceptance angle, $12.9°$, is also shown on the graph with the brown dashed line.

The numerical aperture is an important parameter related to the geometry of the fiber, but it does not tell much about the propagation of light inside the fiber unless the wavelength of the light and the core size of the fiber are given. Having the wavelength λ, and core radius a, a new parameter called **V-number** (also known as waveguide parameter, or normalized frequency) can be derived,

$$V = \frac{2\pi a}{\lambda}\, \text{NA} = \frac{2\pi a}{\lambda}\sqrt{n_1^2 - n_2^2}. \tag{2.4}$$

Once the V-number is obtained, the number of modes[1] of the incident wave can be estimated roughly as $V^2/2$. When the V-number is less than 2.405, the fiber can only support one mode, and such a fiber is known as a single-mode fiber (SMF). If the V-number is higher than 2.405, the wave can travel in different routes; thus, the fiber

---

[1] The formal definition of a mode is given in the next section. For now, a mode can be considered as a unique propagation route inside the fiber.

supports more than one mode. Such fibers are called multimode fibers (MMF). The incident light is coupled to different modes inside a multimode fiber, and speckle patterns are formed at the distal end of the fiber due to the complex modal interference during the transmittance.

2.2 Solutions of Wave Equation and LP Modes

Technically, an optical fiber is a cylindrical waveguide that allows the propagation of light, i.e., electromagnetic waves. Therefore, studying optical fiber theory refers to solving Maxwell's equations in a cylindrical geometry[2]. For most applications, cylindrical step-index fibers can be considered homogeneous and lossless dielectric media (no external charge and current exist), where Maxwell's equations reduce to

$$\nabla \times \boldsymbol{E} = -\mu \frac{\partial \boldsymbol{H}}{\partial t}, \qquad \nabla \times \boldsymbol{H} = \varepsilon \frac{\partial \boldsymbol{E}}{\partial t}, \tag{2.5}$$

where $\boldsymbol{E}$ is the electric field, $\boldsymbol{H} = \boldsymbol{B}/\mu$ is the auxiliary field, and ε and μ are the electric permittivity and magnetic permeability of the medium, respectively. These two Maxwell's equations can be combined into a single wave equation that needs to be satisfied by both electric and magnetic fields,

$$\nabla^2 \left\{ \begin{matrix} \boldsymbol{E} \\ \boldsymbol{H} \end{matrix} \right\} - \mu \varepsilon \frac{\partial^2}{\partial t^2} \left\{ \begin{matrix} \boldsymbol{E} \\ \boldsymbol{H} \end{matrix} \right\} = 0. \tag{2.6}$$

Any solution of this wave equation is known as a **mode** of the optical fiber and represents a unique, independent transmission route for the light. In the general solution of the wave equation, none of the six components of the electric and magnetic field vanishes, and thus complicated hybrid modes exist. Instead of concentrating on the full solution of the wave equation, a much simpler and practical solution can be obtained by taking the refractive index difference between the core and the cladding to be sufficiently small, which is known as **weakly guiding approximation** [101–104], $n_1 - n_2 \ll 1$. The resulting modes after the weakly guiding approximation are nearly linearly polarized and referred to as **LP modes**. LP modes are good approximated solutions for most fibers except for photonic crystal fibers and nanofibers where weakly guiding approximation is not valid [105].

---

[2] The calculations and details of solutions showed in this section can be found in many textbooks such as [96–100]

Assuming the solutions of interest are linearly polarized time harmonic electromagnetic waves traveling in the $z-$direction, they can be written in the cylindrical coordinates as

$$\begin{Bmatrix} E \\ H \end{Bmatrix} = \begin{Bmatrix} E(r,\phi) \\ H(r,\phi) \end{Bmatrix} e^{i(\omega t - \beta z)}, \tag{2.7}$$

where $\omega = \frac{2\pi c}{n_1 \lambda}$ is the angular oscillation frequency of the wave and $\beta = \frac{2\pi n_1}{\lambda}$ is the **propagation constant** ($z-$component of the wavevector k). By using the separation of variables, the angular (azimuthal) solution of the wave can also be found easily as $E_\phi(\phi) = e^{im\phi}$, where $m = 0, 1, 2, \ldots$ is an integer emerging as a result of the azimuthal boundary condition (circular symmetry) of the fiber. The remaining radial part of the electric and magnetic field satisfies the Bessel equation, whose solutions are Bessel functions. When physical constraints are applied in the radial direction[3], the radial solutions inside the core are described by the Bessel function of the first kind, $J_m(r)$, and the solutions outside the core are described by the modified Bessel function of the second kind, $K_m(r)$, whose first three orders are plotted in Fig. 2.3.
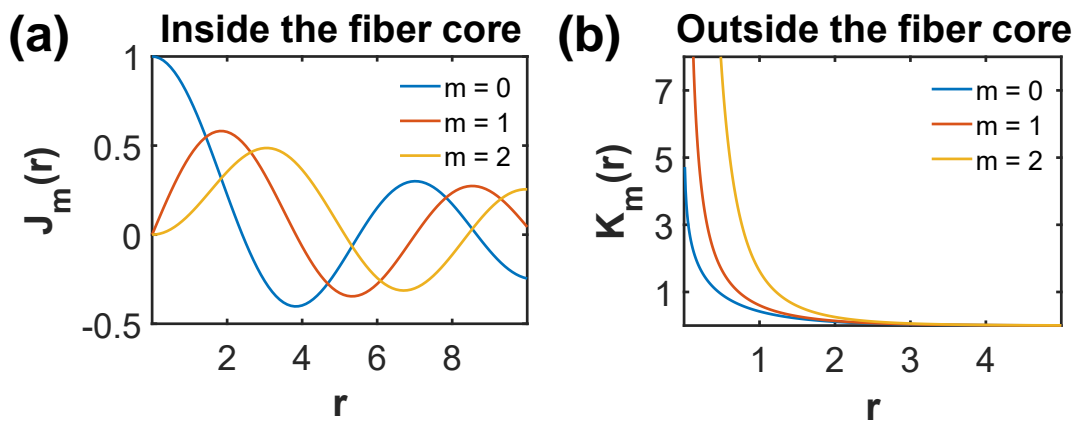
Figure 2.3: The solutions of wave equation inside the fiber are represented by Bessel function of first kind **(a)**, and outside the fiber by modified Bessel function of second kind **(b)**. The wave shows an oscillatory behavior inside the fiber core while it decays exponentially outside.

---

[3] The solution inside the fiber core should be valid at $r = 0$, and the solution outside the fiber core should decay with the increasing radius.

Having the radial part of the solution, the magnitude of electric and magnetic field components of the wave propagating inside a fiber with core radius a can now be written as

$$\left\{\begin{matrix} E \\ H \end{matrix}\right\} = \begin{cases} J_m(\sqrt{k_0^2 n_1^2 - \beta^2}\, r)e^{im\phi}e^{i(\omega t - \beta z)} & \text{for } r \leq a \\ K_m(\sqrt{\beta^2 - k_0^2 n_2^2}\, r)e^{im\phi}e^{i(\omega t - \beta z)} & \text{for } r > a \end{cases} \tag{2.8}$$

where $k_0 = \frac{\omega}{c}$ is the wavenumber in vacuum. The last condition to impose on the system is the continuity of the fields and the potentials at the radial boundary $r = a$. When applied to the solution Eq. (2.8), this boundary condition gives the characteristic equation,

$$U\frac{J_{m+1}(U)}{J_m(U)} - W\frac{K_{m+1}(W)}{K_m(W)} = 0, \tag{2.9}$$

where the normalized wavenumbers U and W are defined as

$$U = a\sqrt{k_0^2 n_1^2 - \beta^2}, \qquad W = a\sqrt{\beta^2 - k_0^2 n_2^2}. \tag{2.10}$$

The characteristic equation, Eq. (2.9), can be solved to find the propagation constant β. The equation has more than one solution for a given value of m, where each solution represents a unique mode of the fiber. For a given m, the pth root of the characteristic equation corresponds to LP$_{mp}$ mode of the fiber, which travels with the propagation constant β_{mp}. Here, m, the azimuthal parameter, represents the variations of the field along the azimuthal (angular) direction, while p, the radial parameter, represents the variations along the radial direction. The LP mode profiles can be visualized by neglecting the dynamic $e^{i(\omega t - \beta z)}$ part of the solutions in Eq. (2.8). The azimuthal exponential can be separated into sine and cosine parts which are called odd and even solutions, respectively. Visually, the only difference between the odd and even representations of LP$_{mp}$ mode is a rotation in the azimuthal direction. Therefore, one azimuthal polarity can be fixed in Eq. (2.8) for visualization purposes.

The details of numerical mode calculations and visualizations can be followed from [106–108]. The first step in mode solutions is to find all propagation constants β_{mp} for a fixed azimuthal parameter m. This is achieved by solving the characteristic equation Eq. (2.9). Each solution is then used in Eq. (2.8) for a chosen azimuthal polarity. The field and intensity distributions of each mode can then be plotted on an appropriate polar grid (r, ϕ). In Fig. 2.4, we show the amplitude, phase, and intensity profiles of

the LP$_{32}$ mode for a step-index multimode fiber with core diameter 105 µm, NA = 0.22 ($n_{\text{core}} = 1.463$, $n_{\text{cladding}} = 1.446$) with an incident light of 1550 nm wavelength. In any LP$_{mp}$ mode, the m index represents the number of azimuthal solutions, and in visual representations of the mode intensity, it is equal to half of the number of angular maxima along the circumference of a circle around the fiber center [109]. Similarly, index p represents the number of radial solutions, which is visualized as the number of maxima along the radial direction in the mode intensity. In Fig. 2.5, we show more examples of the LP mode intensity profiles obtained for the same fiber parameters and the wavelength.
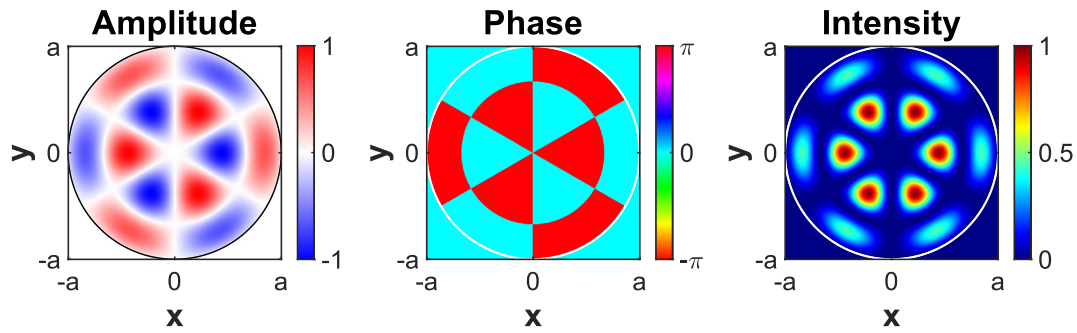
Figure 2.4: Normalized amplitude (real part), phase, and intensity profiles of LP$_{32}$ ($m = 3$, $p = 2$) mode. The amplitude, E_{32}, is, in general, a complex number with both positive and negative values. Once the amplitude E_{32} and phase ϕ_{32} of the mode is known, the intensity can be calculated as $I = |E_{32}e^{i\phi_{32}}|^2$. The number of azimuthal and radial solutions represented in a mode can be verified from the intensity profile as there are $2m = 6$ maxima along the azimuthal direction and $p = 2$ maxima along the radial direction.

16
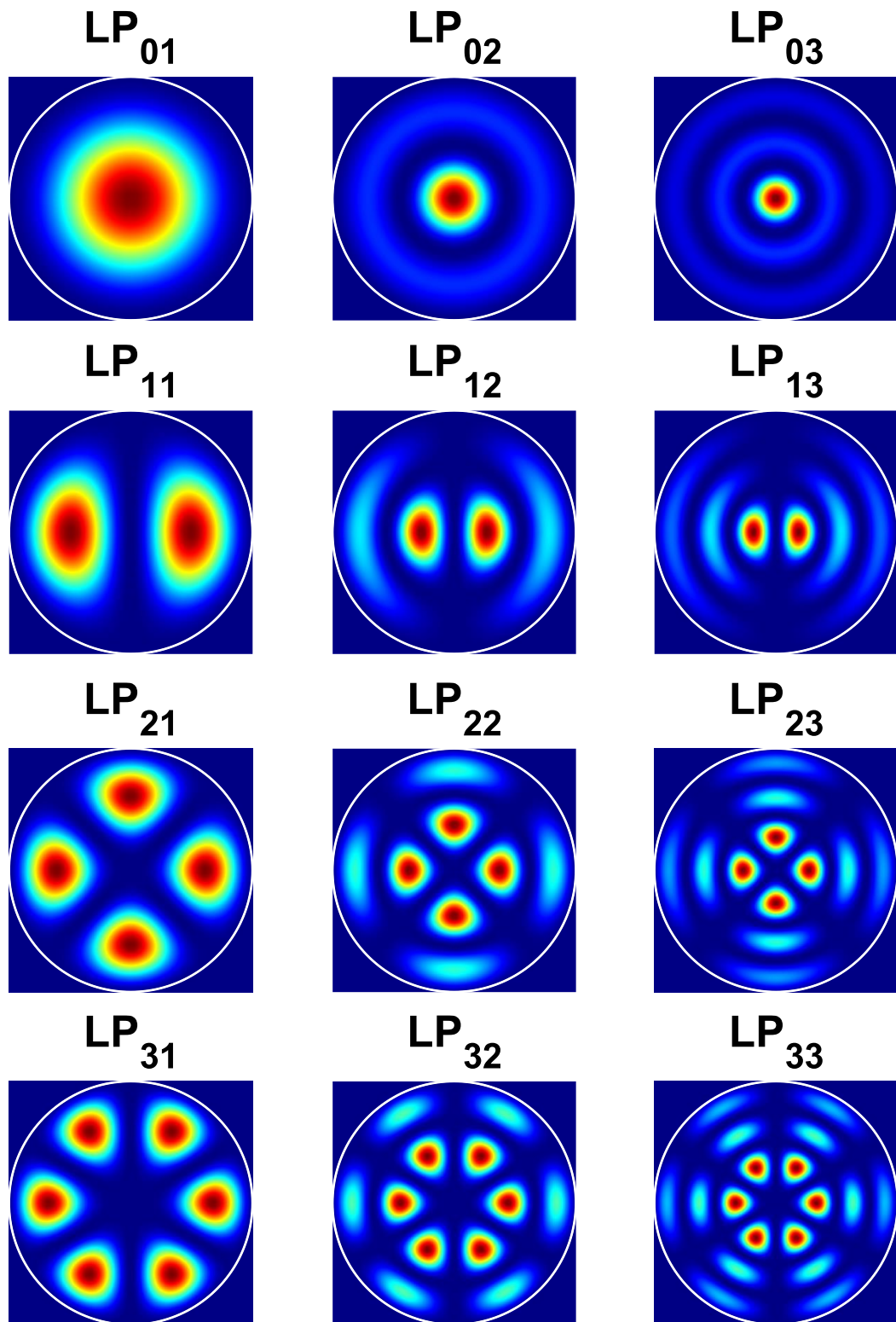
Figure 2.5: Examples of LP mode intensity profiles for a step-index multimode fiber with core diameter 105 μm, NA = 0.22 ($n_\text{core} = 1.463$, $n_\text{cladding} = 1.446$) with an incident light of 1550 nm wavelength.

2.3 Propagation of Light in Fiber and Formation of Speckle Patterns

When a light beam enters the fiber, the beam profile of the light is transformed to the fiber modes by coupling to each mode with a specific weight. Thus, the modes of the fiber can be considered as a complete set of functions, and the spatial profile of the input light, $E_{\text{in}}(r, \theta)$, can be represented as a weighted sum of the fiber modes $E_{mp}(r, \theta)$,

$$E_{\text{in}}(r, \theta) = \sum_{m,p} c_{mp} E_{mp}(r, \theta), \tag{2.11}$$

where c_{mp}, the coupling coefficient, is the weight of the input field coupled to mode E_{mp}. When the input field amplitude $E_{\text{in}}(r, \theta)$ is known[4], coupling coefficients can be found by calculating the overlap integral between the input field and the fiber modes,

$$c_{mp} = \iint E_{mp}^* E_{\text{in}} \, r \, dr \, d\theta. \tag{2.12}$$

Once the coupling coefficients are obtained, the propagation of light inside the fiber can be fully explained analytically. Considering a monochromatic input light of frequency ω, the field distribution at a propagation distance z can be written as

$$E(r, \theta, z) = E_{\text{in}} \sum_{m,p} e^{i(\omega t - \beta_{mp} z)} = \sum_{m,p} c_{mp} E_{mp}(r, \theta) e^{i(\omega t - \beta_{mp} z)}, \tag{2.13}$$

where β_{mp} is the propagation constant of the mode E_{mp}. When a light beam enters the fiber, it couples to the modes of the fiber with the coupling coefficients calculated by Eq. (2.12). These coefficients are then used in Eq. (2.13) to calculate the field (or intensity) profiles at the desired distances. Even when the input beam is a well-structured pattern like a sharp focus, as the beam propagates further inside the fiber, the power starts to spread out, and a speckle pattern is observed due to modal interference given by Eq. (2.13). The propagation of a focused beam inside the fiber at various distances is visualized in Fig. 2.6. A more interesting example is given in Fig. 2.7, Fig. 2.8, and Fig. 2.9, where a text input is propagated inside the same fiber and amplitude, phase, and intensity profiles are plotted, respectively.

---

[4] In practical applications, the intensity of the input field $|E_{\text{in}}(r, \theta)|^2$ can be given instead of the amplitude. In this case, the field amplitude can be obtained by taking the square root.
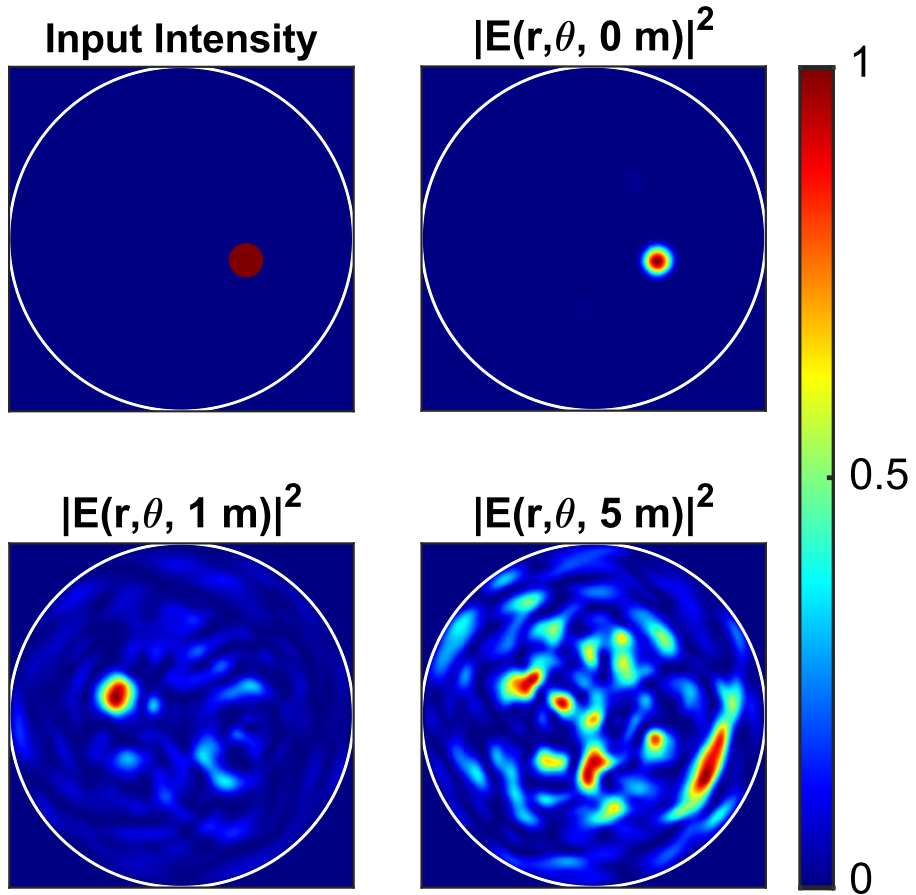
Figure 2.6: Propagation of a focused beam inside the fiber at various distances. The input field is first decomposed into the fiber modes by calculating the overlap integral between the two, and then it is propagated through the fiber by using the propagation constants of the decomposed modes. Thus, the input light is carried along the fiber with the propagation of its constituent modes. The wavelength of the incident light and the fiber parameters used in this simulation are the same as in the previous examples.
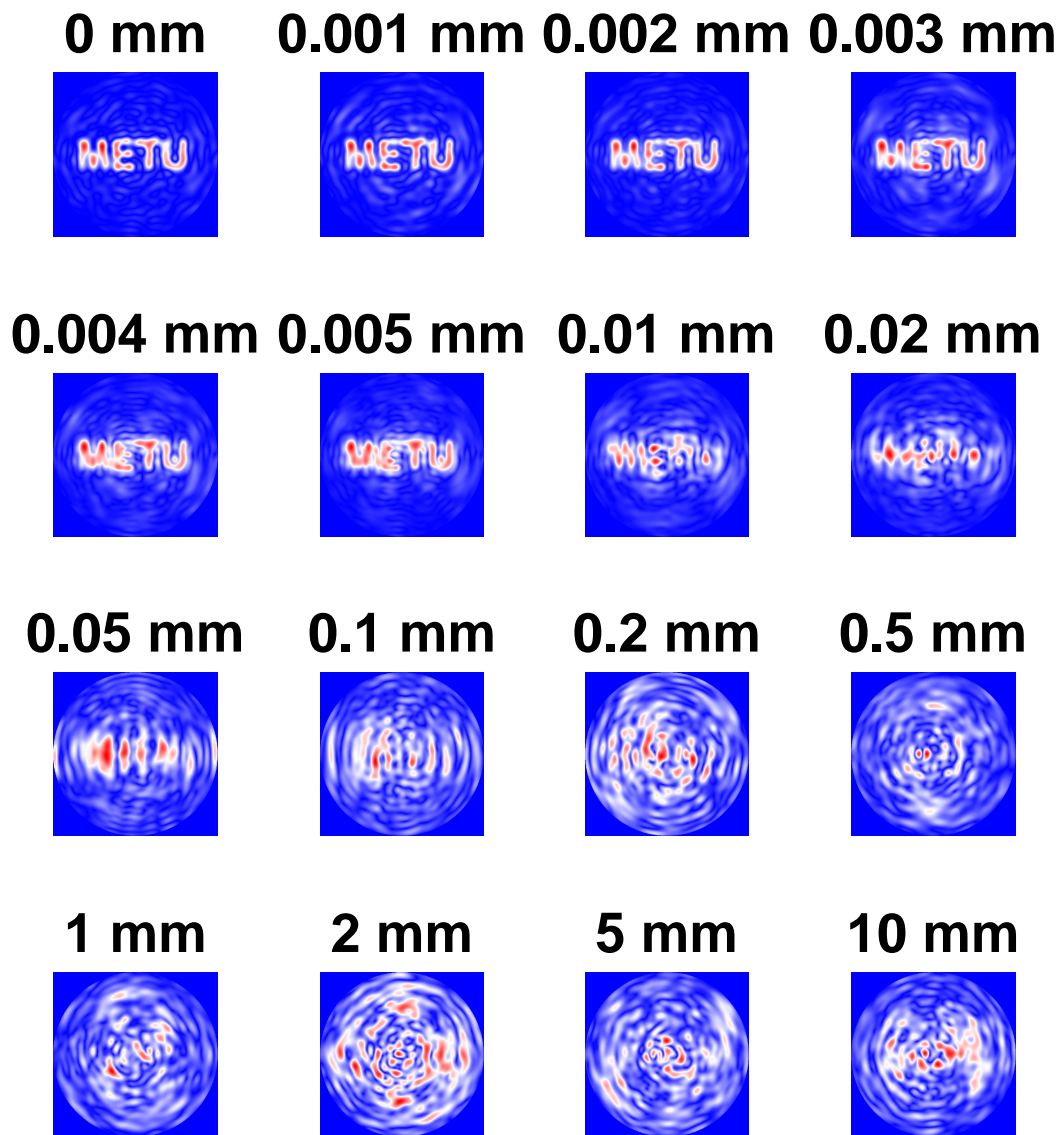
Figure 2.7: Amplitude variation of the text "METU" at different propagation distances along a multimode fiber.
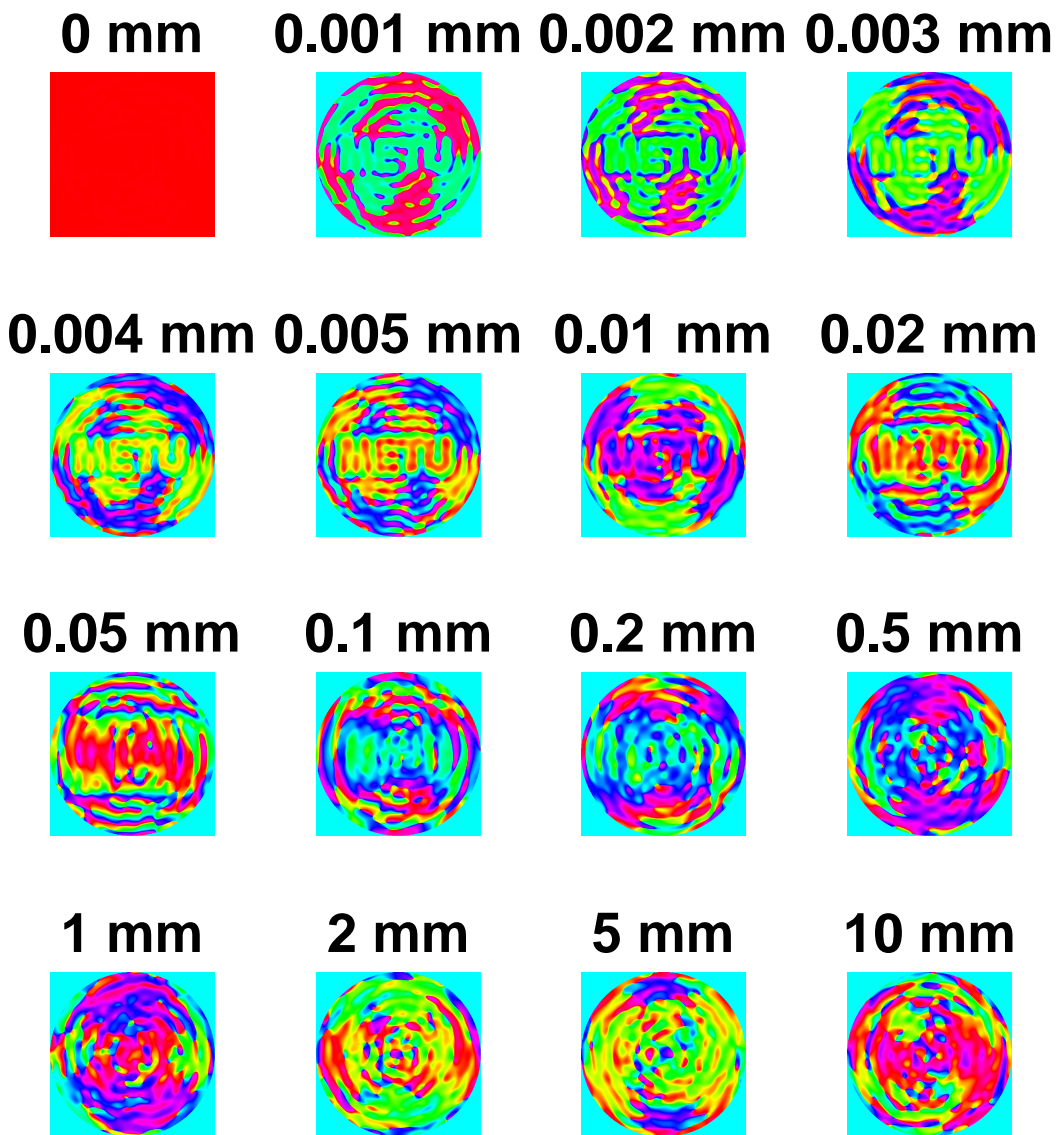
Figure 2.8: Phase variation of the text "METU" at different propagation distances along a multimode fiber.
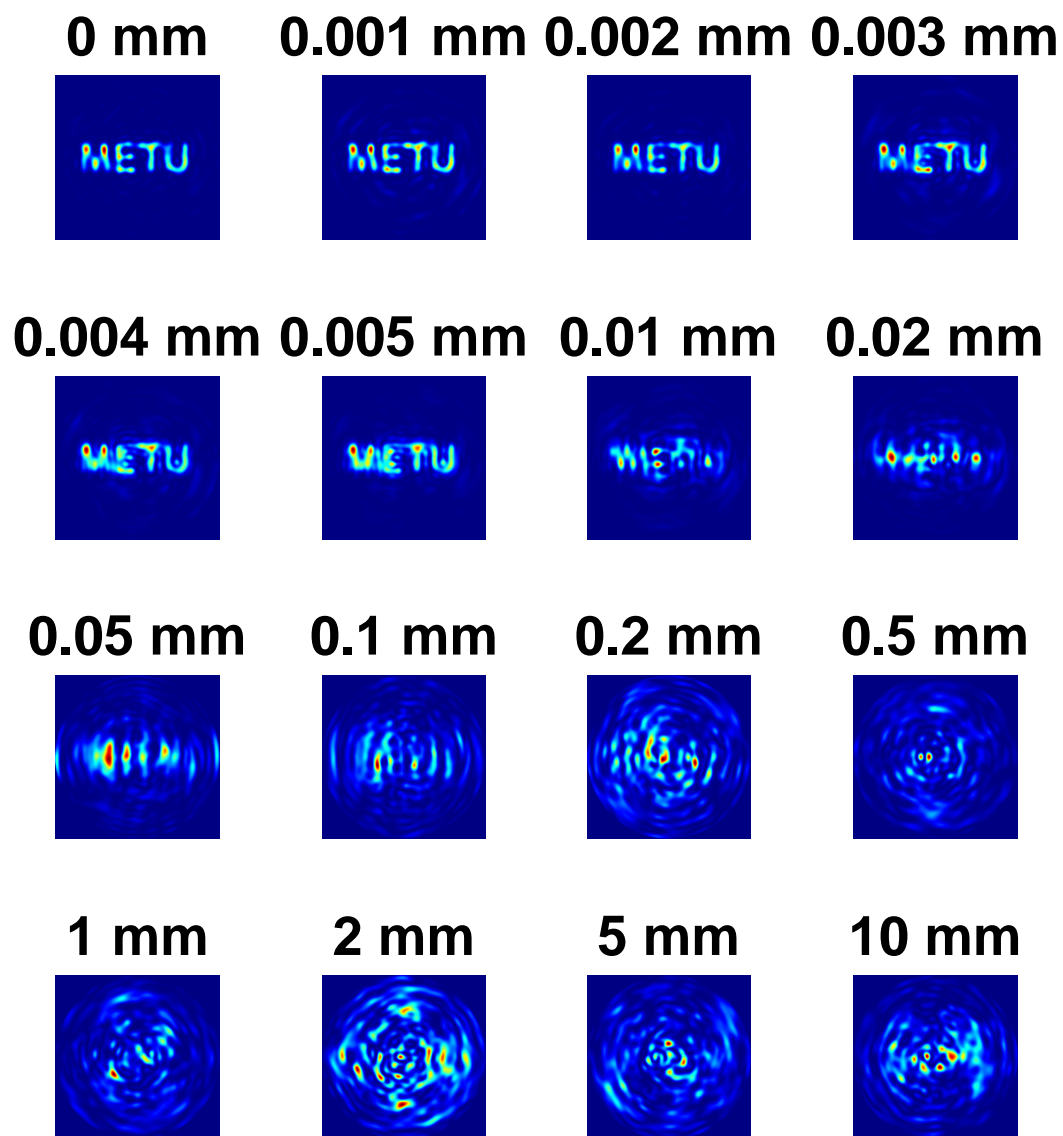
Figure 2.9: Intensity variation of the text "METU" at different propagation distances along a multimode fiber.

CHAPTER 3

METHODS AND EXPERIMENTAL DETAILS

In this chapter, we introduce the experimental setup, apparatus, and methods used in the experiments. The inner structure of the spatial light modulator (SLM) is described in Section 3.2, and the role of liquid crystals in the working principle of SLM is discussed. Achieving a high-quality focus across a scattering medium is a good indicator and verification of the proper functioning of the SLM and the setup. In Section 3.3, we introduce two feedback-based optimization algorithms which are used to modulate the phase of the incident light to obtain a focus at the distal end of a multimode fiber. We show that the non-sequential algorithm, which changes the whole SLM pixels at once, gives a higher-quality focus compared to the pixel-based sequential algorithm. The quality of the focus is measured by calculating the peak-to-background ratio (PBR) of the camera image. The PBR is also used as the objective function (to maximize) in the optimization process of both algorithms. The position and the size of the focusing region are carefully chosen in this chapter for demonstration purposes, but in principle, they can be chosen randomly over the image within the physical limitations.

3.1 Experimental Setup

The experiments in the upcoming chapters are performed with the setup shown in Fig. 3.1. In some experiments, there has been made very slight changes that do not alter the accuracy or repeatability of the results.
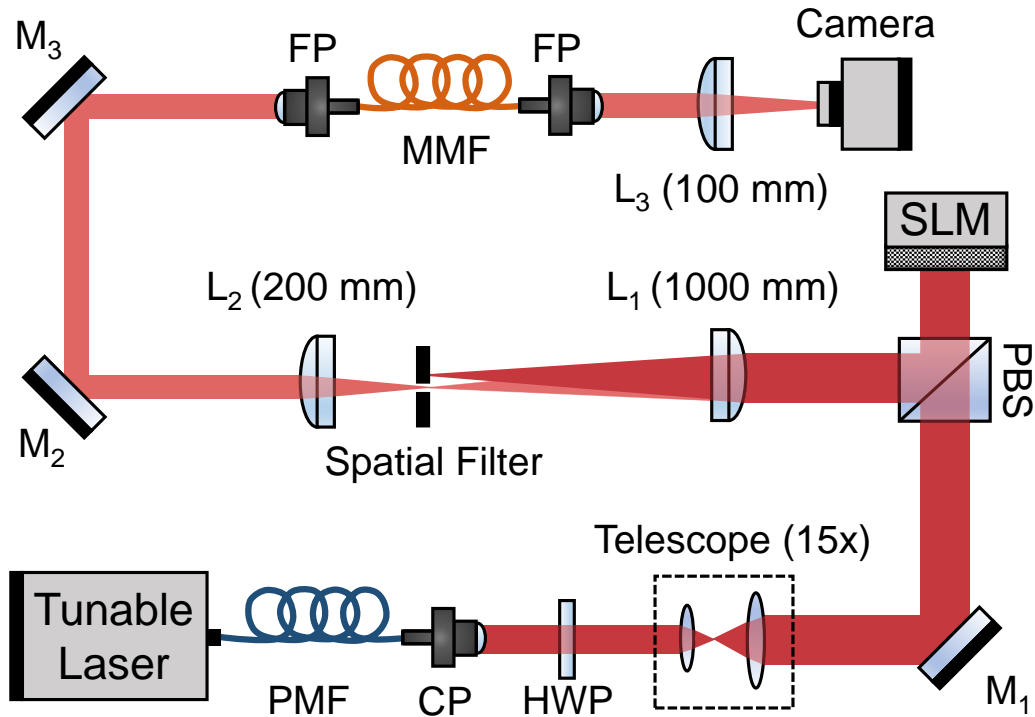
Figure 3.1: Schematic drawing of the experimental setup. M: Mirror, L: Lens, CP: Collimation Package, FP: Fiber Port, PMF: Polarization Maintaining Fiber, HWP: Half-Wave Plate, BE: Beam Expander, PBS: Polarizing Beam Splitter, SLM: Spatial Light Modulator, SF: Spatial Filter, MMF: Multimode Fiber

A tunable laser (SANTEC - WSL100) is used as the primary light source, which can emit <100 kHz linewidth wavelengths between 1527.60 nm to 1565.50 nm (38 nm tuning range) with a tuning step-size of ~1 pm. The output power of the laser can also be tuned between 5.01 mW to 35.48 mW. The deep learning study in Chapter 5 is executed on a similar setup with a visible laser operating at 671 nm. The output of the laser is coupled to an FC/APC polarization maintaining fiber in order to produce a linearly polarized light. The half-wave plate is used to control the incident polarization

so that it matches the alignment direction of the liquid crystals inside the spatial light modulator (more details are given in Section 3.2). The beam is then expanded with a 15x beam expander so that the whole SLM screen (HOLOEYE PLUTO TELCO) can be covered. The SLM is used to shape the incident wavefront by changing its phase, which provides a wide range of uses. SLMs can be used to create holograms of the desired objects as well as to focus light at any target location. A 2-inch polarizing beam splitter is placed to ensure the same incoming and outgoing polarizations after the SLM. Other popular methods to implement an SLM into the experiments are listed in [110]. A 4-f system is used after the SLM with two lenses of focal lengths 1000 mm and 200 mm. A blazed grating is fixed on the SLM for all applications, and the zeroth order diffraction formed after the blazed grating is eliminated with a spatial filter since it carries the "unmodulated" pixelated geometry of the SLM [111–115]. The light is then directed into the multimode fiber with the help of a fiber port system, and speckles are captured with an InGaAs FPA camera (Allied Vision - Goldeye G-008 TEC1). The multimode fiber is fixed to the optical table with adhesive tapes without further advanced isolation methods. The fiber is susceptible to environmental conditions such as temperature variation, humidity, and vibrations, and as a result of this, the speckles formed at the exit of the fiber are expected to change over time. Fig. 3.2 shows the decorrelation of a speckle image over a five hours period. The speckle obtained after five hours is observed to be $\sim 2\%$ different than the initial speckle.

Long calibration/optimization times might be needed in the spectrometer studies presented in Chapter 6 and Chapter 7, and instability of the speckles may create a huge impact in this case. These studies require the use of matrices constructed from the pixels of the speckle images, and the inverse of the matrices is taken in the reconstruction step. Thus, the resolution and accuracy of the spectrometers are highly dependent on the stability of the speckles. This problem can be overcome by isolating the multimode fiber better and by the implementation of faster equipment, such as a laser with high tuning speed, or a faster wavefront modulator, such as a digital micromirror device. Lacking these solutions in our setup, we applied another method to simulate the ideal equipment, which is described in Chapter 6.
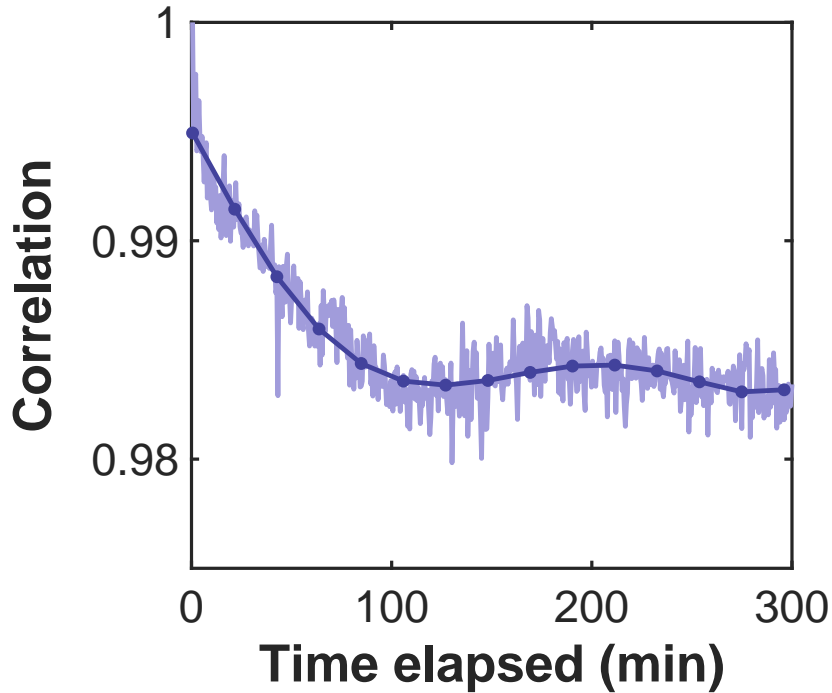
Figure 3.2: Decorrelation of speckle images over time. The speckles obtained after five hours are approximately 2% different than the initial speckle. Fast decorrelation of speckles may cause problems in applications requiring long measurement times. The stability of the system and hence the correlation time of the speckles can be increased with the advanced isolation of the multimode fiber.

3.2 Spatial Light Modulator

The spatial light modulator we use in our experiments is an LCOS (Liquid Crystal on Silicon) two-dimensional reflective microdisplay with full HD (1920×1080) resolution, and it is a phase-only device (can only modulate the phase of the incident light but not the amplitude) [116]. Behind the cover glass of the LCOS microdisplay, there exists a transparent electrode, a liquid crystal (LC) layer, a complementary metal-oxide-semiconductor (CMOS) layer, and alignment layers, as shown in Fig. 3.3. More details about the structure and working principle of spatial light modulators can be found in various resources such as [117–122].
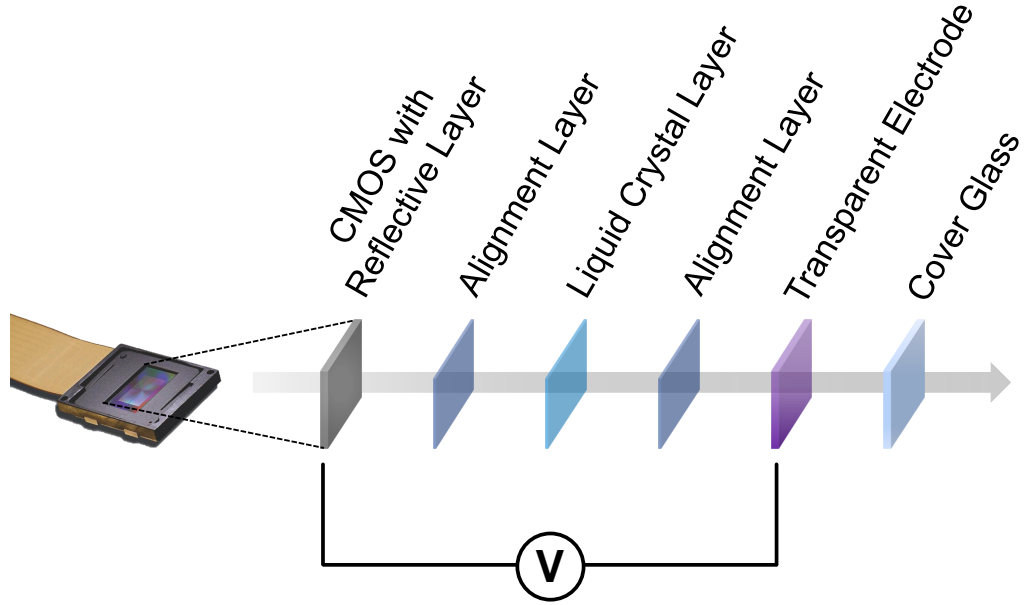
Figure 3.3: Constituents of an LCOS microdisplay. The back panel of the SLM screen is a CMOS with a reflective layer. A liquid crystal layer is sandwiched between the CMOS layer and a transparent electrode, and the front end of the screen is covered with glass. The applied potential between the CMOS layer and the electrode creates an electric field and changes the orientation of the LC molecules.

The phase modulation of the incident light is achieved by controlling the orientation of the liquid crystals through the voltage applied between the CMOS layer and the electrode. The liquid crystals are rod-like molecules, and with the applied electric field, they change their orientations. LC molecules are also birefringent; thus, the refractive indices faced by the incident light in different orientations of the molecule are different. In the unmodulated state, all parts of the light reflected from the SLM experience the same orientation of the LC molecules; hence they travel the same distance inside the liquid crystal. However, as illustrated in Fig. 3.4, when the SLM is programmed, the modulated LC molecules change orientation, and parts of the light traveling through these molecules now experience a delay, which causes a phase difference between different parts of the light. The phase shift between two beams which are reflected from different pixels of a modulated SLM can be written as

$$\Delta\phi = \frac{2\pi}{\lambda} \int_0^d \Delta n(r) \, \mathrm{d}r, \tag{3.1}$$

where d is (roughly) the thickness of the liquid crystal layer.

27
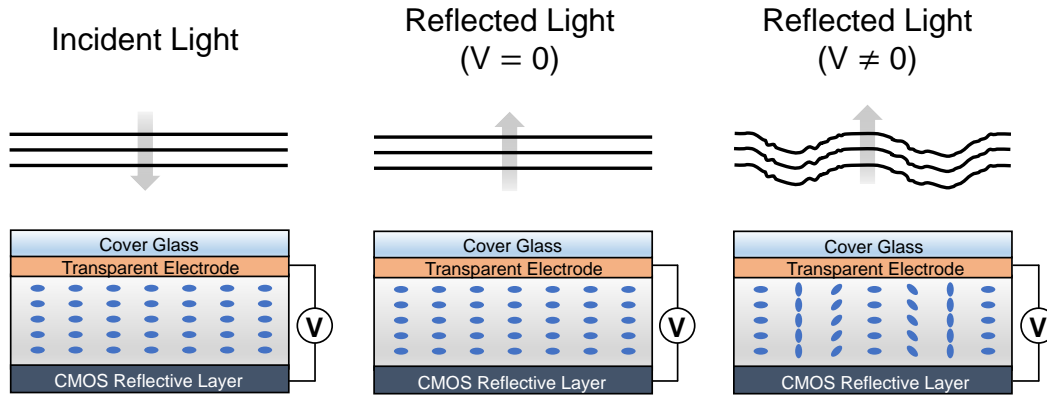
Figure 3.4: Modulation of LC molecules inside the LCOS microdisplay. When the SLM is not programmed, the voltage difference across the liquid crystal layer is zero, and all LC molecules have the same horizontal orientation. In this case, parts of the light incident on different pixels experience the same refractive index; thus, they are reflected with zero path difference. When the SLM is programmed, some LC molecules are rotated as a result of the applied potential. The light reflected from different pixels experiences different refractive indices, which causes a path difference. This mechanism can be used to modulate the incident wavefront in the desired shape.

All pixels of the SLM can be modulated individually and independently by applying unique voltages. In order to create a voltage across the LC layer at a pixel, this pixel is addressed with an 8-bit (256) grayscale value which corresponds to the magnitude of the applied voltage. The SLM in our system has 3.5π phase modulation ability for full addressing. Thus, using the first 146 gray levels is enough to obtain 2π phase modulation.

3.3 Optimization Algorithm

Most of the time, achieving a sharp focus is a convincing sign that the SLM is working correctly with good modulation ability. In Chapter 7, a single-pixel spectrometer will be built by exploiting the modulation ability of the spatial light modulator. Various algorithms can be used to program the SLM for obtaining focus across a complex medium such as multimode fiber [123, 124]. In a phase optimization algorithm, the purpose is to increase the intensity at the desired target location on the detector by

changing the phase of the incident light field. Representing the fields in a phasor diagram, this corresponds to changing the orientations of the field vectors on the target location and making more fields to contribute the constructive interference, as shown in Fig. 3.5.

In our studies, we have used two feedback-based iterative algorithms, a continuous sequential algorithm [123], and a non-sequential algorithm [125], to focus light on a circular target region ($r = 5$ pixels) at a position slightly away from the center of the speckle image formed at the distal end of the multimode fiber [1]. Although a detailed comparison of the algorithms is not done in the context of this thesis, we observed that the non-sequential algorithm gives a better quality focus while the sequential algorithm provides faster focusing; thus, it is time effective. The final results of the single-pixel spectrometer in Chapter 7 are obtained by using the sequential algorithm.

Before Wavefront Shaping   After Wavefront Shaping
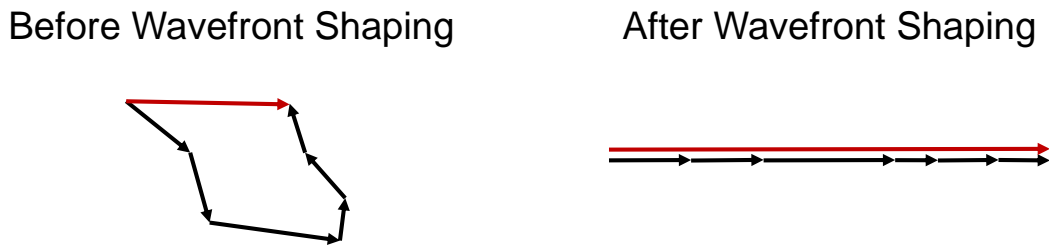
Figure 3.5: Complex plane representation of phase optimization algorithms. Black vectors represent the electric fields in the complex plane. Before the optimization, the fields randomly contribute to the total field on that point, shown with the red arrow. With phase optimization algorithms, the field vectors are rotated to interfere constructively. As a result of the constructive interference, the light can be focused at any desired target location on the output of the system.

---

[1] The position and radius of the target region are specific to our setup, although, in general, they can be chosen at any location and size. Of course, the size of the focal spot is limited by the size of the smallest speckle grain.

3.3.1 Enhancement and Peak-to-Background Ratio

In their groundbreaking study [126], Vellekoop and Mosk used enhancement factor η to measure the wavefront shaping performance and focusing quality of their system. The enhancement factor η is defined as the ratio between the optimized intensity (the intensity of the focused region after wavefront shaping) and the ensemble averaged intensity of the speckle image before optimization,

$$\eta = \frac{I_{\text{target}}^{\text{after}}}{\left\langle I_{\text{speckle}}^{\text{before}} \right\rangle}, \tag{3.2}$$

where $\langle \ldots \rangle$ denotes the ensemble average. The enhancement factor is useful when comparing the initial and final states of the systems, and it is also effective in calculating the increase in total light transmission.

In our experiments, we used a more dynamic figure of merit, peak-to-background ratio (PBR), to determine the focus quality of light across the multimode fiber. PBR does not involve the initial state of the system and aims to compare the intensity of the focused region to the mean intensity of its surrounding in the current state,

$$\text{PBR} = \frac{I_{\text{target}}}{\left\langle I_{\text{surrounding}} \right\rangle}. \tag{3.3}$$

For dynamic scattering media, the quality of the focus is limited by the temporal stability of the medium, which is given by the persistence time, T_P [123]. Therefore, in highly dynamic media such as living tissue ($T_P \approx 10^{-3}$ seconds), it may not be possible to reach high enhancements or PBRs as desired. In such systems, the speed of the wavefront modulator device becomes a key factor, and for that reason, using a digital micromirror device (DMD) [30, 127–134] is preferred in biological wavefront shaping applications.

Fig. 3.6 shows an example of light optimization at the distal end of a multimode fiber using phase optimization. At each iteration of the optimization, the SLM tries to find a better pattern to increase the PBR of the output speckle image. The PBR of the final image is 701.03, and it is ~11.7 times higher than the initial PBR before wavefront shaping (initial PBR = 60.15). Fig. 3.6(e)-(f) shows the intensity on the cross-section shown by the white dashed line on Fig. 3.6(c)-(d).
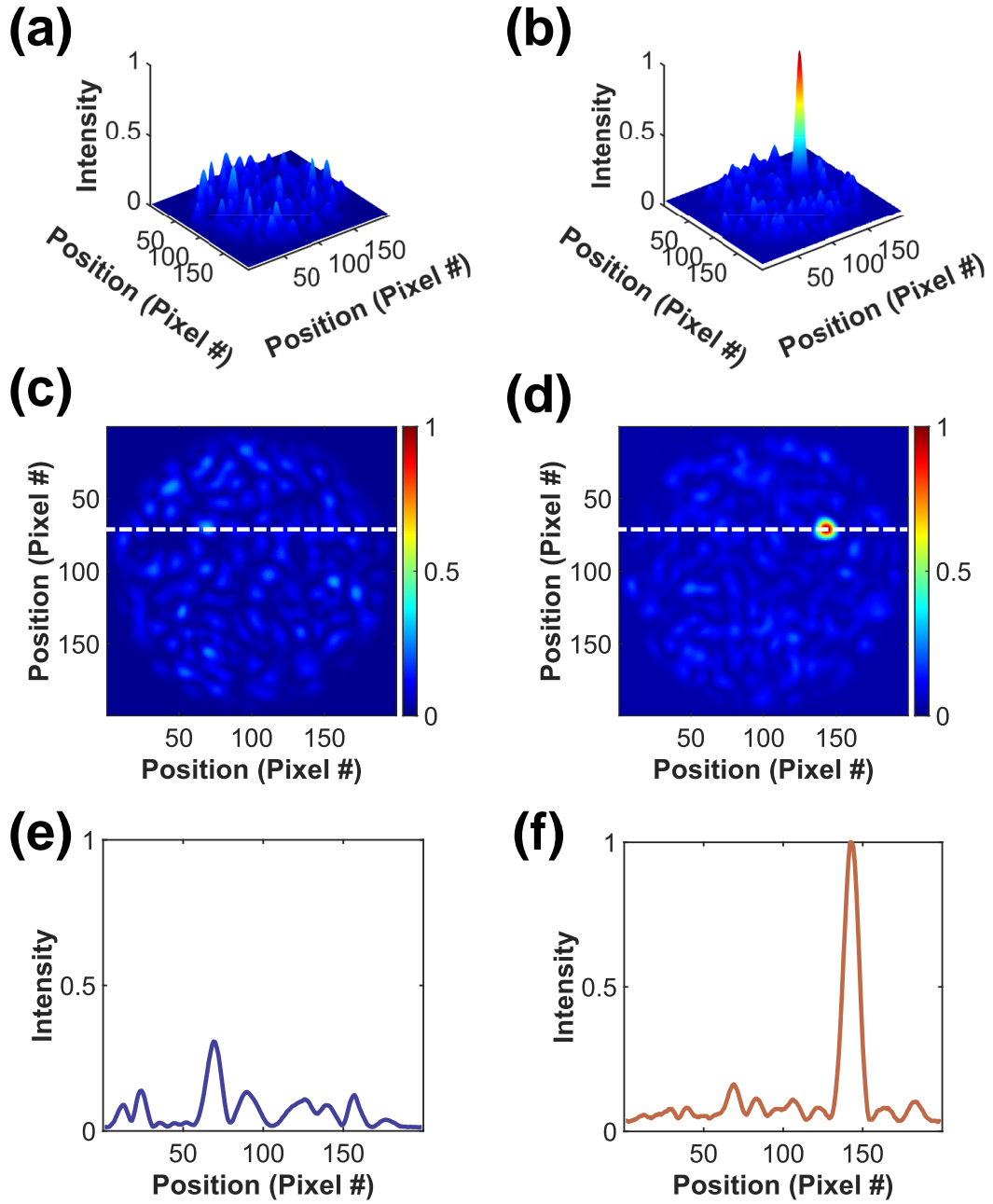
Figure 3.6: Comparison of speckle image before and after wavefront shaping. **(a)-(b)** 3D visualization of the speckles before and after optimization. **(c)-(d)** 2D visualization of the speckles before and after optimization. **(e)-(f)** Intensity variation along the white dashed line on the 2D speckles before and after optimization.

3.3.2 Continuous Sequential Algorithm

Fig. 3.7 shows the principle of the continuous sequential algorithm as described in [123]. Each segment of the SLM is optimized individually to focus the light at the target location on the camera. The size of the segments (group of pixels) and the number of phase steps are determined by the user according to the needs [2]. Generally, the phase of each segment is cycled from 0 to 2π, and the peak-to-background ratio (or any other figure of merit to measure focusing quality) of the output image is computed for each phase. The phase of each segment is then set to the optimal phase, which gives the highest PBR. The process is then repeated for all segments of the SLM, and the optimal SLM pattern is obtained.
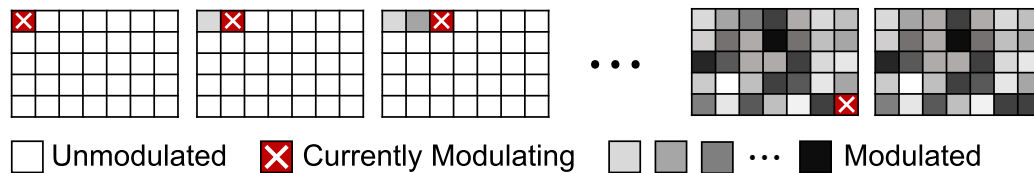
Figure 3.7: Principle of continuous sequential algorithm. Individual pixels (or groups of pixels) on the SLM are programmed sequentially to increase the focusing quality of the beam on the desired target region of the camera. The optimal phase value of each pixel is determined by calculating the PBR of the output image.

Fig. 3.8 shows the states of the SLM and the camera before and after applying the continuous sequential algorithm. As mentioned earlier in Section 3.1, we always keep a blazed grating on the SLM and allow only first-order diffraction to reach the multimode fiber. The SLM screen is divided into 144 macropixels of size $120{\times}120$. Four phase values, $0, \pi/2, \pi, 3\pi/2$, are written on each macropixel and for each phase, the peak-to-background ratio of the speckle image is measured for the chosen target point (shown with the red circle). The optimization is stopped after three iterations of the whole SLM screen, which took approximately 30 minutes. The PBR of the output speckle image is increased 6.6 times, from $\text{PBR}_{\text{initial}} = 78.3$ to $\text{PBR}_{\text{final}} = 517.3$.

---

[2] It would be wise to choose both the number of segments and the number of phase steps to be as low as possible for a highly dynamic medium so that the optimization can be completed before the persistence time of the medium.
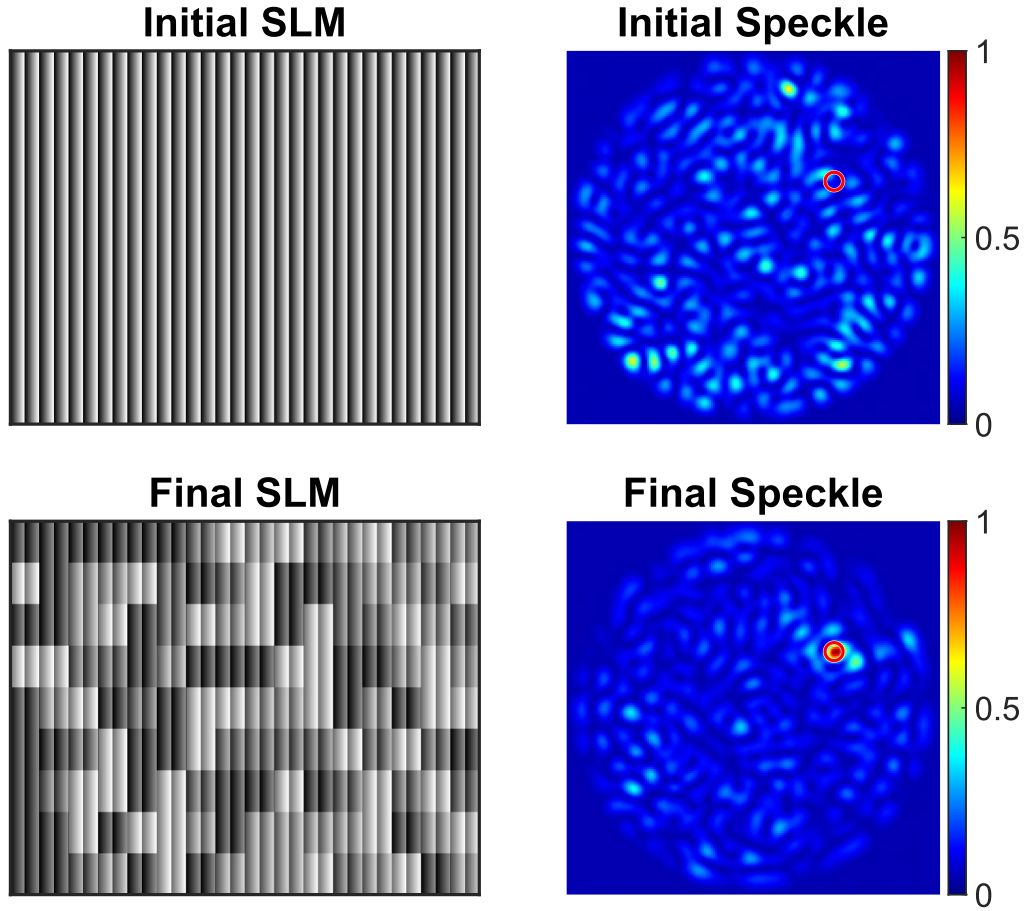
Figure 3.8: Initial and final SLM patterns (left) and corresponding speckles (right) obtained with the implementation of continuous sequential algorithm. All modulation is done on the blazed grating kept on the SLM. 144 macropixels are optimized in three iterations using four phase values between $0 - 3\pi/2$. A focus is be obtained on the target location (shown with the red circle) after $\sim$30 minutes. The PBR of the system is increased 6.6 times, from 78.3 to 517.3.

3.3.3 Non-sequential Algorithm

The non-sequential algorithm introduced in [125] is another feedback-based iterative optimization algorithm we used to focus the light at the distal end of a multimode fiber. Opposite to the sequential algorithm, this algorithm changes the value of all pixels on the SLM in each iteration [106]. A simple flowchart of the algorithm is shown in Fig. 3.9. In the nth iteration of the SLM screen, the algorithm calculates a temporary phase,

Φ_{temp}, using the last successful SLM phase Φ_{n-1},

$$\Phi_{\text{temp}} = \arg\left[(1-\xi)e^{i\Phi_{n-1}(x,y)} + \xi e^{i(kx\cos\alpha + ky\sin\alpha + \theta)}\right], \qquad (3.4)$$

and decides whether to keep the temporary phase by comparing the performance of Φ_{n-1} and Φ_{temp} on creating a better quality focus. Here, x and y correspond to SLM pixels while the other variables, ξ, α, θ, k, are randomly generated in each trial. ξ is a random number between 0 and $1/2$, while the random phase θ and the angle α are chosen in the range $0 - 2\pi$. The wave vector k is chosen randomly in the interval $[0, k_{\text{max}}]$, where k_{max} depends on the system parameters such as the core size of the fiber, the input wavelength, and focal lengths of the lenses used for imaging the SLM screen into the fiber, as described in [125].
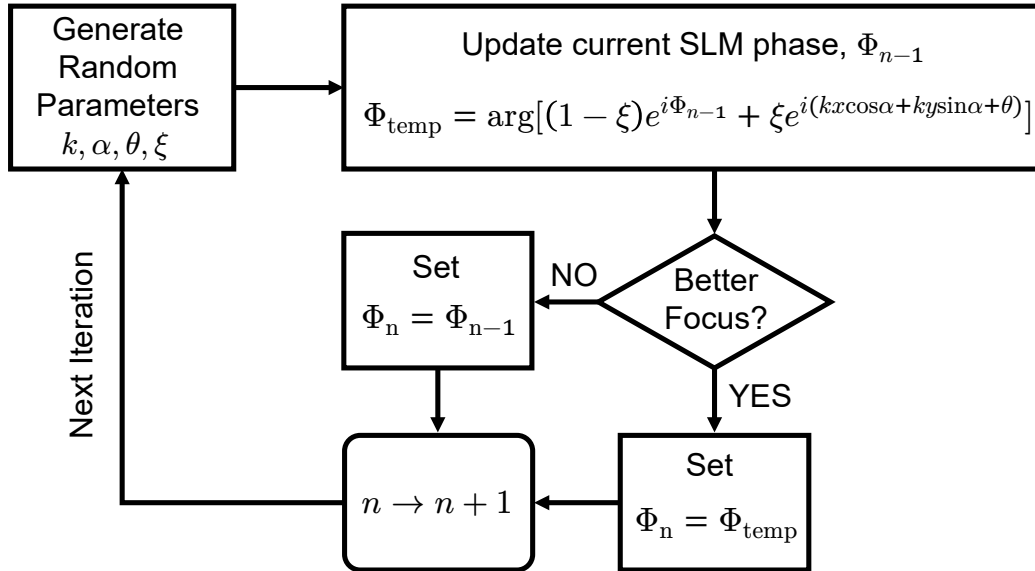
Figure 3.9: Flowchart of non-sequential algorithm. The SLM phase is updated in each iteration with random parameters. The SLM phase mask giving better focus on the desired target point is kept on the SLM after each iteration.

Fig. 3.10 shows an example of light optimization at the distal end of a multimode fiber using the non-sequential algorithm. The light is very sharply focused in the target location (red circle) after 90 minutes, increasing the PBR 8 times (initial PBR is 96.0 for this example).
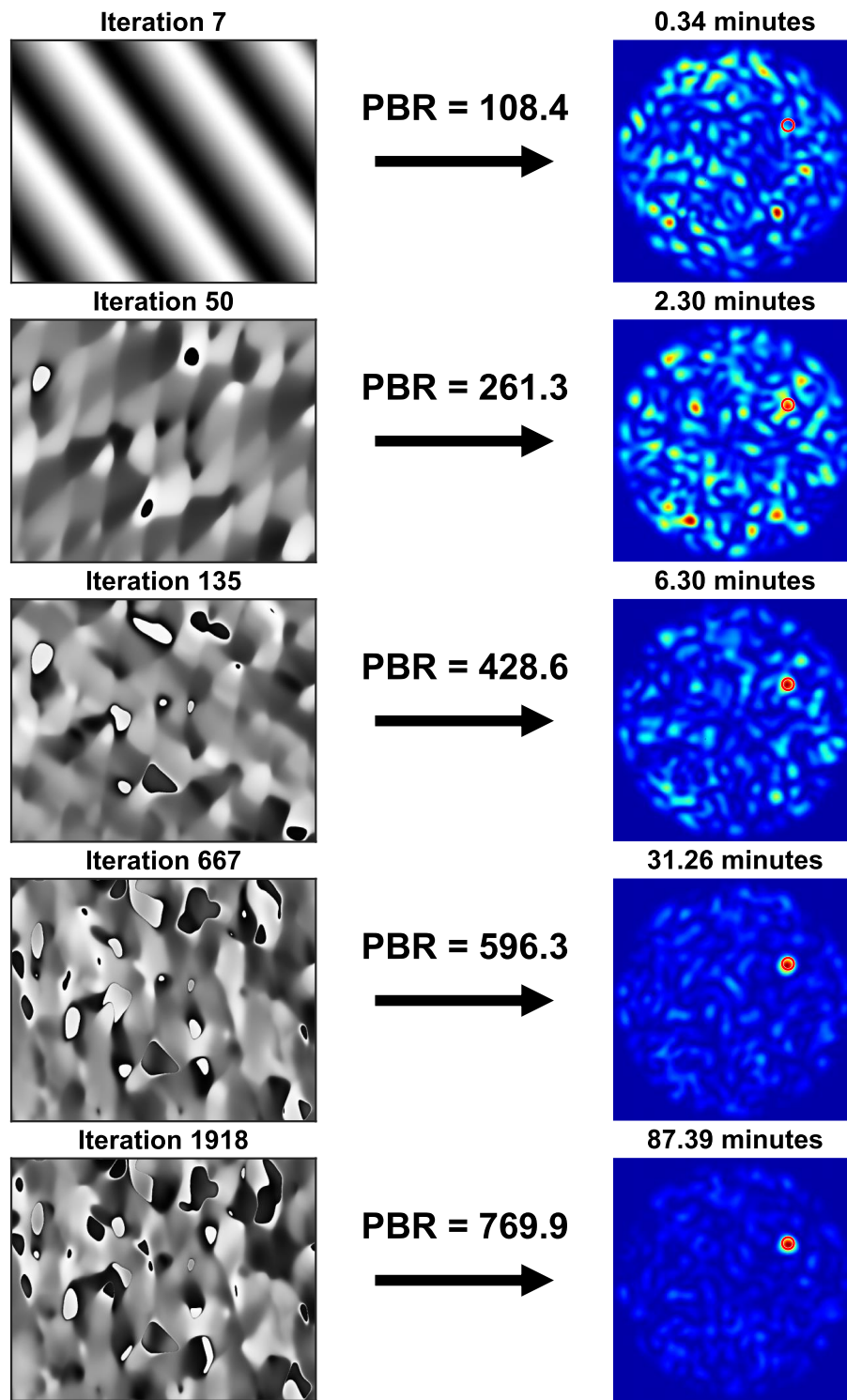
Figure 3.10: SLM patterns (left) and corresponding speckles (right) for various iterations in a non-sequential phase optimization algorithm. A decent focus can be obtained on the target location (shown with the red circle) after ~30 minutes with PBR > 500. If the optimization time is increased to 90 minutes, the focus gets very sharp with PBR = 769.9.

The results obtained in Fig. 3.10 show that the focusing quality does not significantly improve between iterations 667 and 1918. The PBR increases by 29% during this period, in ∼60 minutes, while it increases by 128% between iterations 7 and 667, in ∼30 minutes. To balance the focusing quality and optimization time, the number of iterations for which the PBR starts to converge can be set as the final iteration of the algorithm. Fig. 3.11 shows the increase in the peak-to-background ratio with the number of iterations for three different runs of the algorithm. For all three runs, the PBR starts to converge after 800 iterations, where we obtain a decent focus with PBR > 500. When the average of all runs is considered, PBR = 500 is exceeded after around 600 iterations, which corresponds to roughly 30 minutes of optimization. Therefore, the algorithm can be set to execute until 600 iterations or 30 minutes of optimization time is reached.
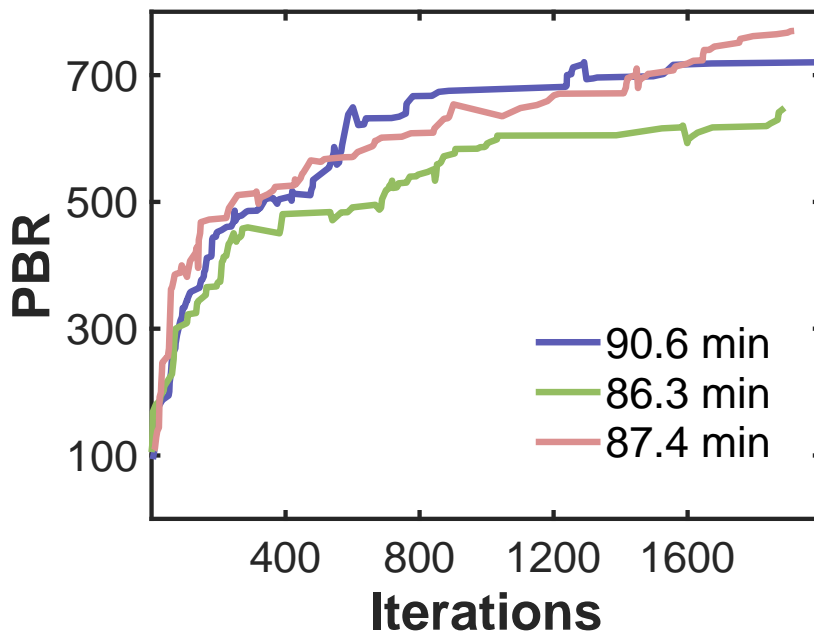
Figure 3.11: Peak-to-background ratio vs. the number of iterations for three different runs of the optimization algorithm. The increase in the PBR is not significant after 800 iterations, where we obtain a decent focus with PBR > 500.

CHAPTER 4

OPTICAL CLASSIFICATION THROUGH SPECKLE IMAGES

In this chapter, we present a primitive but also powerful demonstration of wavefront shaping in optical information transfer, which can lead to insightful applications in communication, cryptography, and computing. We start the chapter by giving background information on classical computing and how information is encoded. The background information is based on the delightful textbook [135]. We then demonstrate the use of spatial light modulators in encoding information. We write distinct gratings on the SLM screen for each number from 1 to 9, and guarantee each grating to create a unique speckle after traveling through a multimode fiber. The speckle patterns, y, are used to construct a calibration matrix, T, and the input numbers, x, are reconstructed by solving the inverse propagation equation $x = \text{T}^{-1} * y$. We test the long-term classification accuracy of our system and share the results at the end of the chapter. The system we propose here is a demonstration of two-fold optical encryption of information where we first encode the numbers as optical gratings and then scramble the information once more with the propagation inside multimode fiber. Combined with the results in the long-term tests, we believe this system can be further improved to build safe communication schemes.

4.1 Encoding Information into Binary States

In classical computing, the information is expressed in terms of *bits*, which refers to two possible states: 0 and 1. Being a two-state system, a bit carries the smallest amount of information possible. To better understand the concept of bits, we can make an analogy with the coins. A coin has two states, heads (H) and tails (T), meaning one coin can only represent two different pieces of information. A common example of a two-state information system is a switch on an electrical circuit. We can associate the "on" and "off" states of the switch with the heads and tails of a coin, respectively (see Fig. 4.1). In this scenario, when the coin is in the H state (switch "on"), no current flows through the circuit, and the light bulb does not glow. Conversely, when the coin is in the T state, a current flows through the circuit, electrical energy is transferred to the bulb, and the bulb glows. Thus the binary information on whether the light bulb is glowing or not is encoded into the H and T states of the coin as shown in Table 4.1.

Table 4.1: States of the coin and associated information

State of the Coin	Encoded Information
Heads (H)	The light bulb does not glow
Tails (T)	The light bulb glows
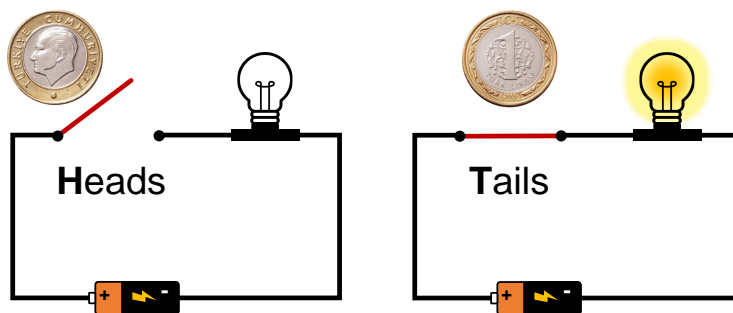
Figure 4.1: Encoding binary information with a single coin. The coin has two states: heads (H) and tails (T), which are associated with the "on" and "off" states of the switch in the circuit. In the given scenario, the states of the coin give information on whether the light bulb is glowing or not.

The number of coins to be used in order to transfer some encoded information depends on the nature of the problem, i.e., the amount of information that needs to be transmitted. If n pieces of information need to be transferred, then the number of coins to be used, m, should satisfy the relation $2^m > n$. A common way of encoding information into binary states is to use binary digits (*bits*), 0 and 1, instead of the H and T states of a coin. Electronic circuits inside the computers generally have two voltage levels, 0 volts, and 5 volts, and conventionally this two-level system is described by bits. A group of bits can be combined to represent a larger amount of information. The states obtained in this form are called *binary strings* or *bit strings*.

In common practice, we use decimal numbers which are represented in base-10. A bit string, on the other hand, can be used to represent numbers in base-2. As in the case of decimal numbers, for a given binary (base-2) number, digit d denotes how many of $d-$power of 2 the number has. For a communication scheme involving only numbers from 1 to 9 ($n = 9$), a binary string of length four is enough since $2^m > n$ relation is satisfied for $m = 4$, as shown in Table 4.2.

Table 4.2: Representation of decimal (base-10) numbers in binary (base-2) 4-bit form

Decimal (Base-10)	Binary (Base-2)
1	0001
2	0010
3	0011
4	0100
5	0101
6	0110
7	0111
8	1000
9	1001

4.2 Optical Encryption of Binary Numbers

The study we present in this chapter aims to construct a safe communication method by encrypting binary numbers optically. Encryption can be considered as putting a piece of information into a form that is difficult to read without the appropriate key. And decryption is the transformation of encrypted information back into its initial readable form. In recent years, there has been a growing interest in the utilization of optical systems for encryption [136–151]. Here, we use two-fold encryption by:

1. Converting the binary numbers into optical gratings

2. Propagating them through a multimode fiber

We first convert the decimal numbers from 1 to 9 into bit strings of length 4 (see Table 4.2) and then, for each number, we create an appropriate phase mask on the spatial light modulator. The SLM masks are formed from two phase values, 0 and π, which correspond to 0 and 1 states of the binary system. Thus, when a digit in the bit string is 0 (1), then 0 (π) phase shift is added to the SLM to represent this digit. After deciding on the phase values, we scan the SLM screen with varying-sized rectangles to determine the regions of the SLM most responsive to the π phase shift. The four rectangular regions obtained after this process are used in the experiment to demonstrate the classification of numbers. Fig. 4.2 shows the phase distributions created for each binary number. We modulate only the region shown with the solid black rectangular window since it is the most responsive area of the SLM, specific to our setup. Each small rectangular window (separated by dashed lines) represent a binary state, or a digit in bit string. As mentioned earlier in Chapter 3, we always keep a vertical blazed grating on the SLM screen in order to eliminate the unmodulated (pixelated) part of the SLM. When the phase distributions are added to this blazed grating, they shift the blazed grating with an amount corresponding to the written phase distribution. Fig. 4.3 shows the SLM patterns when the phase distributions are applied. Clearly, a π phase shift on a region changes the original gray levels to their direct opposite. Fig. 4.4 shows the speckle patterns created after the light reflected from the gratings travels through the multimode fiber.
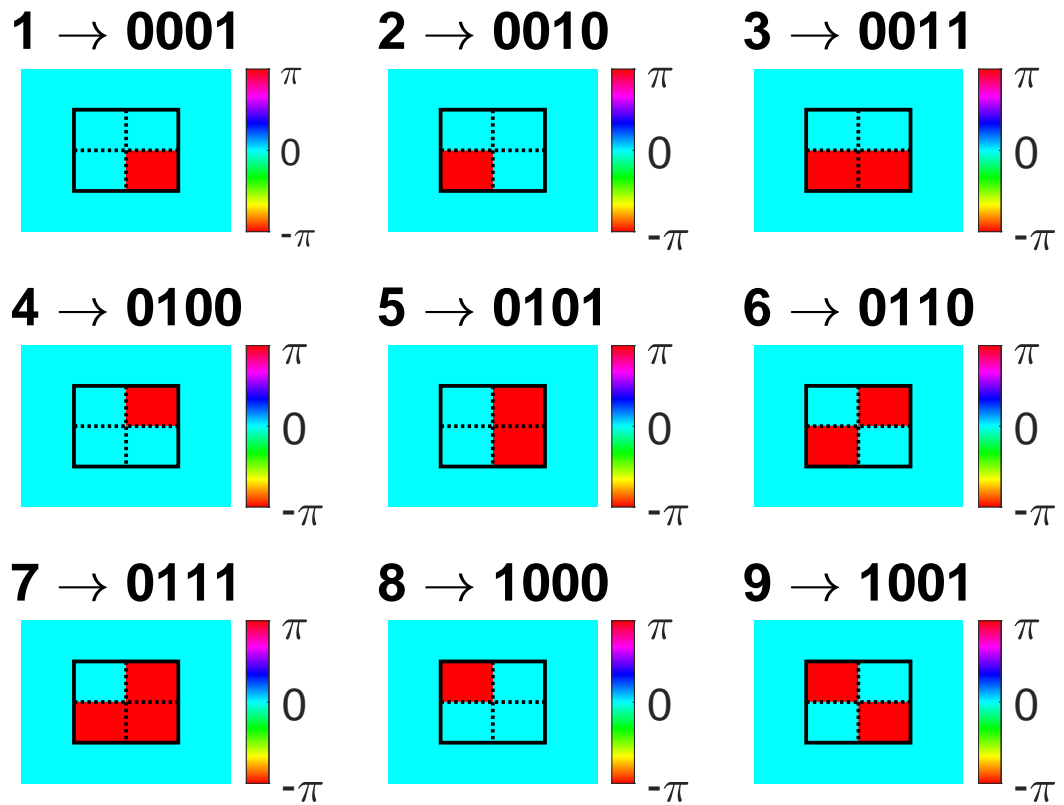
Figure 4.2: Phase distribution written on the SLM screen for encoding bit strings of length four corresponding to the numbers from 1 to 9. The binary number 0 (1) is encoded as 0 (π) phase shift. Encoding is applied to the most responsive regions of the SLM, which are determined by scanning varying-sized rectangles of phase 0 and π over the whole SLM screen. Four regions used to encode the digits in the bit string are separated by dashed lines.
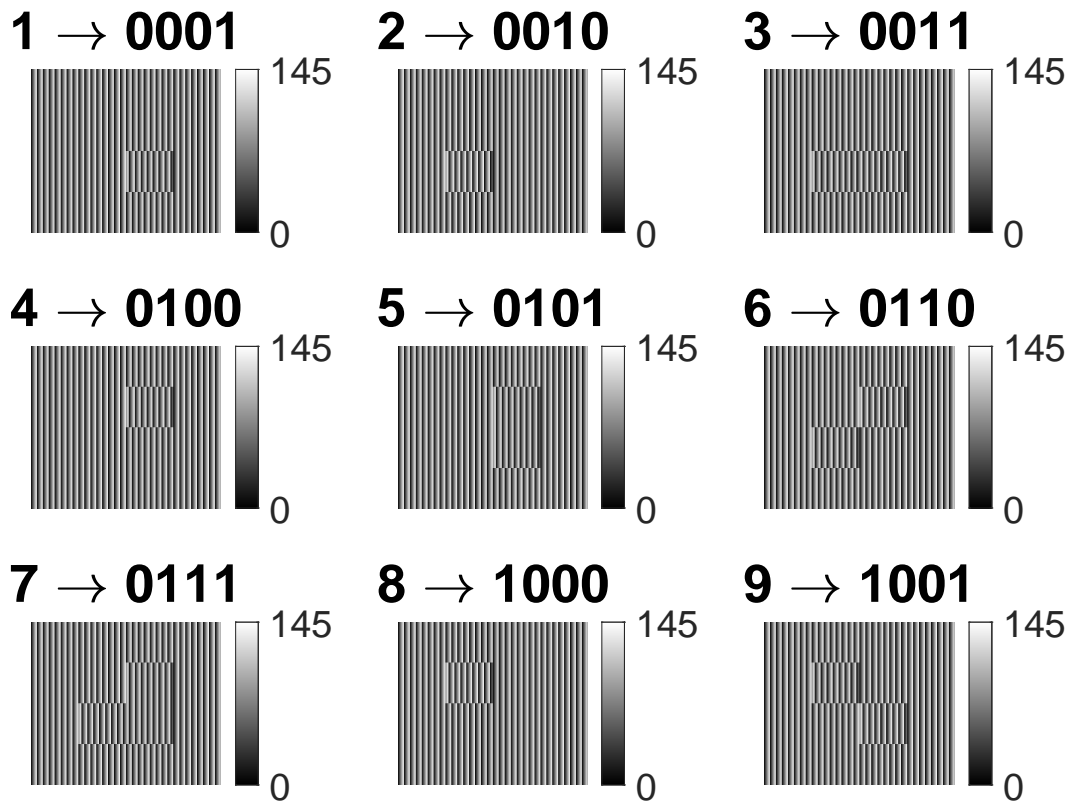
Figure 4.3: SLM patterns for encoding bit strings of length four corresponding to the numbers from 1 to 9. The numbers are encoded onto the vertical blazed grating, which is always kept on the screen to avoid the pixelated nature of the SLM. The binary number 0, which is encoded to create a 0 phase shift, does not change the gray levels of the blazed grating. The binary number 1, encoded to create π phase shift, shifts the gray levels to their direct opposite. Optically, the light beam incident on the modulated part of the SLM is introduced a π phase shift compared to the beams incident on the unmodulated parts.
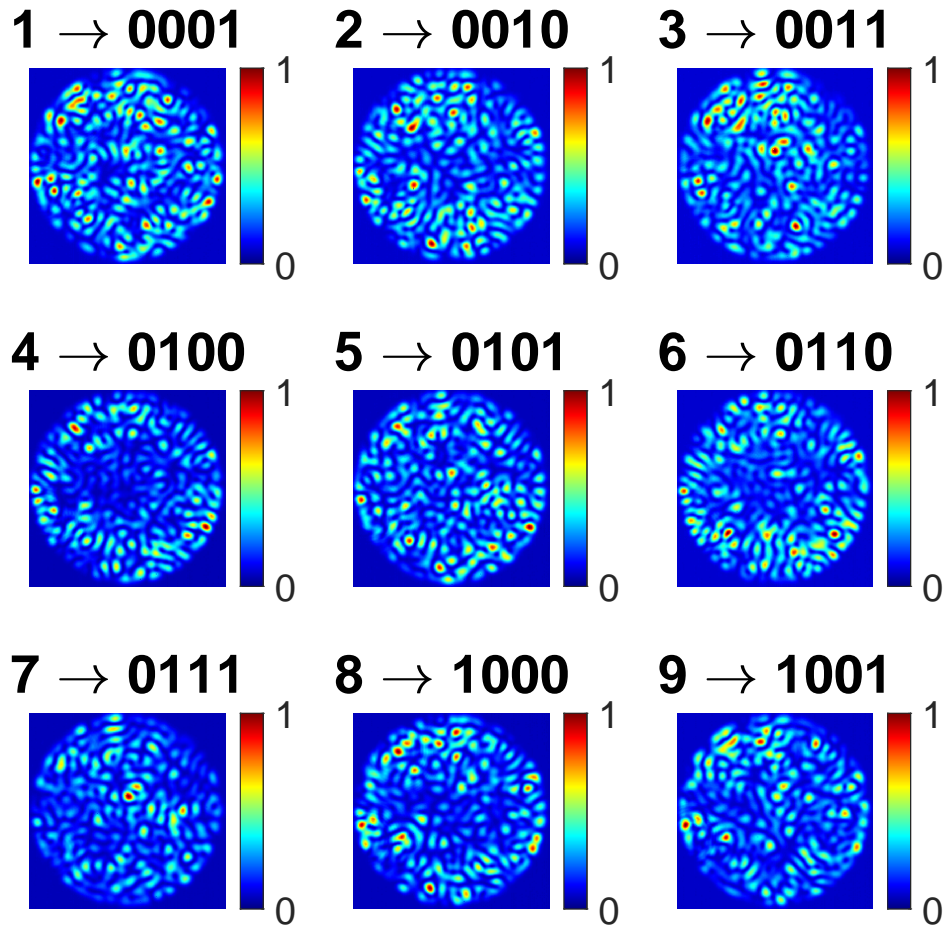
Figure 4.4: Speckle patterns obtained at the exit facet of the multimode fiber for bit strings of length four corresponding to numbers from 1 to 9. Most responsive regions of the SLM are modulated to guarantee distinct speckles. The similarity of the speckles is measured by calculating the correlation coefficients of speckles with each other.

The speckle patterns obtained in Fig. 4.4 represent distinct input information (binary numbers) and for this reason they have to be distinct in order to distinguish numbers from each other, thus to classify the numbers accurately. If the similarity between two speckles is high, the receiver can mix the corresponding numbers and translate the input message wrong. Although we have modulated the most responsive SLM regions to prevent this confusion, a more quantitative approach is to calculate the correlation between the speckles. Fig. 4.5 shows the correlation map of the speckles created by the numbers. The correlation values yield the similarity percentage of speckles, and they are calculated with the `corr2` function in MATLAB [152], which gives the Pearson correlation coefficient between two 2D arrays. The diagonal entries of the matrix

indicate the self-correlation of the speckles, and they are always equal to 1. For the rest of the entries, the minimum correlation is around 0.4; thus, two speckles created by different numbers are at least 40% similar to each other. The highest similarity occurs between the speckles created by numbers 8 and 9, with a correlation around 0.7. In general, the dominancy of the diagonal entries in the correlation matrix is a good indicator of the distinguishability of the numbers.
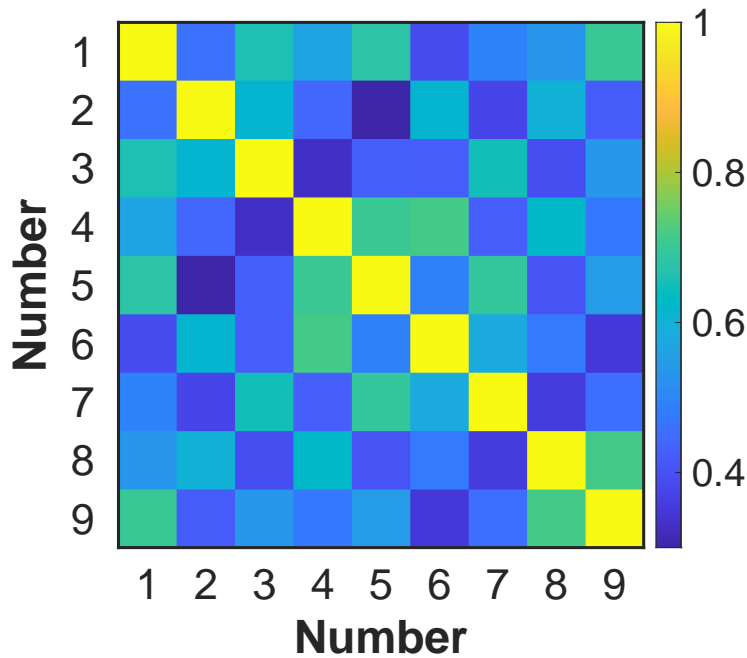
Figure 4.5: Correlation map of speckles obtained for numbers 1 to 9. The diagonality of the correlation map is a good indicator of the distinguishability of the speckles from each other. The correlation between speckles created by numbers 8 and 9 is around 0.7, which is the highest correlation between two different speckles. The correlation value yields the similarity percentage of the speckles. Thus all speckles are at least 30% different from each other in the initial configuration.
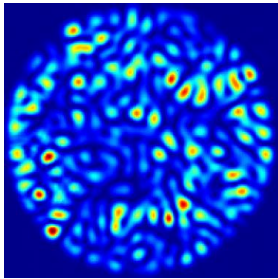
4.3 Reconstruction Method

Our decryption scheme is based on the reconstruction of the input information x in the propagation equation $y = \mathrm{T} * x$. In order to solve the propagation equation for the input x, we develop a mathematical model where the input numbers and output

speckles are represented by column vectors, and the propagation medium is modeled as a matrix. Since the system is calibrated with nine digits, the inputs are vectors of length 9×1. The input vectors are called digit vectors, and they are denoted by $\mathbf{D_i}$, where each $i = 1, 2, \ldots, 9$ corresponds to a specific digit. The indices of the digit vectors represent the digit carried by this vector, and all entries of the digit vectors are zero except for the entry at the position of the index value. Thus, the digit vectors are defined as standard unit vectors of 9 dimensional vector space, as shown below.

$$\mathbf{D_1} = \begin{bmatrix} 1 \\ 0 \\ 0 \\ \vdots \\ 0 \end{bmatrix}_{9 \times 1} \qquad \mathbf{D_2} = \begin{bmatrix} 0 \\ 1 \\ 0 \\ \vdots \\ 0 \end{bmatrix}_{9 \times 1} \qquad \mathbf{D_3} = \begin{bmatrix} 0 \\ 0 \\ 1 \\ \vdots \\ 0 \end{bmatrix}_{9 \times 1} \qquad \cdots \qquad \mathbf{D_M} = \begin{bmatrix} 0 \\ 0 \\ 0 \\ \vdots \\ 1 \end{bmatrix}_{9 \times 1}$$

The outputs, speckle patterns measured by the camera, have two-dimensional structures and are originally represented by 2D matrices. We reshape the speckle matrices into column vectors $\mathbf{I_i}$ and call them intensity vectors, where $i = 1, 2, \ldots, 9$ specifies the input number (1 to 9) created that speckle. If the speckle image has a resolution of $m \times n$, then the original speckle matrices will have $m \times n$ dimensions, and the intensity vectors will have $(m \times n) \times 1$ dimensions.

$$\longrightarrow \begin{bmatrix} 11 & 15 & 12 & \ldots & 10 \\ 20 & 14 & 10 & \ldots & 13 \\ 10 & 16 & 15 & \ldots & 12 \\ \vdots & \vdots & \vdots & \ddots & \vdots \\ 13 & 18 & 12 & \ldots & 11 \end{bmatrix}_{m \times n} \xrightarrow{\text{reshape}} \mathbf{I_i} = \begin{bmatrix} 11 \\ 15 \\ 12 \\ \vdots \\ 11 \end{bmatrix}_{(m \times n) \times 1}$$

After modeling the inputs and outputs as column vectors, a propagation equation between the digit vectors and the intensity vectors can be written as

$$\mathbf{I_i} = \mathbf{T} * \mathbf{D_i}, \tag{4.1}$$

where $\mathbf{T}$ is a $(m \times n) \times 9$ dimensional matrix known as calibration matrix (also called propagation matrix or transmission matrix), and "$*$" denotes the matrix multiplication.

45

Since digit vectors are modeled as unit vectors in the standard basis of 9-dimensional vector space, the propagation equation can only be satisfied if the columns of the calibration matrix are constructed from the intensity vectors. Below, we show the matrix form of the calibration matrix (on the left) and a visualization of the calibration matrix obtained in the experiment for nine numbers (on the right).

When the speckles of all nine digits are captured, the calibration matrix $\mathbf{T}$ can easily be constructed as described above. The calibration matrix can then be used to reconstruct the unknown digits. In practice, the user will have the intensity vector, $\mathbf{I_u}$, created by the unknown input digit, together with the calibration matrix $\mathbf{T}$. In this case, the unknown digit vector, $\mathbf{D_u}$, can be obtained by inverting the propagation equation, Eq. (4.1),

$$\mathbf{D_u} = \mathbf{T}^{-1} * \mathbf{I_u}. \tag{4.2}$$

4.4   Results

The calibration matrix, obtained with the process described in the previous section, is used as the key between the sender and the receiver. Each time the sender wants to transmit a message consisting of the digits from 1 to 9, she uses the same encryption steps and generates speckles. The receiver takes the message in the form of speckles and uses the key (the calibration matrix) to decrypt the message. Fig. 4.6 and Fig. 4.7 show the confusion charts showing the long-term performance of the cryptographic messaging system. The numbers inside the charts are the prediction accuracies of the digits (evaluated over one), measured at different time labels ranging from 5 minutes to 30 hours. The diagonal entries correspond to correct predictions, and the diagonality of the confusion charts is a sign of accurately working encryption/decryption scheme between the sender and the receiver.

The reconstruction error, μ, denoted on top of the confusion charts is calculated as

$$\mu = \sqrt{\frac{1}{9}[\mathbf{D_u^{actual}} - \mathbf{D_u^{reconstructed}}]^2} \, , \tag{4.3}$$

where $\mathbf{D_u^{actual}}$ is the true digit sent by the sender, and $\mathbf{D_u^{reconstructed}}$ is the digit recon-structed and read by the receiver after using the inverse propagation equation Eq. (4.2). The average reconstruction error of the encrypted messaging system increases from 1.8% to 11.9% in 30 hours. Yet, the confusion chart obtained after 30 hours still shows diagonal behavior. Thus, if the sender and receiver agree on accepting the digit which has the highest prediction ratio as the correct digit, then the messaging can be maintained securely even after 30 hours.

The preliminary results presented in this chapter can be improved by testing the performance of the system for longer times. The security level and the duration of validity of the messaging can be increased further by using distinct phase values, i.e., distinct gratings, for each number, which is expected to decrease the similarity of the speckle patterns. Furthermore, a more advanced encryption system can be developed by changing the position of the modulated grating windows on the SLM screen. Such a system brings extra security with the cost of an enlarged calibration set and longer calibration time, but it can also be used in advanced classification tasks.
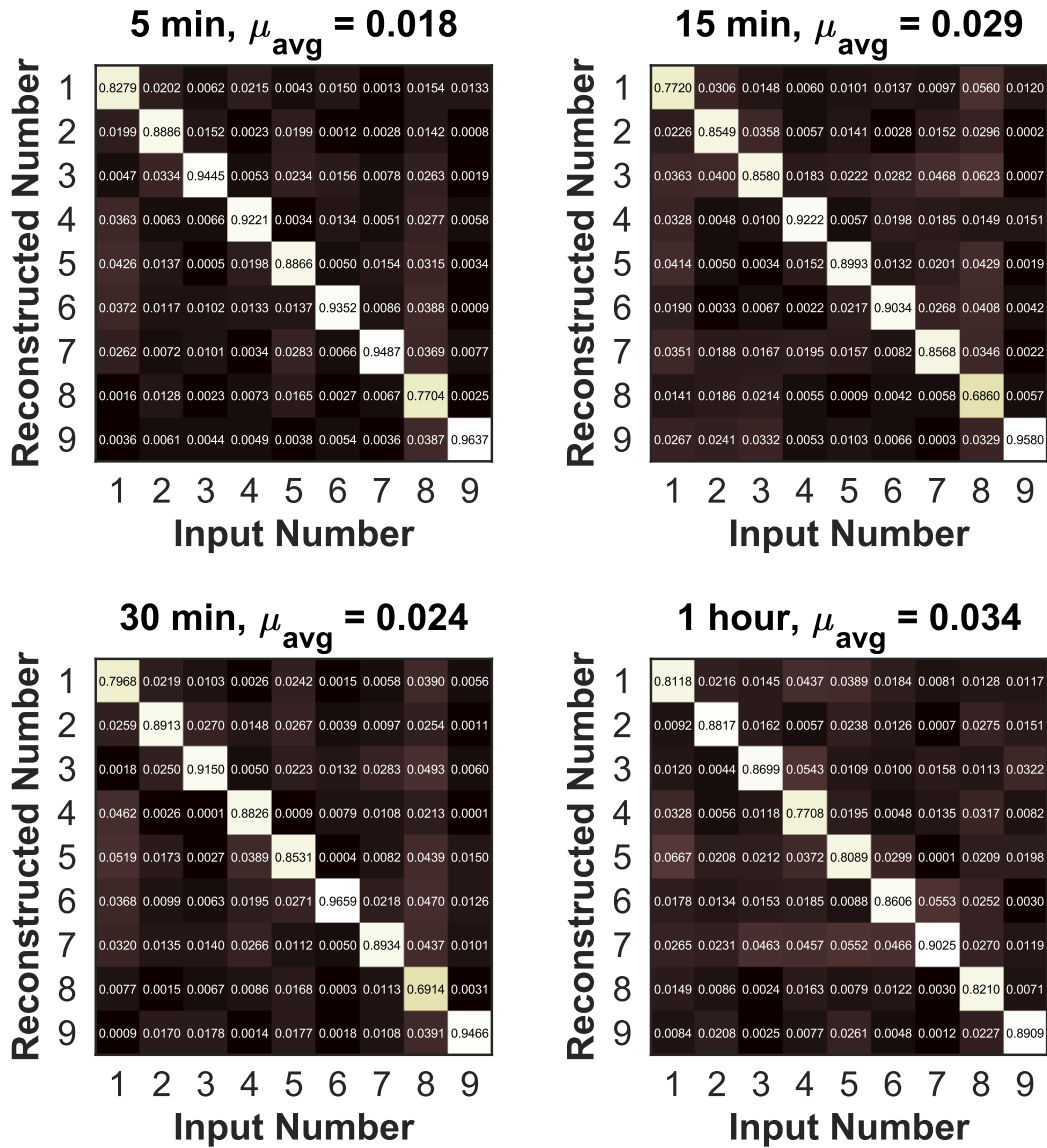
Figure 4.6: Confusion charts of the message delivery system after 5 min, 15 min, 30 min, and 1 hour. The average reconstruction error, μ_{avg}, which is found by averaging the individual errors of all digits, does not show a structured behavior in the first 30 minutes but then increases monotonically.
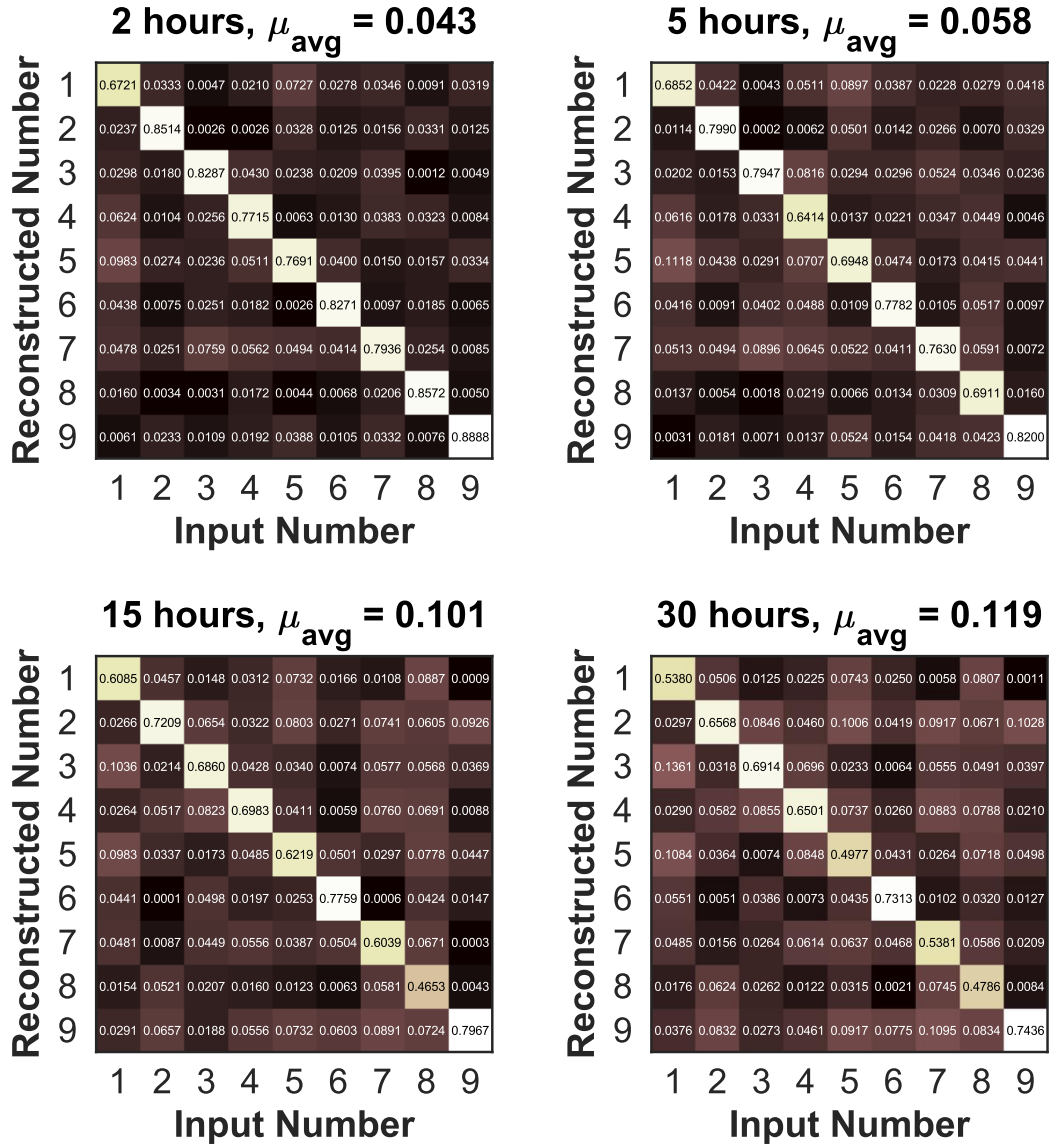
Figure 4.7: Confusion charts of the message delivery system after 2 hours, 5 hours, 15 hours, and 30 hours. The average reconstruction error increases from 4.3% to 11.9% in 28 hours.

CHAPTER 5

DEEP LEARNING BASED IMAGE TRANSMISSION THROUGH A MULTIMODE FIBER

The content presented in this chapter is adapted from the published version:

- S. Kurekci, A. T. Temur, M. E. Odabas, G. Afshari, and E. Yüce, "Deep learning-based image transmission through a multi-mode fiber," Proc. SPIE 11351, Unconventional Optical Imaging II, 1135126 (2020)

Image transmission through a multi-mode fiber is a difficult task, given the complex interference of light through the fiber that leads to random speckle patterns at the distal end of the fiber. With traditional methods and techniques, it is impractical to reconstruct a high-resolution input image by using the information obtained from the intensity of the corresponding output speckle alone. In this work, we train three Convolutional Neural Networks (CNNs) with input-output couples of a multi-mode fiber and test the learning with images outside the learning set. The three implemented deep learning models have modern UNet, ResNet, and VGGNet architectures and are trained with 31,200 gray-scale handwritten letters of the Latin alphabet. After the training, 5,200 images outside the learning set were used for testing, and it was shown that the models successfully reconstructed the input images with average fidelities ranging from 81% to 90%. Our results show the superiority of the ResNet-based architecture over UNet and VGGNet in reconstruction accuracy, achieving up to 97% fidelity in a short amount of time. This can be attributed to the success of the ResNet architecture in learning non-linear systems compared to its counterparts. We believe that the implementation of machine learning techniques to imaging, along with its contributions to biophysics, can reshape the telecommunication industry and thus will be a cornerstone in future optics and photonics studies.

5.1 Introduction

Transmitting a high-quality image through a fiber has important implications in optical communications and biological applications such as endoscopy and neuroimaging. Single mode fibers (SMF) allow propagation of a single spatial mode, which can carry only one-pixel image information. For an advanced everyday image having many more pixels, a bundle of SMFs can be used for image transmission. Yet, using a bundle of single-mode fibers is not practical for endoscopic applications due to the inevitable low resolution they possess. Compared to single-mode fibers, a multimode fiber (MMF) supports many more propagation modes which, in theory, allows the transmission of an image with a high number of pixels. However, image transmission through an MMF is not an easy task since interference between guided modes forms a seemingly random speckle pattern at the exit facet of the fiber. Local deformations along the fiber also increase the complexity of this task. Thus, to recover any information related to the image sent through a multimode fiber, the mathematics behind the transmission must be understood. Recent studies for understanding transmission through a multimode fiber concentrate on measuring the transmission matrix of the fiber [153, 154] or building a deep neural network that learns the mapping between the transmitted images and output speckles.

The studies for adapting a neural network for image recognition in a multi-mode fiber started in 1991 by Aisawa et al. [155] and are continuously drawing increased attention [156, 157]. In these preliminary works, the constructed neural network algorithms were primitive compared to modern deep neural networks. When modern architectures, such as UNet, ResNet, and VGGNet [1] based deep neural networks, were used for image transmission through a multi-mode fiber, significant results were obtained. The trials over different fiber lengths between 0.2 m and 10 m, where two separate neural networks were used for reconstruction and classification of hand-written letters, showed the success of deep learning algorithms in multi-mode fiber image transmission with reconstruction fidelities up to 97% [158]. In the same study, it was also shown that for a 1-km-long fiber, due to high interference between the spatial modes inside the fiber, the success rate of the network in classifying the images was reduced dramatically,

---

[1] As a sidenote in nomenclature, we would like to state that throughout the text, *XNet* should be understood as *XNet based architecture*.

although the reconstruction rate was still at the levels of 90%. A simulation result showing the capability of deep neural networks in constructing both the amplitude and the phase of the MMF input came very shortly after that [159]. In this work, rather than experimentally captured images, the models were trained with the input-output pairs obtained from the transmission matrix of the fiber. Moreover, it was shown that after training, deep neural networks were able to reconstruct images that come from a different distribution than those in the training set. The learning was successfully transferred with fidelities around 90%, and the supremacy of ResNet over VGGNet was shown in terms of computation time. However, the image reconstruction accuracy of the two networks was shown to be very similar. An exciting study about transmitting real-time images and videos through a multi-mode fiber was also published recently, where the transmission matrix of the fiber was statistically measured by a single-layer deep learning algorithm [160].

Image reconstruction after transmission through a multimode fiber turns into a particularly difficult task when an intensity-only measurement is done. In this approach, the neural network needs to find the nonlinear relation between the output speckle intensity and the input electric field. After being illuminated with the laser light, the letters are carried to the multimode fiber as an electric field of amplitude A and phase ϕ,

$$E_{\text{in}} = Ae^{i\phi}, \tag{5.1}$$

and, after the transmission along the fiber, they are recorded on a camera as an intensity distribution

$$I_{\text{out}} = |E_{\text{out}}|^2 = |T * E_{\text{in}}|^2, \tag{5.2}$$

where T is the transmission matrix of the fiber. Therefore, when fed with the output intensity I_{out}, the objective of the neural network is to correctly reconstruct the amplitude A and the phase ϕ of the input electric field E_{in}.

In this work, we reconstruct the images at the proximal end of a multimode fiber from the corresponding speckle patterns by executing three different modern neural networks and compare their performances. We first construct the ResNet and VGGNet-based architectures [159] and then the UNet-based architecture [158]. Our results show the superiority of ResNet architecture in solving the multimode fiber image transmission

problem compared to the other two tested networks. Higher reconstruction fidelity and convenient computation time obtained from ResNet also promises better results when the network is applied to other nonlinear inverse problems having complex inner structures such as speckles. To the best of our knowledge, the three architectures underlined in this study have never been compared for the same system.

5.2   Deep Learning

Deep learning is an implementation of Machine Learning that makes use of biologically inspired *artificial neural networks* to perform specific tasks on given data without explicit instructions, relying on inferences made from the data itself. Artificial neural networks (ANN) are used to model functions or transformations and are essential connections of primitive computational units called *neurons*. Neurons receive signals and process them based on their internal adjustable parameters (weights and biases), then pass them through what are called *activation functions* and onto other neurons. Activation functions are generally used to allow the output signal to be nonlinear and are especially important in solving complex nonlinear problems. The general form of the propagation function of an artificial neuron with input signal x and output signal y is given as

$$y = \mathbf{g}(w * x + b), \tag{5.3}$$

where w is the weight, b is the optional bias term, and $\mathbf{g}$ is the activation function of the neuron.

In supervised deep learning, the goal is to model the mapping from a given set of inputs to a given set of outputs using ANNs that consist of multiple layers of neurons. The output of the final layer of an ANN is called the prediction and is expected to match the target output. However, the parameters of the ANN are randomly initialized and need to be *learned* by the network. The process of learning is the adjustment of these parameters, using *backpropagation*, to minimize a *loss (cost) function* that represents the difference between the prediction and the target output. The backpropagation algorithm computes the gradient of the loss function with respect to each network parameter, then slightly readjusts the parameters in the direction of the steepest descent.

The readjustment of some network parameter w can be formulated as

$$w := w - \alpha \frac{\partial L}{\partial w}, \tag{5.4}$$

where L is the loss function and α is the *learning rate* which is the step size of the readjustment. Ideally, training continues until the loss function stabilizes, which is called *convergence*.

In our study, we use the Mean Squared Error (MSE) loss function

$$\text{MSE}(y, y') = \frac{1}{N} \sum_{j=1}^{M} \sum_{i=1}^{N} \left(y_{i,j} - y'_{i,j} \right)^2, \tag{5.5}$$

computed pixel-wise between real input patterns and network predictions, where N is the number of examples (input-output image pairs), M is the number of pixels in each image, and y and y' represent the real and predicted images, respectively.

In order to objectively measure the performance of a network, the data is divided into two sets. One of these sets, called the *training set*, is used in backpropagation, whereas the other one, called the *validation set*, is used for evaluation. This is done to show that the model has not simply memorized the input-output pairs from the training set but has instead learned the mapping between them.

To further demonstrate our models' ability to approximate the mapping without memorization and to provide a more human-readable evaluation metric, we calculate the Pearson correlation coefficients,

$$P(y, y') = \frac{\sum_{j=1}^{M} \sum_{i=1}^{N} \left(y_{i,j} - \bar{y} \right) \left(y'_{i,j} - \bar{y}' \right)}{\sqrt{\sum_{j=1}^{M} \sum_{i=1}^{N} \left(y_{i,j} - \bar{y} \right)^2} \sqrt{\sum_{j=1}^{M} \sum_{i=1}^{N} \left(y'_{i,j} - \bar{y}' \right)^2}}, \tag{5.6}$$

between the predicted images y' and the ground-truth images y.

5.2.1 Convolutional Neural Networks

Many traditional image processing algorithms rely on handcrafted filters that are used to extract certain features from given images through convolution operations. These features range from extremely basic ones, such as horizontal and vertical lines, to more complex ones, such as complicated shapes or even human faces. However,

handcrafting the filters required to extract relevant features for a sophisticated image-processing task often proves to be an insurmountable problem. A deep learning-based solution to this problem is proposed in the form of Convolutional Neural Networks (CNN), which consist of learnable filters made up of neurons. Filters for extracting both low and high-level features can be learned through backpropagation. Many different CNN architectures have been designed over the years to overcome various obstacles encountered in different image-processing tasks.

Reconstructing input images from speckle patterns created by transmission through a multi-mode fiber can be considered a complex image processing problem due to its nonlinear nature. Therefore, any deep learning-based solution to this problem should utilize CNNs rather than other types of neural networks. Among various types of networks, models based on CNN architectures ResNet, VGGNet, and UNet have already been presented as solutions.

5.3 Experimental Setup

A simple schematic of the experimental setup is given in Fig. 5.1. A diode laser operating at 671 nm is used for illuminating the screen of a 1280x768 pixel Spatial Light Modulator (SLM). 31,200 gray-scale handwritten letters from the Latin alphabet (taken from the EMNIST-Letters dataset [161] as 28x28 pixel images) are written on the SLM by modulating the phase and the amplitude of the incoming laser light. The letters on the SLM are transmitted through a stable 2-meter-long multimode fiber with a core diameter of 105 μm and NA = 0.22. The speckle patterns formed at the exit facet of the fiber are recorded by a visible CCD camera (1024x768 resolution) and stored in the database. Speckle recordings are then processed by a neural network to reconstruct the input patterns.
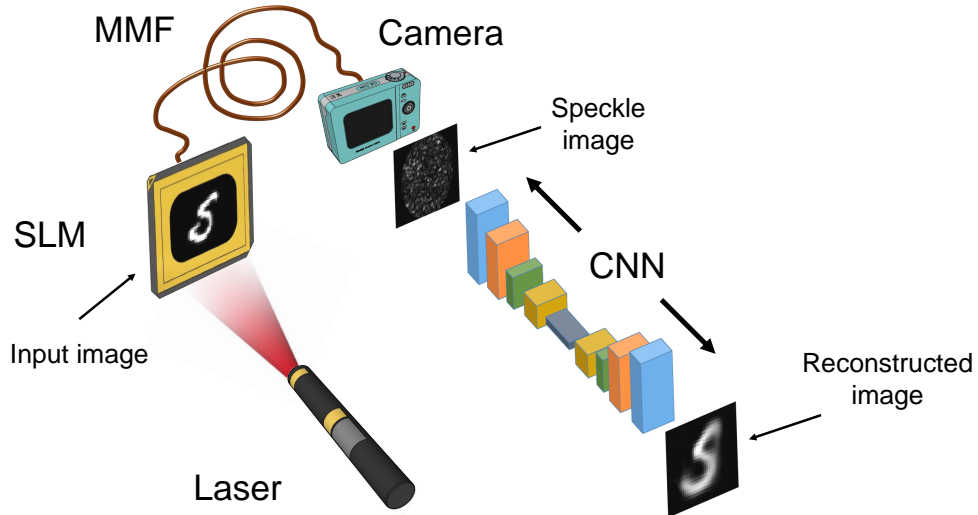
Figure 5.1: Schematic of the experimental setup used for constructing the datasets required to train the neural network and test its accuracy. The input letters sent through the multimode fiber are successfully reconstructed by the deep learning model.

5.4 Results

The required letter-speckle pairs for testing the learning capability of the networks are obtained with the setup shown in Fig. 5.1. The captured image pairs are divided into training and validation sets with 31,200 and 5,200 images, respectively, and equally distributed between 26 letters. All three networks are trained on the training set using mean squared error as the loss function. The loss function is minimized using the Adam optimizer [162] with default parameters for all three models. We trained all three of our models using a batch size (number of predictions before each optimization step) of 64 and for 100 epochs (iterations of the training set). After each epoch of training, the models are fed all speckle patterns from the validation set and asked to produce predictions. Input images from the validation set, corresponding speckle patterns, and reconstructed images by the ResNet-based network are shown in Fig. 5.2, where fidelities are denoted by r.

Moreover, the total training times, the number of layers, and the number of adjustable parameters for each model are listed in Table 5.1. VGGNet is the most complex model with 22 layers, and it has the longest training time[2]. As for the ResNet and UNet,

---

[2] All three models are trained for 100 epochs using an NVidia Tesla V100.

although the UNet has more parameters, it has a shorter training time as it has the fewest number of multiplications of neurons in one pass through the network due to its architectural design.
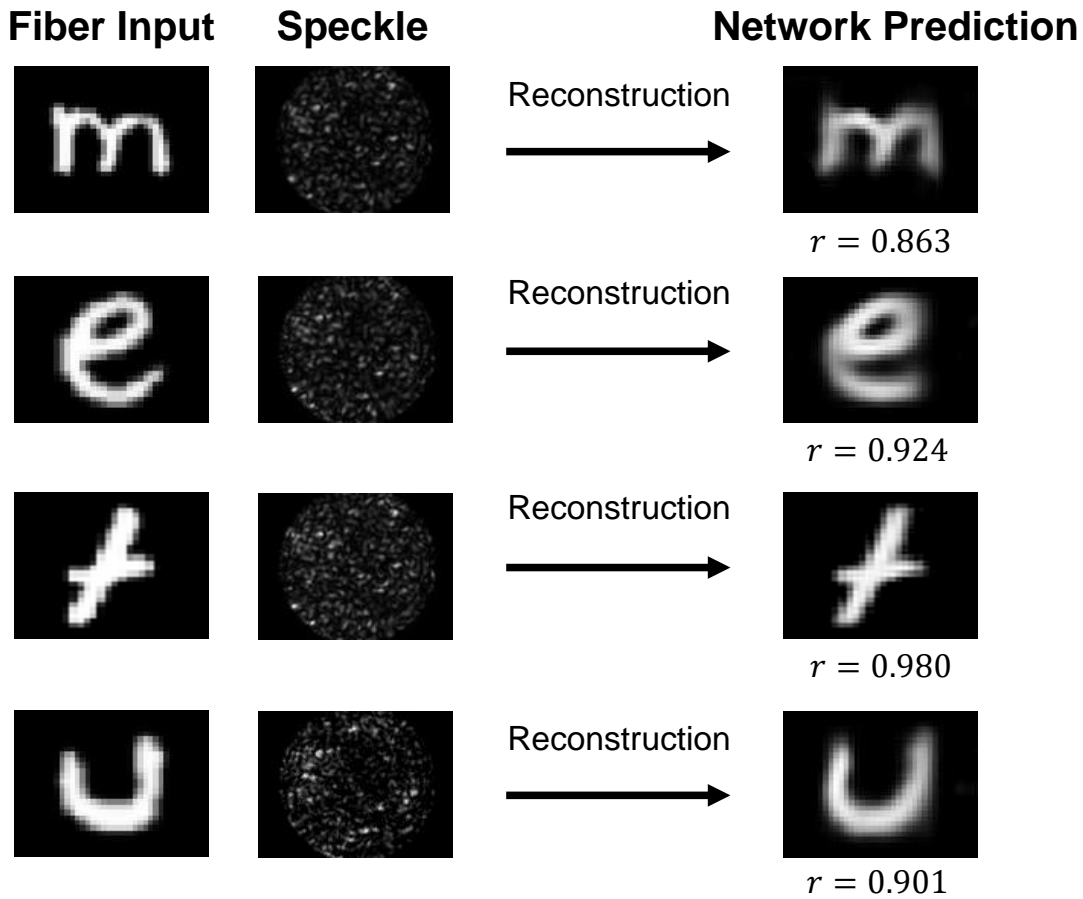
Figure 5.2: Test images reconstructed from the speckle patterns by the ResNet-based deep neural network. Numbers under the reconstructed images represent their correlations to the original input images.

Table 5.1: Number of layers, number of adjustable parameters, and total training time for each architecture.

Model Name	Number of Layers	Number of Parameters	Total Training Time
VGGNEt	22	3,691,457	4 h 13 m
ResNet	14	1,369,411	41 m
UNet	14	1,836,225	25 m

The predictions produced by the networks are then compared with their ground truth fiber inputs to compute the mean squared error values in Fig. 5.3. It can be seen from the figure that the ResNet and the UNet both converge (minimize validation set loss) in less than 20 epochs, after which their validation set losses very slightly increase while their training losses keep decreasing. This phenomenon is called overfitting in deep learning, and it occurs due to the model memorizing specific features of the training set rather than capturing its general features. It is expected that models start overfitting the training set after they reach a minimum validation loss. The reason we see less divergence between the training and validation loss curves in the VGGNet is that it simply has not converged yet.

In order to provide a better metric for our predictions, we calculated the Pearson correlation coefficients between predicted and ground truth images. The average correlation coefficients for the training and validation sets after each epoch is plotted in Fig. 5.4. We can see that the ResNet produces results with up to 90% correlation on average and converges more quickly compared to the other networks.
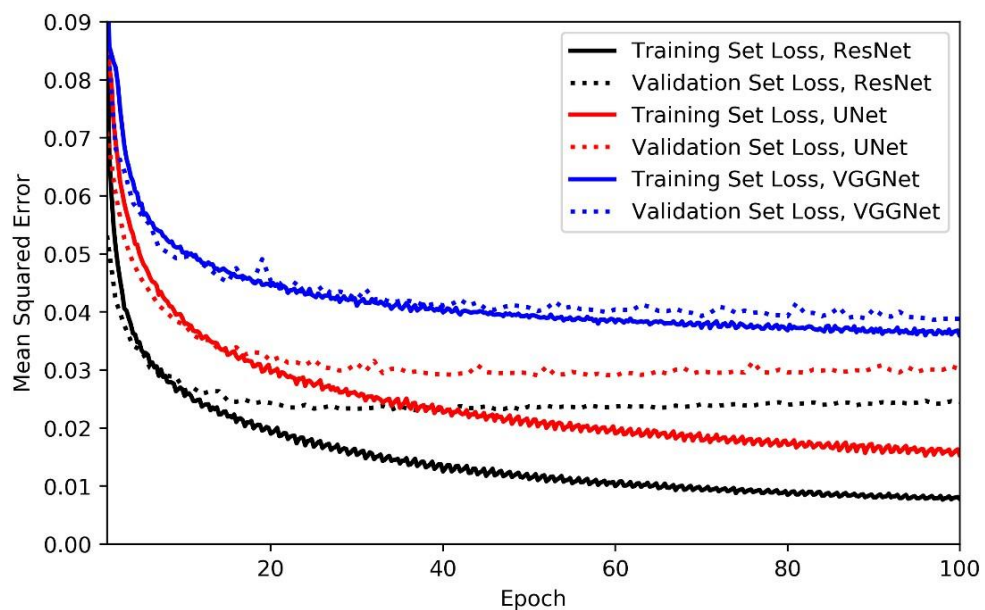
Figure 5.3: MSE loss on both training and validation sets after each epoch for the ResNet, UNet, and VGGNet-based networks. The ResNet-based network converges faster than its counterparts and yields better results.
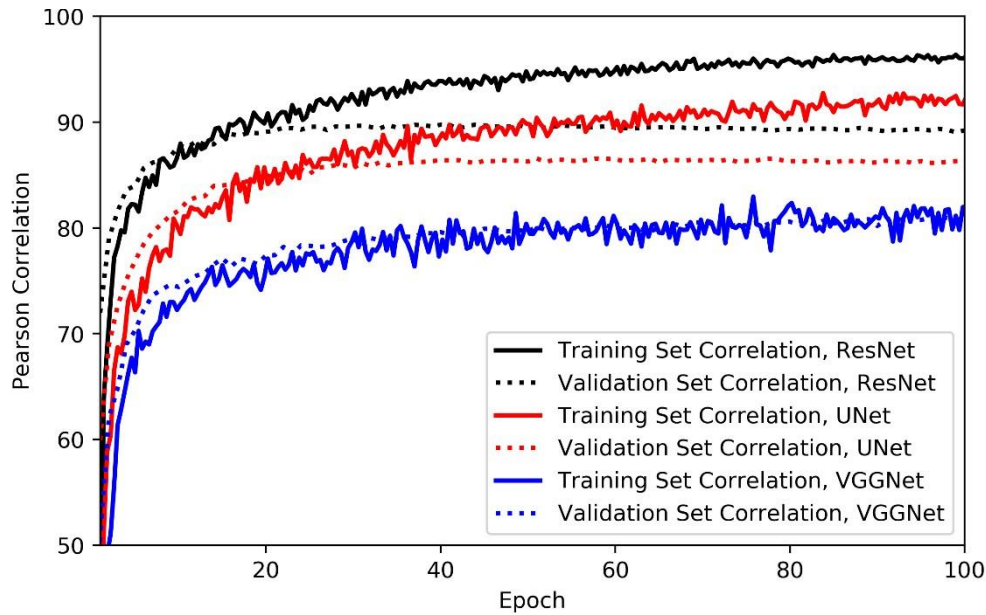
Figure 5.4: Average Pearson correlation coefficient (multiplied by 100) between pairs of predicted and ground truth images for the ResNet, UNet, and VGGNet-based networks after each epoch.

5.5 Comments

The ResNet and the UNet are encoder-decoder architectures where the input features get stacked and represented in smaller matrices in the encoder part and then progressively decoded to reconstruct the MMF input (Fig. 5.5). Unlike these two models, the VGGNet architecture preserves the input shape through the network by reshaping layers. We believe that VGGNet is less suitable for this problem due to its architecture and high complexity.

The skip connections in the ResNet add the values of the previous layer to the output of the following layer, whereas, in the UNet, they concatenate (append matrices along an axis) the values of the encoding layers to specifically chosen decoding layers. Skip connections are generally used in networks with large numbers of layers to overcome issues with backpropagation. For our problem, we did not observe a significant difference in the learning process of either network due to the presence of skip connections. The training and validation results for the ResNet with and without the skip connections can be seen in Fig. 5.6.
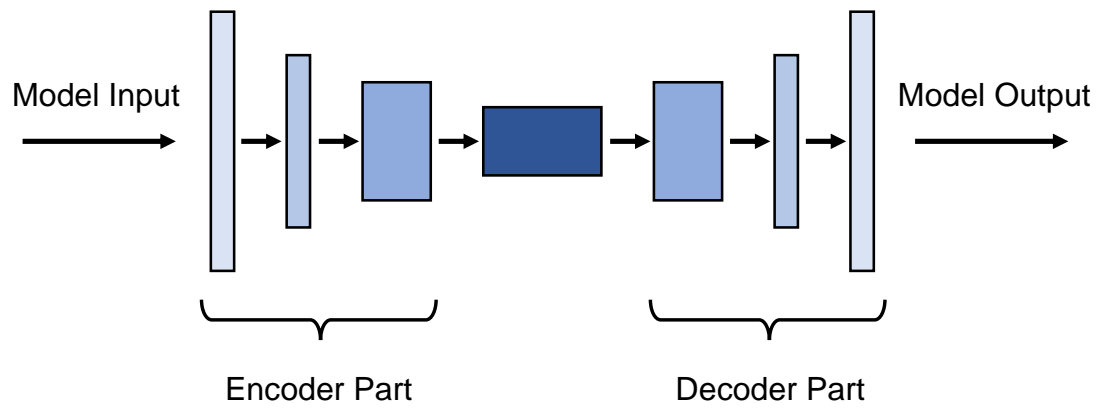
Figure 5.5: A simple schematic showing an encoder-decoder architecture. Progressively higher-level features are extracted from the input in the encoder part to be decoded later to create the prediction.
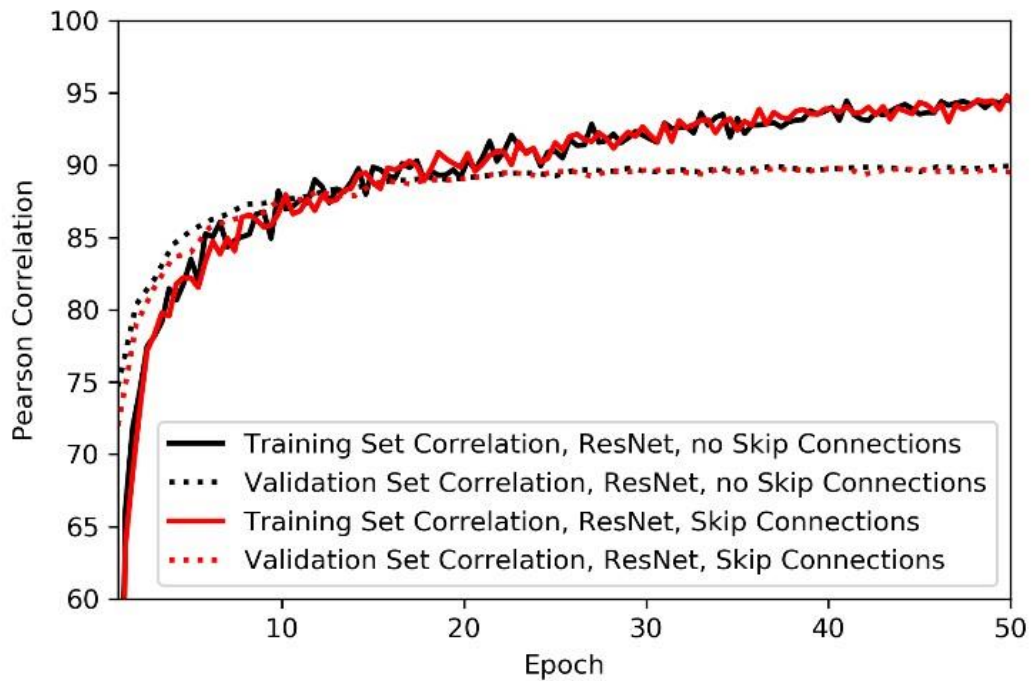
Figure 5.6: Average Pearson correlation coefficients (multiplied by 100) between pairs of predicted and ground truth images for the ResNet-based network **(a)** with and without skip connections

We believe that part of the reason behind the faster convergence and superior results of the ResNet is the utilization of Batch Normalization layers in the network. Batch Normalization layers standardize the layer activations, making the optimizer function more smoothly. They also stabilize the gradient flow and increase the robustness of the network to different hyperparameters, and random initializations [163]. When we trained the ResNet without the Batch Normalization layers, we obtained lower fidelities and slower convergence, as shown in Fig. 5.7.
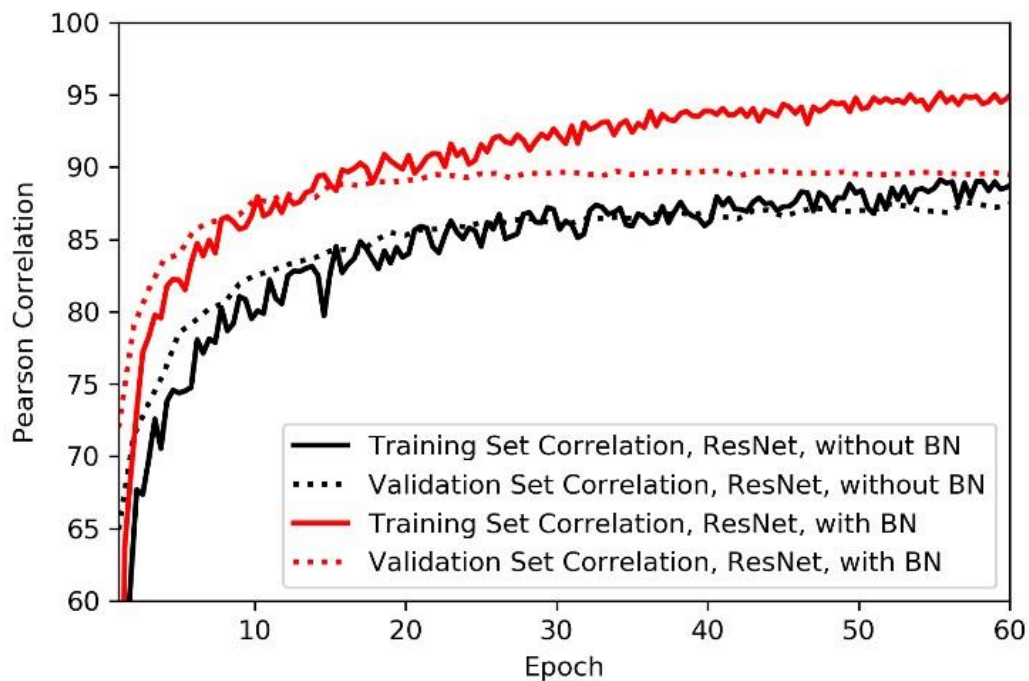
Figure 5.7: Average Pearson correlation coefficients (multiplied by 100) between pairs of predicted and ground truth images for the ResNet-based network with and without batch normalization layers computed after each epoch.

5.6 Conclusion

Our results show the superiority of the ResNet-based architectures over the other two networks, UNet and VGGNet, in terms of accuracy in reconstructing the input images that are transmitted through a multimode fiber. An average reconstruction fidelity of 89.8% was obtained for the validation set by using the ResNet architecture, while it was 86.6% for the UNet and 81% for the VGGNet. Utilization of Batch Normalization layers was shown to be a significant contributing factor to the superiority of the ResNet-based architecture. We believe that the evaluation of different architectures from various aspects may give researchers an opinion on whether to apply these algorithms in their field and may give rise to different application areas for machine learning tools. However, the study of deep learning-based solutions to our problem should not be limited to a study of different architectures but of different approaches like semi-supervised or unsupervised learning or generative models.

CHAPTER 6

MULTIMODE FIBER SPECTROMETER

In this chapter, we introduce a high-resolution, compact, low-cost, and low-loss spectrometer based on the speckle measurements obtained at the distal end of a multimode fiber. We start the chapter by reviewing conventional spectrometers and highlighting the trade-offs between the resolution, size, and cost of such systems. Next, we prove the principle of fiber spectrometers by measuring the response of the speckle pattern to the change in the wavelength of light coupled to the fiber. We then introduce the mathematical model used to investigate the propagation equation, where the input (spectrum) and output (speckle) of the fiber are related via a calibration matrix. We explain the construction of the calibration matrix in detail and demonstrate the reconstruction process with a simulated spectrum involving two discrete wavelengths. In the final section, we test the performance of the spectrometer with experimental data and show the reconstruction of three different types of input sources. Our results show that a multimode fiber spectrometer can resolve two lines with 10 pm separation, which corresponds to a record resolving power of $R \approx 10^5$ at the telecom wavelengths. We also show that the reconstruction error of the spectrometer for a continuous broadband source increases as the bandwidth of the signal increases, reaching $\sim 9\%$ when the bandwidth covers 20% of the whole calibrated spectral range.

6.1 Conventional Spectrometers

Spectroscopy can be defined as the method of understanding the spectra (the wavelength content) of a light source or the spectra created after light-matter interaction. Being a vital technique for developing a scientific understanding of light and matter, spectroscopy is used in many areas of science and technology, including characterization of light sources, atomic structure analysis [164], medical applications [165], biochemistry [166, 167], material science [168], and optical communication technology [169, 170]. Conventional spectroscopy is based on the dispersion of light, which is the relation between the phase velocity and the wavelength. In material dispersion, the phase velocity of light changes when the propagation medium changes, thus, for example, when light undergoes refraction. Therefore, as a result of dispersion, different wavelengths (colors) travel in different directions across a medium; thus, the dispersion property of the light can be used to split light into its constituent wavelengths. This effect can be easily observed in the chromatic aberration of lenses and in the refraction of light through a prism, as shown in Fig. 6.1(a) and Fig. 6.1(b). Due to the relation between the phase velocity v_p of light within a medium and the refractive index n of that medium ($v_p = c/n$, where c is the speed of light), the material dispersion can also be considered as the change in the refractive index of the materials with wavelength. Fig. 6.1(c) shows the refractive index change of various optical glasses commonly used in manufacturing lenses and prisms with respect to wavelength.
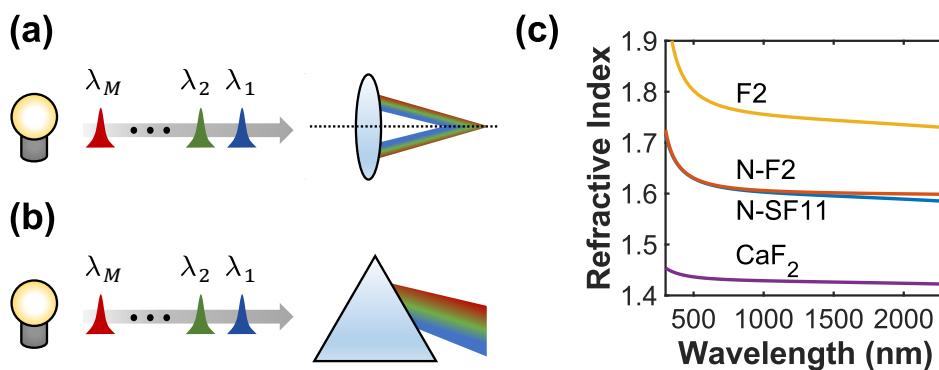
Figure 6.1: **(a)** Dispersion of light in a lens results in chromatic aberration. **(b)** Due to dispersion, light can be separated into its constituent wavelengths. **(c)** Dispersion curves of some optical glasses commonly used in manufacturing lenses and prisms.

Due to their material dispersion property, prisms are extensively used in conventional spectroscopic analysis. Diffraction gratings are another widely preferred option for building conventional spectrometers, which separate light into wavelengths by using the angular dispersion of light occurring after diffraction. A diffraction grating consists of multiple slits (or grooves), as shown in Fig. 6.2, and when a planar wavefront encounters this structure, spherical wavelets are emitted from each slit due to the bending of the wavefront. The spherical wavelets then overlap and create constructive and destructive interference, which results in a fringe pattern. In the case of polychromatic light, different wavelengths constructively interfere at different positions in space as a result of the grating equation,

$$m\lambda = d(\sin \alpha + \sin \beta), \tag{6.1}$$

where d is the distance between the slits (or grooves) of the grating, m is the diffraction order, α and β are incident and diffracted angles, respectively.
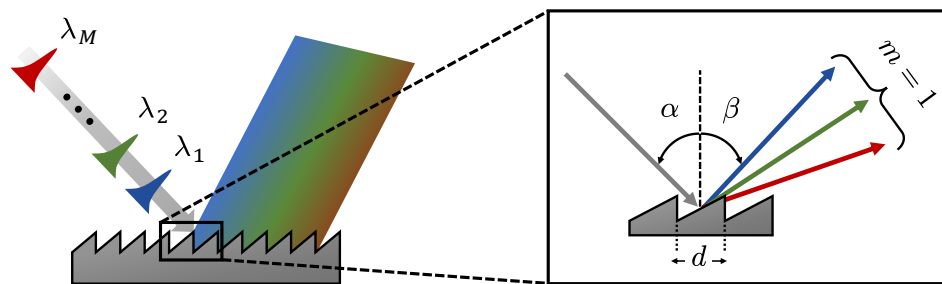
Figure 6.2: Schematic drawing of a reflection diffraction grating. The grating separates the input light into its constituent wavelengths by diffraction. Depending on the grating groove separation d and the incident angle α, a specific wavelength λ diffracts with a distinct angle β at diffraction order m.

There are many critical aspects to consider when building a spectrometer, including the resolution, size, cost, and stability of the system. The resolution of the spectrometer is defined as its ability to separate adjacent wavelengths, and in conventional spectrometers, the resolution generally depends on the quality of the equipment or the optical path length of the dispersed light. In the case of prisms, high-quality prism materials lower the unwanted effects (such as the absorption and reflectance of light), hence resulting in higher resolutions. In the case of diffraction gratings, when the number of lines in

67

the grating is increased, the resolution also increases. However, using high-quality equipment (high-quality prism materials or gratings with high lines/mm) increases the cost of the system. The other parameter defining the higher resolution is the optical path length. As the path that light travels after the grating increases, the resolution also increases. In conventional spectrometers with conventional diffraction gratings, optical path length can be changed by either changing the position or orientation of the grating. In either case, the mechanical motion causes instabilities and noise in the measurements, and it may also lead to alignment problems. Although increasing optical path length is more cost-effective compared to using high-quality equipment, it causes the volume of the spectrometer to increase. Thus, the compactness of the spectrometer is lost.

6.2 Multimode Fiber Spectrometers

For all the aforementioned reasons, there is a huge interest in building miniaturized, low-cost spectrometers [171–179]. Among these efforts, speckle-based spectrometers [180–184], and particularly multimode fiber spectrometers are of interest to us in the context of this thesis. The idea of using a multimode fiber in spectroscopic analysis dates back to the 80s [185, 186], but it gained popularity very recently with a series of papers published during the years 2012-2016 [187–195]. Compared to conventional spectrometers, multimode fibers offer low-cost systems, and since fiber cables can be coiled, the optical path length can be increased easily without compromising the compactness of the system. Therefore, multimode fibers can be utilized to build low-cost, compact, and high-resolution spectrometers with very low loss.

Unlike a conventional spectrometer, which maps the input spectral channels (wavelengths) to distinct space points in one-dimension, a multimode fiber spectrometer is a two-dimensional spectral-to-spatial instrument. As seen in Fig. 6.3, a distinct speckle pattern is formed at the distal end of a multimode fiber for different input wavelengths. This effect can be explained with the wavelength-dependent propagation constants of the fiber modes as the field coupled to the fiber gains an extra phase proportional to $e^{\beta(\lambda)}$ when the input wavelength changes (see Chapter 2 for more details).
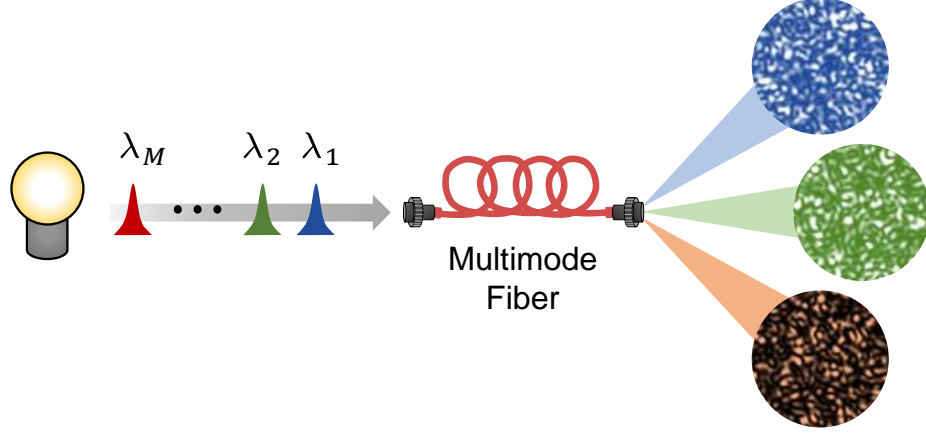
Figure 6.3: A multimode fiber can be used for spectroscopic analysis since different input wavelength creates distinguishable speckle patterns at the distal end of the fiber.

The sensitivity (or response) of the speckle patterns to the wavelength of light is the key building block behind the idea of building a multimode fiber spectrometer. This sensitivity can be calculated analytically by using the correlation function of speckles captured under different wavelengths. The two-dimensional Pearson correlation coefficient between two speckles A and B is given as

$$r = \frac{\sum_m \sum_n (A_{mn} - \bar{A})(B_{mn} - \bar{B})}{\sqrt{\sum_m \sum_n \left(A_{mn} - \bar{A}\right)^2}\sqrt{\sum_m \sum_n \left(B_{mn} - \bar{B}\right)^2}}, \tag{6.2}$$

where m and n are the horizontal and vertical pixels of the speckle image, and the bar denotes the average over all pixels. In [188], a slightly different intensity correlation metric is defined to measure the speckle correlations,

$$C(\Delta\lambda, x) = \frac{\langle I(\lambda, x)I(\lambda + \Delta\lambda, x)\rangle}{\langle I(\lambda, x)\rangle\langle I(\lambda + \Delta\lambda, x)\rangle} - 1, \tag{6.3}$$

where $I(\lambda, x)$ is the intensity of the speckle at position x, created by wavelength λ, and $\langle \ldots \rangle$ represent averaging over all wavelengths. Both correlation functions can be used to measure the decorrelation of speckle images under wavelength variations. For the case of a fiber spectrometer, spectral resolution is the minimum shift in the wavelength sufficient to reduce the degree of correlation of the speckle pattern to 0.5 [188]. In Fig. 6.4, we show examples of speckle patterns and the correlation curves of these speckles calculated for both approaches given by Eq. (6.2) and Eq. (6.3). The speckle patterns in the figure are obtained for $\lambda = 1550.2$ nm, $\lambda = 1550.205$ nm, and

$\lambda = 1550.210$ nm, respectively. The correlation coefficient of the first speckle with the second one is $r = 0.8548$, which implies that our system is not able to distinguish wavelengths separated by 5 pm. However, the correlation reduces below 0.5 when the wavelength is shifted by 10 pm ($r = 0.4696$). Thus, the system is able to distinguish these wavelengths. A more accurate spectral resolution can be calculated by observing the correlation curves in Fig. 6.4(b)-(c), where a full-width at half-maximum (FWHM) value around 9 pm is obtained for both correlation functions. Therefore, it can be safely claimed that such a system can be used as a spectrometer with $\sim$9 pm resolution.
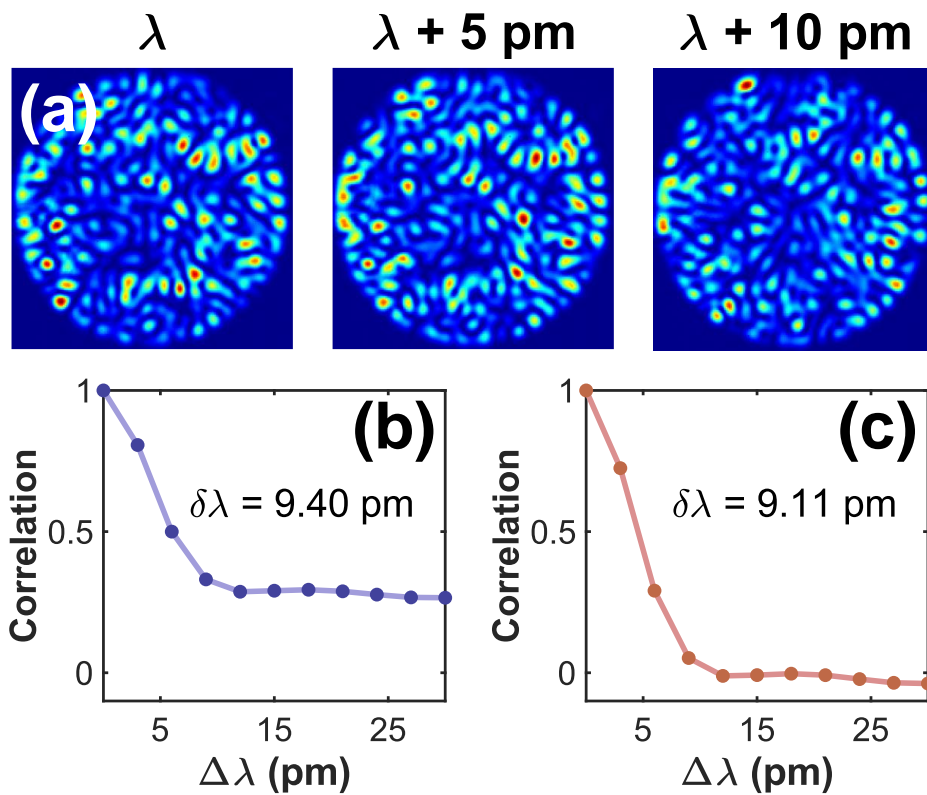
Figure 6.4: Decorrelation of speckles for a 20 meters long fiber (core size = 105 μm, NA = 0.22). **(a)** Speckle images obtained for 1550.2 nm, 1550.205 nm, and 1550.205 nm. Although the correlation between the speckles is high when the wavelength separation is 5 pm, it reduces below 0.5 when the wavelength is shifted by 10 pm. **(b)** Correlation curve obtained by using Pearson correlation function. **(c)** Correlation curve obtained by using intensity correlation function. Both correlation functions imply a spectral resolution, $\delta\lambda$, around 9 pm.

6.3 Experimental Details

Although the use of a spatial light modulator is not required for the purpose of building a fiber spectrometer, we used the same setup given in Fig. 3.1, which was developed for other applications presented in this thesis involving the modulation of light. A fiber spectrometer can be built with a much simpler setup where a spatial light modulator and other optics are not used. Expanding/shrinking the beam and filtering the zeroth order diffraction is also not required. The only consideration is to achieve a good coupling of light to the multimode fiber by keeping the polarization of the input light the same for all wavelengths. The ideal simplified version of the setup used in [188] is shown in Fig. 6.5. Although we kept the SLM in the setup, we did not program it by any means (in this case, it behaves like a mirror) and created a data acquisition process similar to the fiber spectrometer studies in the literature.
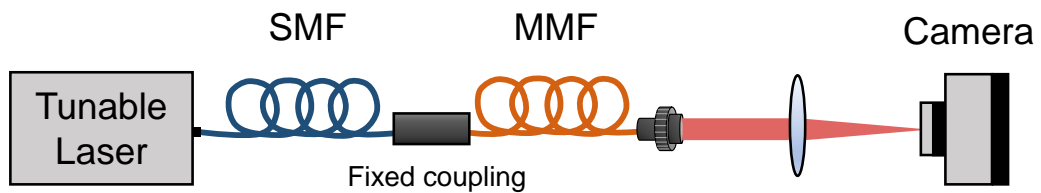
Figure 6.5: A simplified experimental setup for building a fiber spectrometer. The signal emitted from the tunable laser is coupled into a polarization-maintaining single-mode fiber, which is then sent through a multimode fiber (core diameter 105 μm, NA = 0.22) with a fixed coupling. Speckles generated at the distal end of the fiber are imaged onto an InGaAs camera.

With the aforementioned setup, we have constructed the calibration data by measuring the speckles of 201 wavelengths between 1550 nm and 1551 nm in steps of 5 pm. Normally, the spectrometer has to be tested after the calibration data is obtained. However, in our system, setting and stabilizing a single wavelength takes ∼30 seconds, and calibration of 201 wavelengths can be completed in around 100 minutes. Thus an extra 100 minutes is added between the calibration set and the test set although the calibration process would be much faster with the use of more capable tunable lasers or wavelength-swept lasers. As mentioned in [196], the standard tunable lasers

71
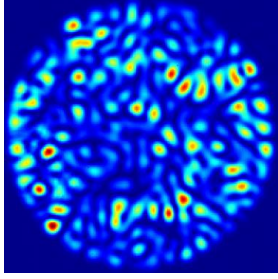
used in telecommunication have the ability to tune the wavelengths very rapidly, at about 0.1 ms - 1 s. In [188], a calibration time of around a few minutes is reported for 500 wavelengths, which also implies a tuning speed below 1 s (for a single wavelength). When the time spent for the calibration increases, the multimode fiber becomes more exposed to the environmental changes and vibrations, and hence the speckles start to decorrelate, as was previously shown in Fig. 3.2 in Chapter 3. This delay between the calibration and test set constructions increases the reconstruction error of the wavelengths. Thus it is a major obstacle in building a properly calibrated fiber spectrometer, which is specific to the equipment used in our setup. We handled this problem by speeding up the calibration process with the assumption that a standard tunable laser with 0.5 seconds tuning speed is implemented in the setup. With this assumption, the calibration of 201 wavelengths would be completed in $\sim$2 minutes. Therefore, it would be possible to test any wavelength 2 minutes after the calibration. For this purpose, instead of waiting for the whole calibration set to be completed, we captured the test set speckle of the wavelengths 2 minutes after the calibration speckles of the same wavelengths were captured.

6.4 Reconstruction Algorithm

The algorithm used to reconstruct the input wavelengths in the fiber spectrometer is very similar to the one introduced in Chapter 4. To construct a propagation equation, we first model the inputs and outputs as column vectors. If the system is calibrated with M wavelengths, then the inputs are vectors of length $M \times 1$. The input vectors are called spectrum vectors, and they are denoted by $\mathbf{S_i}$, where each $i = 1, 2, \ldots, M$ corresponds to a specific wavelength. The indices of the spectrum vectors (the positions of the elements inside the vector) represent the wavelengths, and the entries correspond to the signal weight (intensity) of the wavelengths in the total spectrum. Under these considerations, the calibration spectrum vectors are defined as standard unit vectors of M dimensional vector space, as shown below. This definition is reasonable since the laser power is set to a fixed value during the data acquisition process. Independent from the actual output power, the spectrum vectors can be considered as normalized vectors as long as all wavelengths are emitted with the same power.

$$
\mathbf{S_1} = \begin{bmatrix} 1 \\ 0 \\ 0 \\ \vdots \\ 0 \end{bmatrix}_{M \times 1} \qquad
\mathbf{S_2} = \begin{bmatrix} 0 \\ 1 \\ 0 \\ \vdots \\ 0 \end{bmatrix}_{M \times 1} \qquad
\mathbf{S_3} = \begin{bmatrix} 0 \\ 0 \\ 1 \\ \vdots \\ 0 \end{bmatrix}_{M \times 1} \qquad \bullet\bullet\bullet \qquad
\mathbf{S_M} = \begin{bmatrix} 0 \\ 0 \\ 0 \\ \vdots \\ 1 \end{bmatrix}_{M \times 1}
$$

The outputs, speckle patterns measured by the camera, have two-dimensional structures and are originally represented by 2D matrices. We reshape the speckle matrices into column vectors $\mathbf{I_i}$ (called intensity vectors), where $i = 1, 2, \ldots, M$ specifies the input wavelength created the speckle. If the speckle has a resolution of $m \times n$, then the original speckle matrices will have $m \times n$ dimensions, and the intensity vectors will have $(m \times n) \times 1$ dimensions.

$$
\longrightarrow \begin{bmatrix}
11 & 15 & 12 & \ldots & 10 \\
20 & 14 & 10 & \ldots & 13 \\
10 & 16 & 15 & \ldots & 12 \\
\vdots & \vdots & \vdots & \ddots & \vdots \\
13 & 18 & 12 & \ldots & 11
\end{bmatrix}_{m \times n}
\xrightarrow{\text{reshape}}
\mathbf{I_i} = \begin{bmatrix} 11 \\ 15 \\ 12 \\ \vdots \\ 11 \end{bmatrix}_{(m \times n) \times 1}
$$

After modeling the inputs and outputs as column vectors, a propagation equation between the spectrum vectors and the intensity vectors can be written as

$$
\mathbf{I_i} = \mathbf{T} * \mathbf{S_i}, \tag{6.4}
$$

where $\mathbf{T}$ is a $(m \times n) \times M$ dimensional matrix known as calibration matrix (also called propagation matrix or transmission matrix), and "$*$" denotes the matrix multiplication. Since spectrum vectors are modeled as unit vectors in the standard basis of M-dimensional vector space, the propagation equation can only be satisfied if the columns of the calibration matrix are constructed from the intensity vectors. Below, we show the matrix form of the calibration matrix (on the left) and a visualization of the calibration matrix obtained in the experiment for 201 wavelengths (on the right).

$$T = \begin{bmatrix} | & | & & | \\ I_1 & I_2 & \cdots & I_M \\ | & | & & | \end{bmatrix}_{(m \times n) \times M} \longrightarrow$$
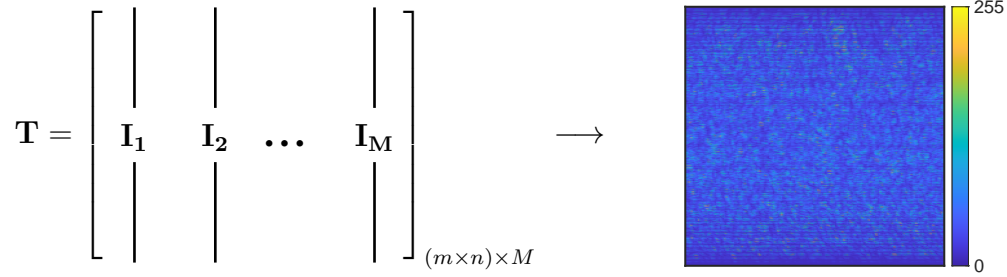
When the speckles of all M wavelengths are captured, the calibration matrix $\mathbf{T}$ can easily be constructed as described above. The calibration matrix can then be used to reconstruct any unknown input spectrum consisting of combinations of calibrated wavelengths. In practice, the user will have the intensity vector, $\mathbf{I_u}$, created by the unknown input spectrum, together with the calibration matrix $\mathbf{T}$. In this case, the unknown spectrum vector, $\mathbf{S_u}$, can be obtained by inverting the propagation equation, Eq. (6.4),

$$\mathbf{S_u} = \mathbf{T^{-1}} * \mathbf{I_u}. \tag{6.5}$$

Once the spectrum vector is obtained, it can be plotted to obtain the reconstructed spectrum. In Fig. 6.6, we show an example of the reconstruction procedure for an input spectrum $\mathbf{S_u^{probe}} = 0.3\,\mathbf{S_{40}} + 0.7\,\mathbf{S_{160}}$, which is a combination of two wavelengths in the calibration set with different signal weights. Since the optical signals of different frequencies do not interfere [188], the intensity vector of the unknown spectrum can be obtained by the weighted sum of the speckles corresponding to the same combination as the unknown spectrum vector, $\mathbf{I_u} = 0.3\,\mathbf{I_{40}} + 0.7\,\mathbf{I_{160}}$. By using the measured speckle, $\mathbf{I_u}$, and the calibration matrix $\mathbf{T}$, the unknown spectrum can be reconstructed with slight deviations from the actual probe spectrum.
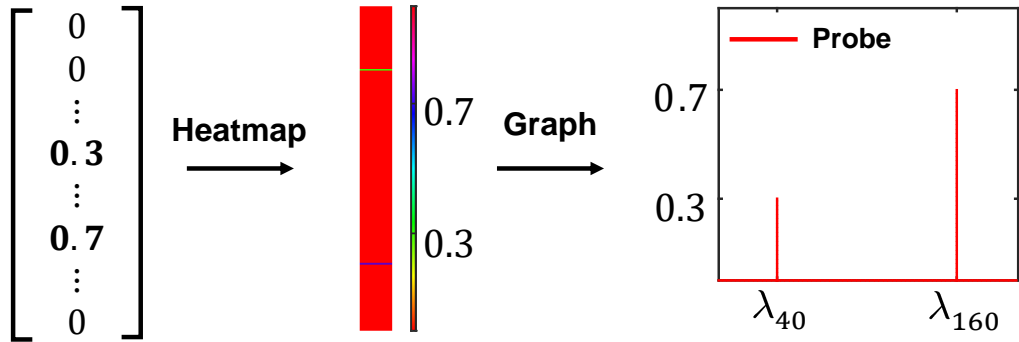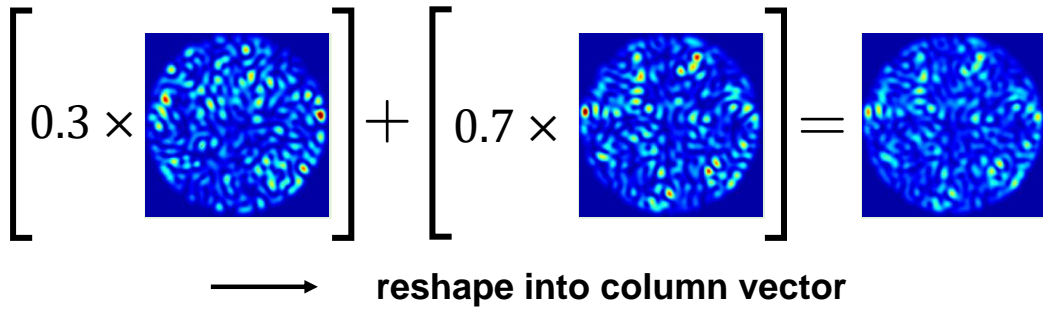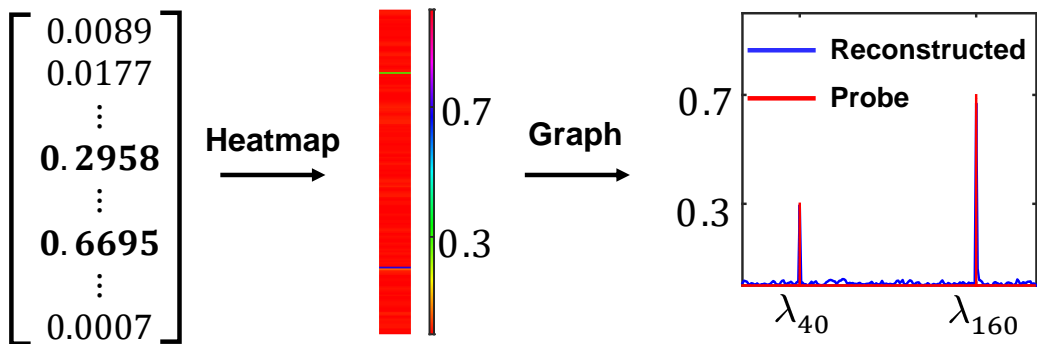
Figure 6.6: An example of the reconstruction procedure in fiber spectrometer. **(a)** The input spectrum consists of two wavelengths with different weights and is represented by a column vector. **(b)** The measured speckle (which is the sum of the individual speckles created by the wavelengths in the spectrum) is also converted into a column vector. **(c)** The input spectrum is reconstructed by using the measured speckle and the calibrated data.

6.5 Results

After the calibration of the system is completed and a calibration matrix $\mathbf{T}$ is obtained, the spectrometer can be tested with different light sources whose spectral content is within the range of the calibrated wavelengths. In order to test the performance of the fiber spectrometer, we have used the following three input spectra:

1. Single wavelength produced by a monochromatic light source

2. Discrete line spectra produced by an atomic gas

3. Broadband continuous spectra produced by a supercontinuum light source

For all cases, the intensity vector $\mathbf{I_u}$ is obtained, and the inverse propagation equation is used to reconstruct the input spectra. To measure the accuracy of the spectrometer, the root-mean-square error (RMSE),

$$\mu = \sqrt{\frac{1}{M}[\mathbf{S_u^{probe}} - \mathbf{S_u^{reconstructed}}]^2} \ , \tag{6.6}$$

between the actual probe spectrum $\mathbf{S_u^{probe}}$ and the reconstructed spectrum $\mathbf{S_u^{reconstructed}}$ is calculated, where M is the number of calibrated wavelengths, which is equal to the size of the spectrum vectors. The reconstruction results for the first case, the monochromatic spectra, are shown in Fig. 6.7(a). Here, each wavelength is reconstructed separately, and the results are plotted in a single graph. In this case, the average reconstruction error is around 3%. Fig. 6.7(b) shows the performance of the spectrometer in reconstructing a spectrum consisting of three discrete wavelengths with different weights. The error between the actual spectrum (dashed red line) and the reconstructed spectrum (solid blue curve) is ∼1.8%. Fig. 6.7(c) demonstrates the spectrometer's ability to reach the resolution value promised by the speckle correlation curves. The 10 pm resolution is approved as the system can successfully distinguish two discrete spectral lines with 10 pm separation. The reconstruction of broadband continuous spectra is shown in Fig. 6.7(d) for three sources having different bandwidths. In this case, the spectral reconstruction error increases from 3.8% to 8.7% as the bandwidth of the signal increases from 50 pm (covering 5% of the whole spectral range) to 200 pm (covering 20% of the whole spectral range).

76
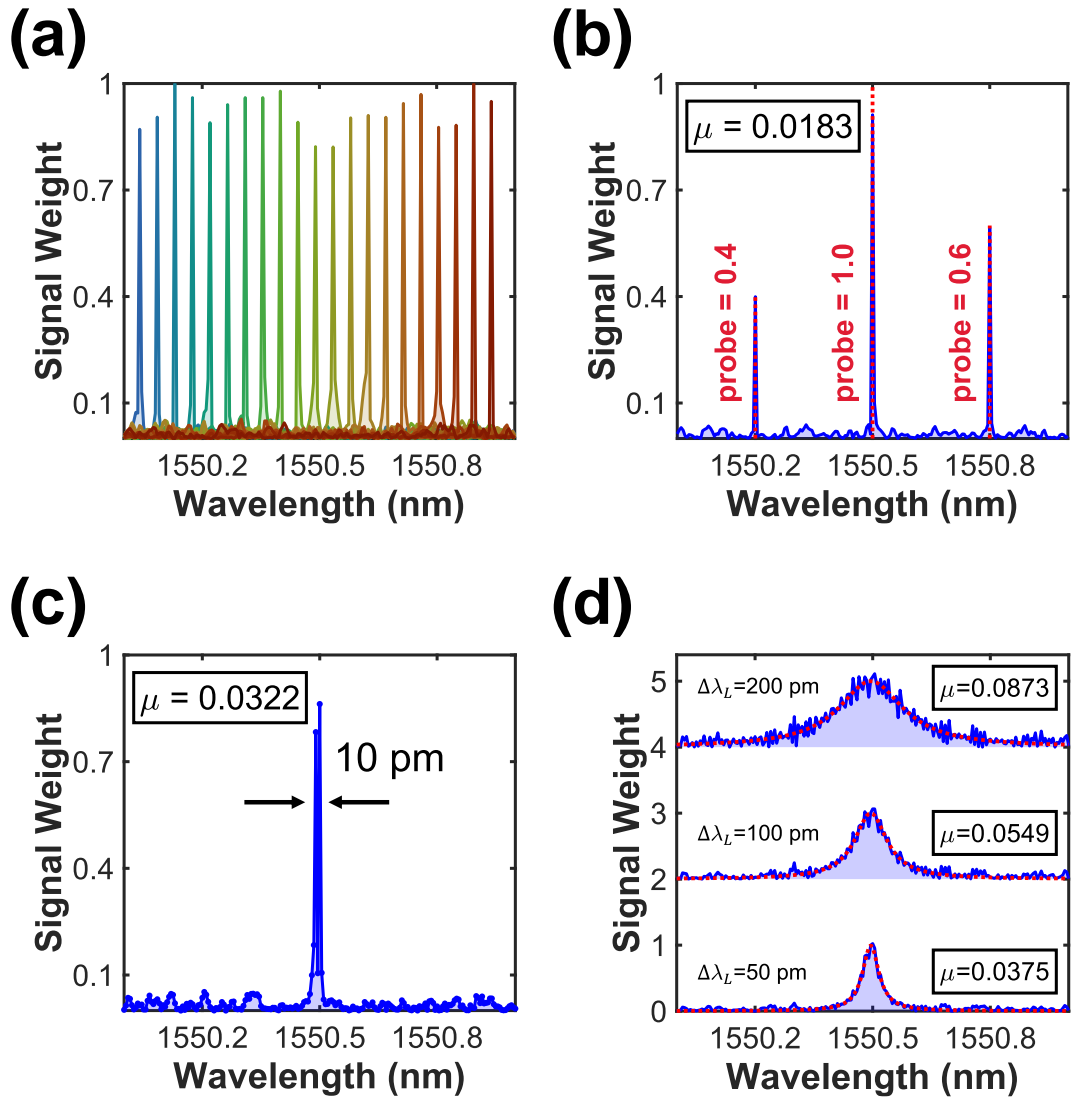
Figure 6.7: Reconstruction results for three different types of input spectra. **(a)** Monochromatic spectrum is reconstructed with an average error of ~3%. Each wavelength is reconstructed separately, and the results are shown in a single graph. **(b)** A spectrum involving three discrete lines with different weights is reconstructed with 1.8% error. The probe spectrum is shown with the dashed red line. **(c)** The resolution value suggested by the correlation curves is approved as the spectrometer is able to reconstruct two lines separated by 10 pm. **(d)** For an input source producing a continuous broadband spectrum, the error depends on the bandwidth of the signal. When the bandwidth of the signal covers 20% of the whole spectral range, the reconstruction error increases to ~9%.

CHAPTER 7

SINGLE-PIXEL MULTIMODE FIBER SPECTROMETER

The content presented in this chapter is adapted from the preprint version:

- S. Kürekci, S. S. Kahraman, and E. Yüce, "Single-Pixel Multimode Fiber Spectrometer via Wavefront Shaping," arXiv.2210.13292 [Preprint]

When light passes through a multimode fiber, two-dimensional random intensity patterns are formed due to the complex interference within the fiber. The extreme sensitivity of speckle patterns to the frequency of light paved the way for high-resolution multimode fiber spectrometers. However, this approach requires expensive IR cameras and impedes the integration of spectrometers on-chip. In this study, we propose a single-pixel multimode fiber spectrometer by exploiting wavefront shaping. The input light is structured with the help of a spatial light modulator, and optimal phase masks, focusing light at the distal end of the fiber, are stored for each wavelength. Variation of the intensity in the focused region is recorded by scanning all wavelengths under fixed optimal masks. Based on the intensity measurements, we show that an arbitrary input spectrum having two wavelengths 20 pm apart from each other can be reconstructed successfully (with a reconstruction error of ~3%) in the near-infrared regime, corresponding to a resolving power of $R \approx 10^5$. We also demonstrate the reconstruction of broadband continuous spectra for various bandwidths. With the installation of a single-pixel detector, our method provides low-budget and compact detection at an increased single-to-noise ratio.

7.1 Introduction

Spectrometers achieve spectral-to-spatial mapping, which allows spectral decomposition of the input light. Conventional spectrometers use dispersive media such as gratings or prisms, and they can achieve resolving powers around $R < 10^4$ and can reach up to $R < 10^5$ only with the installation of complex triple-grating systems (the spectral resolution is $\delta\lambda = \lambda_0/R$, where λ_0 is the operating wavelength). However, such spectrometers generally require moving parts (grating, mirrors) and a line array detector for scanning whole wavelengths of interest. Moreover, inverse proportionality between spectral resolution and optical path length leads to bulky systems when high resolution is demanded. The fundamental need for high-resolution spectral analysis in various lines of research and applications triggers new concepts that are built on the basis of holography [197], scattering of light by a photonic crystal [189, 198] a random scattering medium [199] or a multimode fiber (MMF) [188, 190, 192, 200] to form a complex spatial intensity distribution (a speckle pattern) on a multipixel detector such as a charged couple device (CCD) or a focal plane array (FPA). In such systems, wavelengths experience different propagation constants inside the scattering medium, thus forming distinct spatial intensity profiles on the detector, which provides the required one-to-one spectral-to-spatial mapping. Before the use of the spectrometer, a calibration matrix is measured by scanning all wavelengths in the operational range, and it stores the corresponding speckle patterns. The calibration matrix is then utilized to reconstruct an arbitrary input spectrum based on the measured intensity distribution. However, the increased cost of CCD and FPA sensors, especially in the infrared regime, limits the deployment of high-resolution spectral analysis tools.

Among all scattering-based systems, the multimode fiber spectrometers have been particularly attractive by offering high resolutions with reduced scattering losses (keeping the light collimated inside the fiber and preventing scattering to higher angles). Since fibers can be wrapped, higher spectral resolution can be achieved without enlarging the system. It was shown in [190] that high resolving powers $R > 10^6$ in near-infrared regime is possible with fibers of 100 m long. Yet the signal-to-noise ratio (SNR) is the main limiting factor for the resolution at low signal levels, and increased fiber length [184].

Single pixel detection together with compressed sensing [201–203] have been revolutionizing imaging methods. Surprisingly, the penetration of these methods in spectroscopy has been very limited due to mechanical resolution limits. The single-pixel imaging (SPI) systems are based on the use of a spatial light modulator (SLM) and a single-pixel detector. Employing the SPI method is particularly useful when working in the infrared regime since FPAs get extremely expensive at longer wavelengths [204].

In this study, we develop a high-resolution single-pixel multimode fiber spectrometer and demonstrate its ability to reconstruct arbitrary spectra. The single-pixel detection is achieved by focusing light on a selected target region of a focal plane array which is employed as a bucket detector. The input wavefronts are structured using a spatial light modulator which provides distinct output intensities at the detector [15, 38, 126, 205, 206]. The intensity variations at the target position as a function of input wavelength are used to reconstruct the spectra at a resolution of 20 pm. The increased intensity at the focused point also increases SNR, which removes low signal barrier in reaching high resolutions at low signal levels. This, to the best of our knowledge, is the first demonstration of a high-resolution scattering medium-based spectrometer exploiting single-pixel detection. Replacing an FPA with a single-pixel detector reduces the cost in infrared applications enormously, and it also provides a new method for on-chip hyperspectral compressed imaging, which is brought by the compact size of a single-pixel spectrometer.

7.2 Methods

The spectrometer is built based on the system given in Fig. 7.1. A tunable laser operating around 1550 nm with 38 nm tuning range is used for illuminating an SLM (HOLOEYE PLUTO-TELCO) with 1920×1080 pixels screen resolution. The beam is expanded to cover the SLM screen, and a half-wave plate is used to control the incident polarization so that it matches the alignment direction of the liquid crystals inside the SLM.

The light is phase-modulated via SLM and focused on the distal end of a 20-meter-long multimode fiber (core diameter 105 μm, NA = 0.22). A continuous sequential

algorithm [123] is used in the modulation steps where the SLM is divided into 144 superpixels of size 16×9 and four phase steps between 0-2π are scanned through each superpixel. The modulated beam is focused into a circular target region consisting of 76 pixels on a bucket detector of 30 μm×30 μm cell size. The intensity at the focus spot is then integrated to reconstruct the input spectrum from single-pixel data. Since the whole spectrometer is built upon the intensity measurements of the target region, which effectively covers an area around 0.07 mm^2, the bucket detector can safely be replaced with commercial photodiodes, which generally have active areas larger than the size of our target region [207].
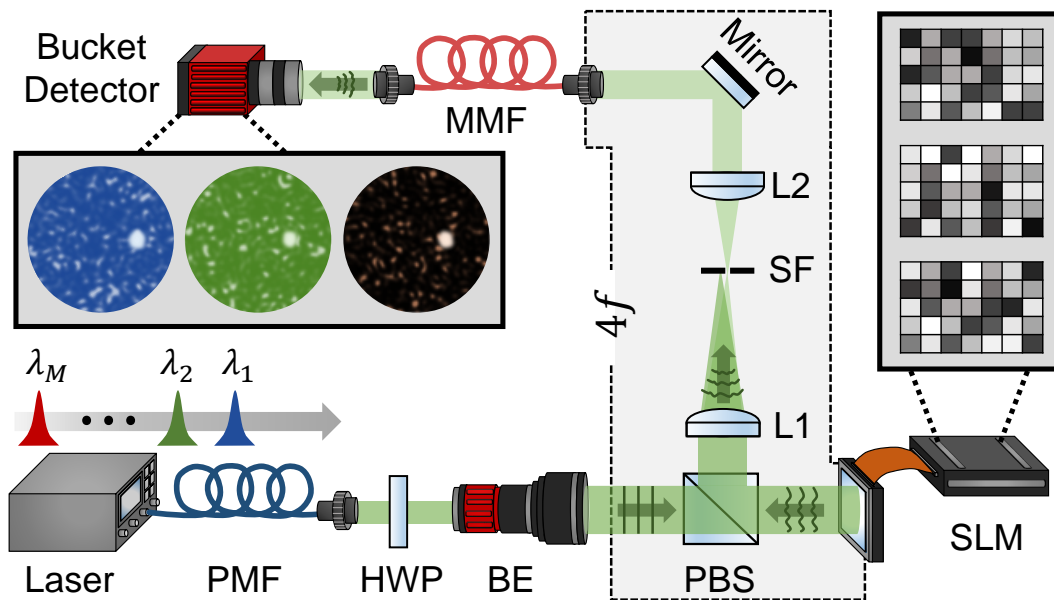
Figure 7.1: Schematic of the setup. The input wavelengths provided by a tunable laser are optimized at the end of a 20-meter-long multimode fiber by using a spatial light modulator. Unique SLM patterns are used to focus distinct wavelengths. L: Lens, PMF: Polarization Maintaining Fiber, HWP: Half-Wave Plate, BE: Beam Expander, PBS: Polarizing Beam Splitter, SLM: Spatial Light Modulator, SF: Spatial Filter, MMF: Multimode Fiber.

In order to calibrate the spectrometer, we have modified the calibration process in [188] for an SLM-based single-pixel system as depicted in Fig. 7.2. We represent the

input spectrum of a single wavelength λ_i as a unit vector,

$$\mathbf{S_i} = [\lambda_1 \quad \lambda_2 \quad \ldots \quad \lambda_M]^T, \tag{7.1}$$

where all the elements except $\lambda_i = 1$ are set to zero (T is the transpose operator). All M input wavelengths within the scope of the operating range of the spectrometer are modulated by the SLM and optimized on the target region of the detector. The optimized SLM phase masks, ϕ_i ($i = 1, 2, \ldots, M$) are stored. Once the optimization process is completed, the target region intensities of individual wavelengths are measured under all recorded SLM patterns, and the intensity values are then integrated into a single numerical value. Throughout the text, $I_{\lambda_i}^{\phi_j}$ denotes the integrated intensity of the target region under input wavelength λ_i and optimized SLM pattern ϕ_j. For each wavelength, λ_i (or spectrum vector $\mathbf{S_i}$), a corresponding intensity vector as a function of SLM phase mask ϕ is created,

$$\mathbf{I_i} = [I_{\lambda_i}^{\phi_1} \quad I_{\lambda_i}^{\phi_2} \quad \ldots \quad I_{\lambda_i}^{\phi_M}]^T. \tag{7.2}$$

The intensity vectors are then combined into a single $M \times M$ matrix $\mathbf{T}$, which is called the calibration matrix, whose rows can be used as a measure of the system response to wavelength variations. With the implementation of advanced wavefront optimization methods, it is possible to focus light in milliseconds [208] and complete the calibration of the spectrometer in less than a few minutes for many practical spectroscopy applications.

The entries sitting in the main diagonal of the calibration matrix are expected to have the highest numerical values in their row and column since they correspond to the perfect match between the input wavelength and the optimized SLM pattern. In the off-diagonal entries, wavelength and the optimized phase mask mismatch, and as a result, the integrated intensity drops for steps out of the diagonal. More contrast between the diagonal and off-diagonal entries can be produced when the light is sharply focused on the detector. In this case, the spectrometer is expected to be more sensitive to wavelength variations, and thus have a higher resolution. The sharpness of the focus can be controlled by involving a measure of merit (such as enhancement factor) during the optimization. In our experiments, we measured an average enhancement around $\eta \approx 70$, which is approximately 40% below the theoretical maximum value [206].
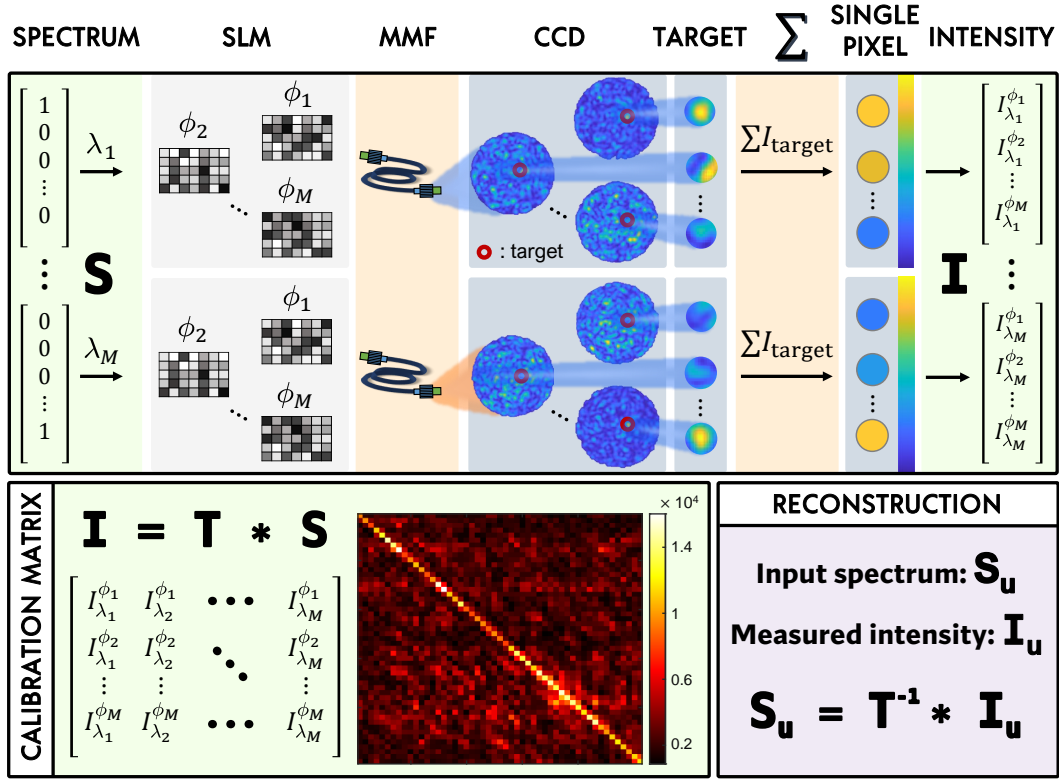
Figure 7.2: Schematic explanation of calibration and reconstruction. The upper rectangle illustrates the process used to obtain the calibration matrix $\mathbf{T}$. The heatmap of the 50×50 calibration matrix obtained in the experiment is shown inside the bottom left rectangle. Using the inverse of the calibration matrix, an unknown input spectrum can be reconstructed as formulated in the bottom right corner. The asterisk operator (*) denotes matrix multiplication.

The calibration process of the spectrometer can be modeled mathematically as a set of linear propagations where the inputs are the spectrum vectors $\mathbf{S_i}$, outputs are the intensity vectors $\mathbf{I_i}$, and the propagation operator is the calibration matrix $\mathbf{T}$,

$$\mathbf{T} * \mathbf{S_i} = \mathbf{I_i}. \tag{7.3}$$

To test the performance of the spectrometer, an unknown spectrum $\mathbf{S_u^{probe}}$ is sent through the system and the corresponding intensity vector $\mathbf{I_u}$ is captured. By inverting Eq. (7.3), we obtain the reconstructed spectrum vector $\mathbf{S_u^{reconstructed}}$ based on the calibration data and the measured intensity,

$$\mathbf{S_u^{reconstructed}} = \mathbf{T^{-1}} * \mathbf{I_u}. \tag{7.4}$$

The performance of the spectrometer is measured by comparing the reconstructed spectrum to the actual probe spectrum, where the comparison is done by calculating the root mean square error,

$$\mu = \sqrt{\frac{1}{M}[\mathbf{S_{probe}} - \mathbf{S_{reconstructed}}]^2} \tag{7.5}$$

7.3 Results

Using the calibration process explained in Fig. 7.2, we have calibrated our system with 50 wavelengths around the central wavelength 1550 nm (from 1549.75 nm to 1550.24 nm) with 10 pm step-size between consecutive wavelengths. After the calibration matrix is obtained and stored, individual wavelengths are sent through the system and measured intensities are plugged in Eq. (7.4). The reconstructed spectrum vectors of individual wavelengths in the spectral range are plotted in Fig. 7.3(a). Since optical signals of different wavelengths do not interfere, an arbitrary spectrum can be modeled with a tunable laser by creating the spectrum content separately and then superposing the measured intensities. In the mathematical formulation, we sum the individual intensity vectors and plug the resulting vector in Eq. (7.4) as the measured intensity. For two wavelengths 20 pm apart from each other, the spectrum reconstruction is shown in Fig. 7.3(b). We show that a single pixel spectrometer can resolve the spectral lines accurately and is able to reconstruct the unknown input spectrum with a reconstruction error $\mu = 0.0298$.

While the input light entering the system may consist of sparse wavelengths, it may also carry a broadband spectrum. In this case, we model the continuous broadband spectrum as a weighted combination of individual wavelengths. We discretize the broadband spectrum with 10 pm spacing, which is the step size between two consecutive wavelengths in our dataset. To test the performance of the spectrometer, we modeled broadband Lorentzian beams of different bandwidths in the 490 pm spectral range from 1549.75 nm to 1550.24 nm. Each wavelength involved in the broadband signal is expected to contribute to the final intensity by its weight in the spectrum. Thus, the final intensity measured on the detector is found by superposing the individual intensity vectors scaled by the weight of the corresponding wavelength. Then, the

resulting intensity vector is inserted in Eq. (7.4) to predict the input spectrum. The results for three Lorentzian beams centered at 1549.99 nm with 20 pm, 100 pm, and 200 pm bandwidths corresponding to $\sim$4%, $\sim$20% and $\sim$40% of the total spectral range are plotted in Figure 7.3(c). It is observed that the reconstruction error increases with the bandwidth of the signal, reaching $\sim$6% ($\mu = 0.0569$) when $\sim$40% of the spectral range is covered.
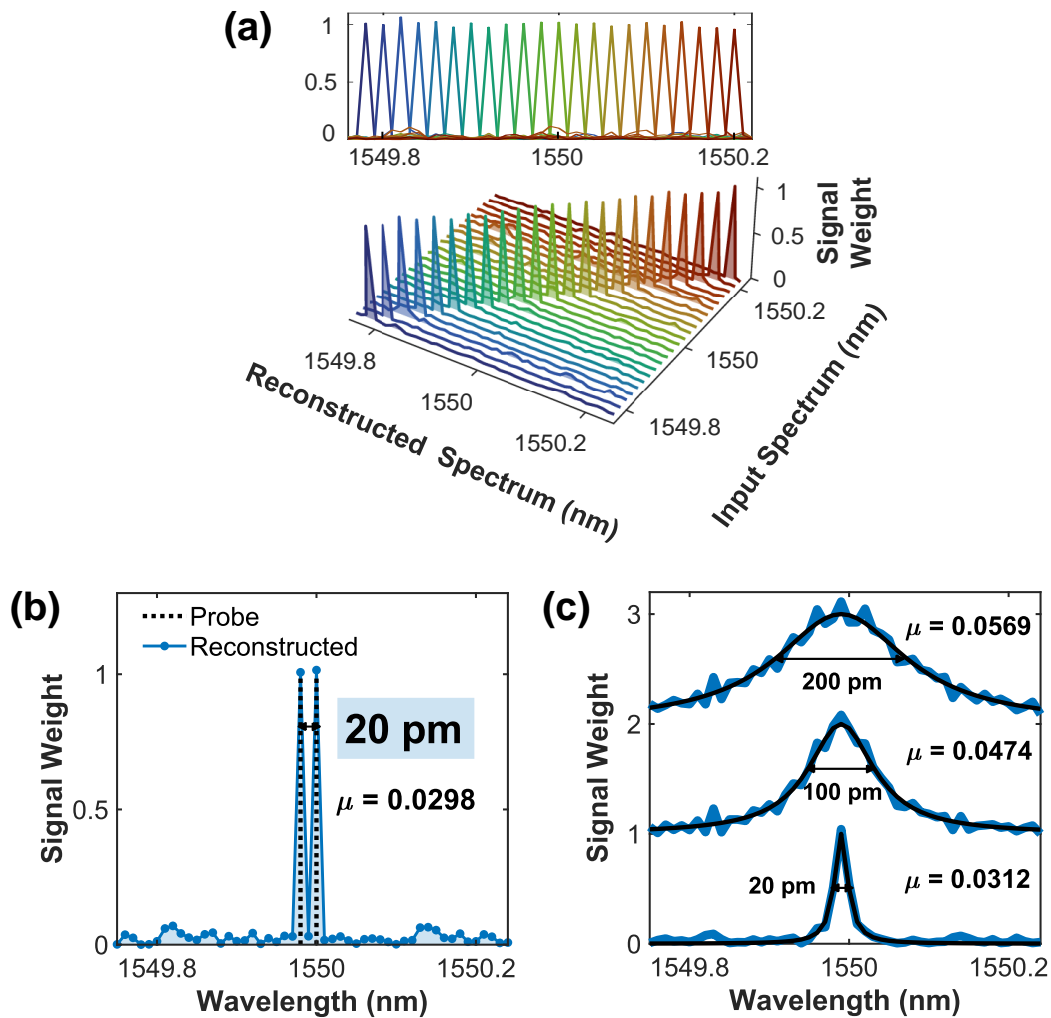
Figure 7.3: Performance of spectrometer in reconstructing (a) individual wavelengths, (b) arbitrary spectra with two wavelengths, and (c) broadband Lorentzian spectra of various bandwidths.

7.4 Discussion

It is possible to reduce the spectrum reconstruction error of a multimode fiber-based speckle spectrometer by suppressing the system noise using computational methods such as truncated inversion [188, 209]. In this study, we show pure physical results solely based on intensity measurements without any computational aid. The computational manipulations should be handled carefully in a single-pixel spectrometer since 1) the number of data points is fewer compared to a speckle spectrometer which may immediately dismiss some methods, and 2) diagonal data is positively biased in the calibration matrix of the single-pixel spectrometer opposite to the speckle spectrometer where the data is randomly distributed due to the nature of speckle images. A computational method preserving the diagonality of the calibration matrix and simultaneously respecting the correlation between the columns of $\mathbf{T}$ may be a good candidate for reducing the errors. Increasing the isolation of the system by stabilizing the multimode fiber is another way of suppressing the system noise [192]. In preferred cases, the isolation can be provided by replacing the multimode fiber with an integrated ridge waveguide which is much less susceptible to environmental variations. With such improvements, we believe the single-pixel spectrometer will be able to go beyond the resolution limit of a speckle spectrometer which is more affected by the detection noise [184].

7.5 Conclusion

In summary, we have demonstrated a high-resolution, single-pixel multimode fiber spectrometer employing wavefront shaping of light. The working principle of the spectrometer is based on the abrupt distortion of the focused intensity when the wavelength of the incoming light changes. Thus, the use of the SLM is not required for our method. The system can be externally perturbed by heat or carrier injection to a semiconductor waveguide. The calibration can be performed with respect to the external perturbation, and an arbitrary spectrum can be reconstructed accordingly. The SLM, on the other hand, brings an additional advantage by increasing the signal-to-noise level. The efforts regarding the miniaturized wavefront controllers can pave the

way for simultaneous spectral reconstruction as well as increasing the SNR [210, 211]. The proposed spectrometer is promising in developing single-pixel hyperspectral imaging applications across scattering media, and it offers replacing bulky, expensive cameras with a single-pixel detector to develop low-budget systems.

CHAPTER 8

CONCLUSION

In this thesis, the classification and reconstruction of spatial and spectral information across multimode fibers are studied. Scrambling of input information into speckle patterns (random intensity distributions) during the propagation of electromagnetic waves in multimode fibers is discussed. The wavefront shaping method and the spatial light modulators (SLM) are introduced, and two feedback-based wavefront shaping algorithms are developed for focusing light at the distal end of the multimode fiber. The use of spatial light modulators and fibers in safe optical communication and in cryptography is investigated. For this purpose, binary numbers between 1 and 9 are encoded as optical gratings on the spatial light modulator, and light reflected from the SLM is propagated through a multimode fiber. The input numbers are reconstructed from the corresponding speckle patterns by solving the inverse propagation equation algebraically. The long-term performance of this communication system is tested without the use of high-level isolation precautions, yet accurate classification of the numbers is achieved for 30 hours. The classification task over multimode fibers is expanded to include images of handwritten letters, and a deep-learning algorithm is developed for this objective. The images are written on the SLM screen, and output speckles obtained at the end of the multimode fiber are stored. Three different neural networks, Res-Net, U-Net, and VGG-Net, are trained with the input-output couples, and their performance is tested. A high reconstruction accuracy of around 90% is achieved, and the superiority of Res-Net architecture in terms of accuracy is shown. The classification and reconstruction task is further enlarged to cover the spectral signals, and a high-resolution, compact, low-cost multimode fiber spectrometer is demonstrated. A calibration matrix is constructed from the speckles obtained for the wavelengths in the spectral range of interest, and this matrix is then used to recon-

struct input spectra with high resolving powers ($R \geq 10^5$). The performance of the spectrometer is tested for three cases, including monochromatic spectra, arbitrary discrete spectra, and continuous spectra, and the unknown input spectrum is successfully reconstructed in all cases with low errors. To decrease the size of the system on the detection side, a single-pixel multimode fiber spectrometer is developed. All wavelengths in the spectral range are focused on a chosen target region at the distal end of the multimode fiber, and the spectrometer is built based on the measurements of the integrated intensity of the target region. This spectrometer is also tested for the aforementioned three cases, and unknown input spectra are reconstructed with a resolving power of $R \approx 10^5$.

We believe the studies presented in this thesis can be developed further to build high-level fiber optic systems in telecommunication, biomedicine, and spectroscopy. The methods we introduced here may also inspire new applications in quantum optics and in cryptography.

REFERENCES

[1] J. Jönsson, *Multi-Scattering: Computational light transport in turbid media*. PhD thesis, Lund University, 2021.

[2] F. Zernike, "Phase contrast, a new method for the microscopic observation of transparent objects," *Physica*, vol. 9, no. 7, pp. 686–698, 1942.

[3] A. Ishimaru, *Wave Propagation and Scattering in Random Media*. Wiley, 1999.

[4] G. Popescu, *Quantitative Phase Imaging of Cells and Tissues*. McGraw-Hill Professional, 2011.

[5] K. Lee, K. Kim, J. Jung, J. Heo, S. Cho, S. Lee, G. Chang, Y. Jo, H. Park, and Y. Park, "Quantitative phase imaging techniques for the study of cell pathophysiology: From principles to applications," *Sensors*, vol. 13, no. 4, pp. 4170–4191, 2013.

[6] J.-H. Park, Z. Yu, K. Lee, P. Lai, and Y. Park, "Perspective: Wavefront shaping techniques for controlling multiple light scattering in biological tissues: Toward in vivo applications," *APL Photonics*, vol. 3, no. 10, p. 100901, 2018.

[7] E. N. Leith and J. Upatnieks, "Holographic imagery through diffusing media," *J. Opt. Soc. Am.*, vol. 56, pp. 523–523, Apr 1966.

[8] I. Freund, "Looking through walls and around corners," *Physica A: Statistical Mechanics and Its Applications*, vol. 168, no. 1, pp. 49–65, 1990.

[9] D. Huang, E. A. Swanson, C. P. Lin, J. S. Schuman, W. G. Stinson, W. Chang, M. R. Hee, T. Flotte, K. Gregory, C. A. Puliafito, and J. G. Fujimoto, "Optical coherence tomography," *Science*, vol. 254, no. 5035, pp. 1178–1181, 1991.

[10] O. Legrand, *Waves and Imaging through Complex Media*. Springer, 1st ed., 2001.

[11] J. Huisken, J. Swoger, F. D. Bene, J. Wittbrodt, and E. H. K. Stelzer, "Optical sectioning deep inside live embryos by selective plane illumination microscopy," *Science*, vol. 305, no. 5686, pp. 1007–1009, 2004.

[12] K. Svoboda and R. Yasuda, "Principles of two-photon excitation microscopy and its applications to neuroscience," *Neuron*, vol. 50, no. 6, pp. 823–839, 2006.

[13] K. Maslov, H. F. Zhang, S. Hu, and L. V. Wang, "Optical-resolution photoacoustic microscopy for in vivo imaging of single capillaries," *Opt. Lett.*, vol. 33, pp. 929–931, May 2008.

[14] T. Ccaron, I. Zcaron, Mar, M. Mazilu, and K. Dholakia, "In situ wavefront correction and its application to micromanipulation," *Nature Photonics*, vol. 4, pp. 388–394, 2010.

[15] A. P. Mosk, A. Lagendijk, G. Lerosey, and M. Fink, "Controlling waves in space and time for imaging and focusing in complex media," *Nature Photonics*, vol. 6, pp. 283–292, May 2012.

[16] M. Nixon, O. Katz, E. Small, Y. Bromberg, A. A. Friesem, Y. R. Silberberg, and N. Davidson, "Real-time wavefront shaping through scattering media by all-optical feedback," *Nature Photonics*, vol. 7, pp. 919–924, 2013.

[17] A. Bassi, B. Schmid, and J. Huisken, "Optical tomography complements light sheet microscopy for in toto imaging of zebrafish development," *Development*, vol. 142, pp. 1016–1020, Mar 2015.

[18] D. Kromm, T. Thumberger, and J. Wittbrodt, "Chapter 5 - an eye on light-sheet microscopy," in *The Zebrafish* (H. W. Detrich, M. Westerfield, and L. I. Zon, eds.), vol. 133 of *Methods in Cell Biology*, pp. 105–123, Academic Press, 2016.

[19] S. Rotter and S. Gigan, "Light fields in complex media: Mesoscopic scattering meets wave control," *Reviews of Modern Physics*, vol. 89, p. 015005, 2017.

[20] A. Escobet-Montalbán, F. M. Gasparoli, J. Nylk, P. Liu, Z. Yang, and K. Dholakia, "Three-photon light-sheet fluorescence microscopy," *Opt. Lett.*, vol. 43, pp. 5484–5487, Nov 2018.

[21] T.-L. Liu, S. Upadhyayula, D. E. Milkie, V. Singh, K. Wang, I. A. Swinburne, K. R. Mosaliganti, Z. M. Collins, T. W. Hiscock, J. Shea, A. Q. Kohrman, T. N. Medwig, D. Dambournet, R. Forster, B. Cunniff, Y. Ruan, H. Yashiro, S. Scholpp, E. M. Meyerowitz, D. Hockemeyer, D. G. Drubin, B. L. Martin, D. Q. Matus, M. Koyama, S. G. Megason, T. Kirchhausen, and E. Betzig, "Observing the cell in its native state: Imaging subcellular dynamics in multicellular organisms," *Science*, vol. 360, no. 6386, p. eaaq1392, 2018.

[22] X. Yuan and S. Han, "Single-pixel neutron imaging with artificial intelligence: Breaking the barrier in multi-parameter imaging, sensitivity, and spatial resolution," *The Innovation*, vol. 2, 2021.

[23] C. M. Hobson, M. Guo, H. D. Vishwasrao, Y. Wu, H. Shroff, and T.-L. Chew, "Practical considerations for quantitative light sheet fluorescence microscopy," *Nature Methods*, vol. 19, pp. 1538–1549, 2022.

[24] H.-M. Cao, A. P. Mosk, and S. Rotter, "Shaping the propagation of light in complex media," *Nature Physics*, 2022.

[25] I. M. Vellekoop and A. P. Mosk, "Focusing coherent light through opaque strongly scattering media," *Opt. Lett.*, vol. 32, pp. 2309–2311, Aug 2007.

[26] Z. Yaqoob, D. Psaltis, M. S. Feld, and C. Yang, "Optical phase conjugation for turbidity suppression in biological samples," *Nature Photonics*, vol. 2, pp. 110–115, 2008.

[27] I. M. Vellekoop, A. Lagendijk, and A. Mosk, "Exploiting disorder for perfect focusing," *Nature Photonics*, vol. 4, no. 5, pp. 320–322, 2010.

[28] S. M. Popoff, G. Lerosey, R. Carminati, M. Fink, A. C. Boccara, and S. Gigan, "Measuring the transmission matrix in optics: An approach to the study and control of light propagation in disordered media," *Phys. Rev. Lett.*, vol. 104, p. 100601, Mar 2010.

[29] Y. M. Wang, B. Judkewitz, C. A. DiMarzio, and C. Yang, "Deep-tissue focal fluorescence imaging with digitally time-reversed ultrasound-encoded light," *Nature Communications*, vol. 3, 2012.

[30] S. Bianchi and R. Di Leonardo, "A multi-mode fiber probe for holographic micromanipulation and microscopy," *Lab on a Chip*, vol. 12, no. 3, pp. 635–639, 2012.

[31] J.-H. Park, C. Park, H. Yu, Y.-H. Cho, and Y. Park, "Dynamic active wave plate using random nanoparticles," *Optics Express*, vol. 20, no. 15, pp. 17010–17016, 2012.

[32] J.-H. Park, C. Park, H. Yu, J. Park, S. Han, J. Shin, S. H. Ko, K. T. Nam, Y.-H. Cho, and Y. Park, "Subwavelength light focusing using random nanoparticles," *Nature Photonics*, vol. 7, no. 6, pp. 454–458, 2013.

[33] P. Lai, L. Wang, J. W. Tay, and L. V. Wang, "Photoacoustically guided wavefront shaping for enhanced optical focusing in scattering media," *Nature Photonics*, vol. 9, pp. 126–132, 2014.

[34] S. R. Huisman, T. J. Huisman, S. A. Goorden, A. P. Mosk, and P. W. Pinkse, "Programming balanced optical beam splitters in white paint," *Optics Express*, vol. 22, no. 7, pp. 8320–8332, 2014.

[35] O. Katz, E. Small, Y. Guan, and Y. Silberberg, "Noninvasive nonlinear focusing and imaging through strongly scattering turbid layers," *Optica*, vol. 1, pp. 170–174, Sep 2014.

[36] J. Yoon, K. Lee, J. Park, and Y. Park, "Measuring optical transmission matrices by wavefront shaping," *Opt. Express*, vol. 23, pp. 10158–10167, Apr 2015.

[37] D. B. Conkey, A. M. Caravaca-Aguirre, J. D. Dove, H. Ju, T. W. Murray, and R. Piestun, "Super-resolution photoacoustic imaging through a scattering wall," *Nature Communications*, vol. 6, no. 1, pp. 1–7, 2015.

[38] R. Horstmeyer, H. Ruan, and C. Yang, "Guidestar-assisted wavefront-shaping methods for focusing light into biological tissue," *Nature Photonics*, vol. 9, pp. 563–571, Aug 2015.

[39] K. Lee, J. Lee, J.-H. Park, J.-H. Park, and Y. Park, "One-wave optical phase conjugation mirror by actively coupling arbitrary light fields into a single-mode reflector," *Phys. Rev. Lett.*, vol. 115, p. 153902, Oct 2015.

[40] H. Defienne, M. Barbieri, I. A. Walmsley, B. J. Smith, and S. Gigan, "Two-photon quantum walk in a multimode fiber," *Science Advances*, vol. 2, no. 1, p. e1501054, 2016.

[41] Z. Yu, H. Li, and P. Lai, "Wavefront shaping and its application to enhance photoacoustic imaging," *Applied Sciences*, vol. 7, no. 12, 2017.

[42] O. Tzang, A. M. Caravaca-Aguirre, K. Wagner, and R. Piestun, "Adaptive wavefront shaping for controlling nonlinear multimode interactions in optical fibres," *Nature Photonics*, vol. 12, no. 6, pp. 368–374, 2018.

[43] I. T. Leite, S. Turtaev, X. Jiang, M. Šiler, A. Cuschieri, P. S. J. Russell, and T. Čižmár, "Three-dimensional holographic optical manipulation through a high-numerical-aperture soft-glass multimode fibre," *Nature Photonics*, vol. 12, no. 1, pp. 33–39, 2018.

[44] J.-H. Park, Z. Yu, K. Lee, P. Lai, and Y. Park, "Perspective: Wavefront shaping techniques for controlling multiple light scattering in biological tissues: Toward in vivo applications," *APL Photonics*, vol. 3, no. 10, p. 100901, 2018.

[45] W. Xiong, C. W. Hsu, Y. Bromberg, J. E. Antonio-Lopez, R. Amezcua Correa, and H. Cao, "Complete polarization control in multimode fibers with polarization and mode coupling," *Light: Science & Applications*, vol. 7, no. 1, pp. 1–10, 2018.

[46] M. W. Matthès, P. Del Hougne, J. De Rosny, G. Lerosey, and S. M. Popoff, "Optical complex media as universal reconfigurable linear operators," *Optica*, vol. 6, no. 4, pp. 465–472, 2019.

[47] N. Bender, H. Yılmaz, Y. Bromberg, and H. Cao, "Creating and controlling complex light," *APL Photonics*, vol. 4, no. 11, p. 110806, 2019.

[48] S. Leedumrongwatthanakun, L. Innocenti, H. Defienne, T. Juffmann, A. Ferraro, M. Paternostro, and S. Gigan, "Programmable linear quantum networks with a multimode fibre," *Nature Photonics*, vol. 14, no. 3, pp. 139–142, 2020.

[49] X. Wei, J. C. Jing, Y. Shen, and L. V. Wang, "Harnessing a multi-dimensional fibre laser using genetic wavefront shaping," *Light: Science & Applications*, vol. 9, no. 1, pp. 1–10, 2020.

[50] Z. Li, Z. Yu, H. Hui, H. Li, T. Zhong, H. Liu, and P. Lai, "Edge enhancement through scattering media enabled by optical wavefront shaping," *Photon. Res.*, vol. 8, pp. 954–962, Jun 2020.

[51] H. Lee, S. Yoon, P. Loohuis, J. H. Hong, S. Kang, and W. Choi, "High-throughput volumetric adaptive optical imaging using compressed time-reversal matrix," *Light: Science & Applications*, vol. 11, pp. 1–13, 2021.

[52] Y. Zhao, Q. He, S. Li, and J. Yang, "Gradient-assisted focusing light through scattering media," *Opt. Lett.*, vol. 46, pp. 1518–1521, Apr 2021.

[53] L. Liu, K. Ma, Y. Qu, Q. He, R. Shao, C. Chen, and J. Yang, "High-contrast light focusing through scattering media with multi-pixel encoding," *Applied Physics Express*, vol. 14, p. 092009, Aug 2021.

[54] Z. Cheng and L. V. Wang, "Focusing light into scattering media with ultrasound-induced field perturbation," *Light, Science & Applications*, vol. 10, 2021.

[55] B. Rudolf, Y. Du, S. Turtaev, I. T. Leite, and T. Čižmár, "Thermal stability of wavefront shaping using a DMD as a spatial light modulator," *Opt. Express*, vol. 29, pp. 41808–41818, Dec 2021.

[56] S. Gigan, O. Katz, H. B. de Aguiar, E. R. Andresen, A. Aubry, J. Bertolotti, E. Bossy, D. Bouchet, J. Brake, S. Brasselet, Y. Bromberg, H. Cao, T. Chaigne, Z. Cheng, W. Choi, T. Čižmár, M. Cui, V. R. Curtis, H. Defienne, M. Hofer, R. Horisaki, R. Horstmeyer, N. Ji, A. K. LaViolette, J. Mertz, C. Moser, A. P. Mosk, N. C. Pégard, R. Piestun, S. Popoff, D. B. Phillips, D. Psaltis, B. Rahmani, H. Rigneault, S. Rotter, L. Tian, I. M. Vellekoop, L. Waller, L. Wang, T. Weber, S. Xiao, C. Xu, A. Yamilov, C. Yang, and H. Yılmaz, "Roadmap on wavefront shaping and deep imaging in complex media," *Journal of Physics: Photonics*, vol. 4, p. 042501, Aug 2022.

[57] L. Devaud, B. Rauer, M. Kühmayer, J. Melchard, M. Mounaix, S. Rotter, and S. Gigan, "Temporal light control in complex media through the singular-value decomposition of the time-gated transmission matrix," *Physical Review A*, 2022.

[58] Z. Yu, H. Li, T. Zhong, J.-H. Park, S. Cheng, C. M. Woo, Q. Zhao, J. Yao, Y. Zhou, X. Huang, W. Pang, H.-S. Yoon, Y. Shen, H. Liu, Y. Zheng, Y. Park,

L. V. Wang, and P. Lai, "Wavefront shaping: A versatile tool to conquer multiple scattering in multidisciplinary fields," *The Innovation*, vol. 3, 2022.

[59] C. Jensen-McMullin, H. P. Lee, and E. R. Lyons, "Demonstration of trapping, motion control, sensing and fluorescence detection of polystyrene beads in a multi-fiber optical trap," *Opt. Express*, vol. 13, pp. 2634–2642, Apr 2005.

[60] Z. Liu, C. Guo, J. Yang, and L. Yuan, "Tapered fiber optical tweezers for microscopic particle trapping: fabrication and application," *Opt. Express*, vol. 14, pp. 12510–12516, Dec 2006.

[61] X. Zhao, N. Zhao, Y. Shi, H. Xin, and B. Li, "Optical fiber tweezers: A versatile tool for optical trapping and manipulation," *Micromachines*, vol. 11, no. 2, 2020.

[62] W. Shi, Q. Fang, X. Zhu, R. A. Norwood, and N. Peyghambarian, "Fiber lasers and their applications," *Appl. Opt.*, vol. 53, pp. 6554–6568, Oct 2014.

[63] S. Addanki, I. Amiri, and P. Yupapin, "Review of optical fibers-introduction and applications in fiber lasers," *Results in Physics*, vol. 10, pp. 743–750, 2018.

[64] W. Wang, B. Zhou, S. Xu, Z. Yang, and Q. Zhang, "Recent advances in soft optical glass fiber and fiber lasers," *Progress in Materials Science*, vol. 101, pp. 90–171, 2019.

[65] "Recent advances and applications of random lasers and random fiber lasers," *Progress in Quantum Electronics*, vol. 78, p. 100343, 2021.

[66] W. Ecke, I. Latka, R. Willsch, A. Reutlinger, and R. Graue, "Fibre optic sensor network for spacecraft health monitoring," *Measurement Science and Technology*, vol. 12, pp. 974–980, 2001.

[67] M. A. Zumberge, W. Hatfield, and F. K. Wyatt, "Measuring seafloor strain with an optical fiber interferometer," *Earth and Space Science*, vol. 5, no. 8, pp. 371–379, 2018.

[68] C. U. Kumari, D. Samiappan, K. R., and T. Sudhakar, "Fiber optic sensors in ocean observation: A comprehensive review," *Optik*, vol. 179, pp. 351–360, 2019.

97

[69] H. Gong, M. S. Kizil, Z. Chen, M. Amanzadeh, B. Yang, and S. M. Aminossadati, "Advances in fibre optic based geotechnical monitoring systems for underground excavations," *International Journal of Mining Science and Technology*, vol. 29, no. 2, pp. 229–238, 2019.

[70] R. H. Scott, S. Chikermane, M. Vidakovic, B. McKinley, T. Sun, P. Banerji, and K. T. Grattan, "Development of low cost packaged fibre optic sensors for use in reinforced concrete structures," *Measurement*, vol. 135, pp. 617–624, 2019.

[71] I. Chapalo, A. Theodosiou, K. Kalli, and O. Kotov, "Multimode fiber interferometer based on graded-index polymer cytop fiber," *J. Lightwave Technol.*, vol. 38, pp. 1439–1445, Mar 2020.

[72] C. Li, W. Yang, X. Yu, J. Fan, Y. Xiong, Y. Yang, and L. Li, "A knotted shape core cladding optical fiber interferometer for simultaneous measurement of displacement and temperature," *Photonics and Nanostructures - Fundamentals and Applications*, vol. 39, p. 100778, 2020.

[73] J. Villatoro, "Phase-shifted modal interferometers for high-accuracy optical fiber sensing," *Opt. Lett.*, vol. 45, pp. 21–24, Jan 2020.

[74] N. A. Olsson, "Lightwave systems with optical amplifiers," *Journal of Lightwave Technology*, vol. 7, pp. 1071–1082, 1989.

[75] H. J. R. Dutton, "Understanding optical communications," Prentice Hall, 1998.

[76] G. P. Agrawal, "Fiber-optic communication systems," Wiley, 2002.

[77] D. O. Caplan, "Laser communication transmitter and receiver design," *Journal of Optical and Fiber Communications Reports*, vol. 4, pp. 225–362, 2007.

[78] R.-J. Essiambre, G. Kramer, P. J. Winzer, G. J. Foschini, and B. Goebel, "Capacity limits of optical fiber networks," *Journal of Lightwave Technology*, vol. 28, no. 4, pp. 662–701, 2010.

[79] P. J. Winzer, D. T. Neilson, and A. R. Chraplyvy, "Fiber-optic transmission and networking: the previous 20 and the next 20 years," *Opt. Express*, vol. 26, pp. 24190–24239, Sep 2018.

[80] S. Kumar, S. Rathee, P. Arora, and D. Sharma, "A comprehensive review on fiber bragg grating and photodetector in optical communication networks," *Journal of Optical Communications*, vol. 43, no. 4, pp. 585–592, 2022.

[81] R. Correia, S. James, S.-W. Lee, S. P. Morgan, and S. Korposh, "Biomedical application of optical fibre sensors," *Journal of Optics*, vol. 20, 2017.

[82] A. Gharatape and A. Y. Khosroushahi, "Optical biomarker-based biosensors for cancer/infectious disease medical diagnoses," *Applied Immunohistochemistry & Molecular Morphology*, vol. 27, p. 278–286, 2017.

[83] A. G. Leal-Junior, C. A. Diaz, L. M. Avellar, M. J. Pontes, C. Marques, and A. Frizera, "Polymer optical fiber sensors in healthcare applications: A comprehensive review," *Sensors*, vol. 19, p. 3156, Jul 2019.

[84] J. Guo, C. Yang, Q. Dai, and L. Kong, "Soft and stretchable polymeric optical waveguide-based sensors for wearable and biomedical applications," *Sensors*, vol. 19, no. 17, 2019.

[85] J. Guo, B. Zhou, C. Yang, Q. Dai, and L. Kong, "Stretchable and temperature-sensitive polymer optical fibers for wearable health monitoring," *Advanced Functional Materials*, vol. 29, no. 33, p. 1902898, 2019.

[86] W. Talataisong, R. Ismaeel, M. Beresna, and G. Brambilla, "Suspended-core microstructured polymer optical fibers and potential applications in sensing," *Sensors*, vol. 19, no. 16, 2019.

[87] S. E. Mowbray and A. M. Amiri, "A brief overview of medical fiber optic biosensors and techniques in the modification for enhanced sensing ability," *Diagnostics*, vol. 9, no. 1, 2019.

[88] P. Roriz, S. Silva, O. Frazão, and S. Novais, "Optical fiber temperature sensors and their biomedical applications," *Sensors*, vol. 20, no. 7, 2020.

[89] M. Loyez, E. M. Hassan, M. Lobry, F. Liu, C. Caucheteur, R. Wattiez, M. C. DeRosa, W. G. Willmore, and J. Albert, "Rapid detection of circulating breast cancer cells using a multiresonant optical fiber aptasensor with plasmonic amplification," *ACS Sensors*, vol. 5, no. 2, pp. 454–463, 2020.

[90] Y. Zhang, Y. Cao, and J.-X. Cheng, "High-resolution photoacoustic endoscope through beam self-cleaning in a graded index fiber," *Opt. Lett.*, vol. 44, pp. 3841–3844, Aug 2019.

[91] O. Herman, O. Wagner, N. Shabairou, and Z. Zalevsky, "Time multiplexed super resolution of multicore fiber endoscope using multimode fiber illumination patterns," *Optical Fiber Technology*, vol. 54, p. 102122, 2020.

[92] N. Stasio, C. Moser, and D. Psaltis, "Calibration-free imaging through a multicore fiber using speckle scanning microscopy," *Opt. Lett.*, vol. 41, pp. 3078–3081, Jul 2016.

[93] Y. Choi, C. Yoon, M. Kim, T. D. Yang, C. Fang-Yen, R. R. Dasari, K. J. Lee, and W. Choi, "Scanner-free and wide-field endoscopic imaging by using a single multimode optical fiber.," *Physical Review Letters*, vol. 109 20, p. 203901, 2012.

[94] A. M. Caravaca-Aguirre and R. Piestun, "Single multimode fiber endoscope," *Opt. Express*, vol. 25, pp. 1656–1665, Feb 2017.

[95] A. Porat, E. R. Andresen, H. Rigneault, D. Oron, S. Gigan, and O. Katz, "Widefield lensless imaging through a fiber bundle via speckle correlations," *Opt. Express*, vol. 24, pp. 16835–16855, Jul 2016.

[96] J. D. L. Allan W. Snyder, *Optical Waveguide Theory*. New York: Chapman and Hall, 1st ed., 1983.

[97] J. A. Buck, *Fundamentals of Optical Fibers*. New Jersey: John Wiley & Sons, 2nd ed., 2004.

[98] K. Okamoto, *Fundamentals of Optical Waveguides*. Electronics & Electrical, Burlington: Academic Press, 2006.

[99] A. Yariv and P. Yeh, *Photonics: Optical Electronics in Modern Communications*. New York: Oxford University Press, 2007.

[100] M. S. Wartak, *Computational Photonics: An Introduction with MATLAB*. New York: Cambridge University Press, 2013.

[101] A. Snyder, "Asymptotic expressions for eigenfunctions and eigenvalues of a dielectric or optical waveguide," *IEEE Transactions on Microwave Theory and Techniques*, vol. 17, no. 12, pp. 1130–1138, 1969.

[102] D. Gloge, "Weakly guiding fibers," *Appl. Opt.*, vol. 10, pp. 2252–2258, Oct 1971.

[103] J. A. Arnaud, *Beam and Fiber Optics*. New York: Academic Press, 1976.

[104] A. W. Snyder and W. R. Young, "Modes of optical waveguides," *J. Opt. Soc. Am.*, vol. 68, pp. 297–309, Mar 1978.

[105] "LP Modes." https://www.rp-photonics.com/lp_modes.html. Accessed: October 2022.

[106] S. Kahraman, "Enhancing the Resolution of Multimode Fiber Based Spectrometers," Master's thesis, Middle East Technical University, Ankara, Sep 2021.

[107] T. Pertsch, "Fiber Mode Solver (Bessel's Differential Equation)." https://www.iap.uni-jena.de/iapmedia/de/Lecture/ Computational+Photonics1538258400/CPho18_Seminar06_ Fiber_Mode_Solver.pdf. Accessed: August 2021.

[108] M. Hughes, "Fibre Mode Solver and Simulator." https://www. mathworks.com/matlabcentral/fileexchange/77497- fibre-mode-solver-and-simulator. Accessed: October 2022.

[109] R. S. Quimby, *Photonics and Lasers: An Introduction*. New Jersey: John Wiley & Sons, 2006.

[110] Y. Liang, X. Yun, M. He, Z. Wang, S. Wang, and M. Lei, "Zero-order-free complex beam shaping," *Optics and Lasers in Engineering*, vol. 155, p. 107048, 2022.

[111] M. Polin, K. Ladavac, S.-H. Lee, Y. Roichman, and D. G. Grier, "Optimized holographic optical traps," *Optics Express*, vol. 13, no. 15, p. 5831 – 5845, 2005.

[112] H. Zhang, J. Xie, J. Liu, and Y. Wang, "Elimination of a zero-order beam induced by a pixelated spatial light modulator for holographic projection," *Applied Optics*, vol. 48, no. 30, p. 5834 – 5841, 2009.

[113] M. Padgett and R. Di Leonardo, "Holographic optical tweezers and their relevance to lab on chip devices," *Lab Chip*, vol. 11, pp. 1196–1205, 2011.

[114] J. Liang, S.-Y. Wu, F. K. Fatemi, and M. F. Becker, "Suppression of the zero-order diffracted beam from a pixelated spatial light modulator by phase compression," *Applied Optics*, vol. 51, no. 16, p. 3294 – 3304, 2012.

[115] W. Improso, G. Tapang, and C. Saloma, "Suppression of zeroth-order diffraction in phase-only spatial light modulator," *Optics, Photonics and Laser Technology*, p. 1 – 30, 2017.

[116] "PLUTO-2.1 LCOS Spatial Light Modulator Phase Only (Reflective)." `https://holoeye.com/slm-pluto-phase-only/`. Accessed: November 2022.

[117] C. Maurer, A. Jesacher, S. Bernet, and M. Ritsch-Marte, "What spatial light modulators can do for optical microscopy," *Laser & Photonics Reviews*, vol. 5, no. 1, pp. 81–101, 2011.

[118] F. Difato, M. D. Maschio, R. Beltramo, A. Blau, F. Benfenati, and T. Fellin, *Spatial Light Modulators for Complex Spatiotemporal Illumination of Neuronal Networks*, pp. 61–81. New Jersey: Humana Press, 2012.

[119] Z. Zhang, Z. You, and D. Chu, "Fundamentals of phase-only liquid crystal on silicon (lcos) devices," *Light-Science & Applications*, vol. 3, 2014.

[120] Jullien, Aurélie, "Spatial light modulators," *Photoniques*, no. 101, pp. 59–64, 2020.

[121] "Spatial Light Modulators." `https://holoeye.com/spatial-light-modulators/`. Accessed: November 2022.

[122] "Understanding the jargon of LCOS Spatial Light Modulators (SLMs)." `https://photonics.laser2000.co.uk/blogs/understanding-the-`

jargon-of-lcos-spatial-light-modulators-slms/. Accessed: November 2022.

[123] I. M. Vellekoop and A. P. Mosk, "Phase control algorithms for focusing light through turbid media," *Optics Communications*, vol. 281, pp. 3071–3080, Jun 2008.

[124] Z. Fayyaz, N. Mohammadian, M. Reza Rahimi Tabar, R. Manwar, and K. Avanaki, "A comparative study of optimization algorithms for wavefront shaping," *Journal of Innovative Optical Health Sciences*, vol. 12, no. 04, p. 1942002, 2019.

[125] R. D. Leonardo and S. Bianchi, "Hologram transmission through multi-mode optical fibers," *Opt. Express*, vol. 19, pp. 247–254, Jan 2011.

[126] I. M. Vellekoop and A. P. Mosk, "Focusing coherent light through opaque strongly scattering media," *Optics Letters*, vol. 32, pp. 2309–2311, Aug 2007.

[127] D. Akbulut, T. J. Huisman, E. G. van Putten, W. L. Vos, and A. P. Mosk, "Focusing light through random photonic media by binary amplitude modulation.," *Optics Express*, vol. 19, pp. 4017–4029, 2011.

[128] Y. Ren, R. Lu, and L. Gong, "Tailoring light with a digital micromirror device," *Annalen der Physik*, vol. 527, 2015.

[129] S. Shin, K. Kim, J. Yoon, and Y. Park, "Active illumination using a digital micromirror device for quantitative phase imaging.," *Optics Letters*, vol. 40, pp. 5407–5410, 2015.

[130] M.-C. Park, B.-R. Lee, J.-Y. Son, and O. O. Chernyshov, "Properties of DMDs for holographic displays," *Journal of Modern Optics*, vol. 62, pp. 1600–1607, 2015.

[131] A. Turpin, I. Vishniakou, and J. D. Seelig, "Light scattering control in transmission and reflection with neural networks.," *Optics Express*, vol. 26, pp. 30911–30929, 2018.

[132] K. Nam and J.-H. Park, "Increasing the enhancement factor for dmd-based wavefront shaping.," *Optics Letters*, vol. 45, pp. 3381–3384, 2020.

[133] T. Zhao, S. Ourselin, T. K. M. Vercauteren, and W. Xia, "Focusing light through multimode fibres using a digital micromirror device: a comparison study of non-holographic approaches," *Optics Express*, vol. 29, pp. 14269–14281, 2021.

[134] A. B. Ayoub and D. Psaltis, "High speed, complex wavefront shaping using the digital micro-mirror device," *Scientific Reports*, vol. 11, 2021.

[135] T. G. Wong, *Introduction to Classical and Quantum Computing*. Nebraska: Rooted Grove, 2nd ed., 2022.

[136] G. Unnikrishnan and K. Singh, "Cryptography using optoelectronic techniques," in *Photonics 2000: International Conference on Fiber Optics and Photonics*, vol. 4417, pp. 178–189, SPIE, 2001.

[137] B. Javidi and J. L. Horner, "Optical pattern recognition for validation and security verification," *Optical Engineering*, vol. 33, no. 6, pp. 1752–1756, 1994.

[138] B. Javidi, "Securing information with optical technologies," *Physics Today*, vol. 50, no. 3, pp. 27–32, 1997.

[139] P. Refregier and B. Javidi, "Optical image encryption based on input plane and fourier plane random encoding," *Opt. Lett.*, vol. 20, pp. 767–769, Apr 1995.

[140] G. Unnikrishnan, J. Joseph, and K. Singh, "Optical encryption system using a spatial light modulators," in *Proc. SPIE 3740*, pp. 525–528, 1999.

[141] G. Unnikrishnan and K. Singh, "Double random fractional Fourier domain encoding for optical security," *Optical Engineering*, vol. 39, no. 11, pp. 2853–2859, 2000.

[142] B. Javidi and T. Nomura, "Securing information by use of digital holography," *Opt. Lett.*, vol. 25, pp. 28–30, Jan 2000.

[143] S. Lai and M. A. Neifeld, "Digital wavefront reconstruction and its application to image encryption," *Optics Communications*, vol. 178, no. 4, pp. 283–289, 2000.

[144] E. Tajahuerce, O. Matoba, S. C. Verrall, and B. Javidi, "Optoelectronic information encryption with phase-shifting interferometry," *Appl. Opt.*, vol. 39, pp. 2313–2320, May 2000.

[145] E. Tajahuerce and B. Javidi, "Encrypting three-dimensional information with digital holography," *Appl. Opt.*, vol. 39, pp. 6595–6601, Dec 2000.

[146] P. C. Mogensen and J. Glückstad, "A phase-based optical encryption system with polarisation encoding," *Optics Communications*, vol. 173, no. 1, pp. 177–183, 2000.

[147] P. C. Mogensen and J. Glückstad, "Phase-only optical encryption," *Opt. Lett.*, vol. 25, pp. 566–568, Apr 2000.

[148] J. A. Davis, D. E. McNamara, D. M. Cottrell, and T. Sonehara, "Two-dimensional polarization encoding with a phase-only liquid-crystal spatial light modulator," *Appl. Opt.*, vol. 39, pp. 1549–1554, Apr 2000.

[149] G. Unnikrishnan, M. Pohit, and K. Singh, "A polarization encoded optical encryption system using ferroelectric spatial light modulator," *Optics Communications*, vol. 185, no. 1, pp. 25–31, 2000.

[150] S.-Y. Yi, C.-S. Ryu, and S.-H. Lee, "Optical visual cryptography based on the phase characteristics of spatial light modulator," in *Optics and Photonics for Counterterrorism and Crime Fighting II*, vol. 6402, p. 64020A, SPIE, 2006.

[151] B. Javidi, A. Carnicer, M. Yamaguchi, T. Nomura, E. Pérez-Cabré, M. S. Millán, N. K. Nishchal, R. Torroba, J. F. Barrera, W. He, X. Peng, A. Stern, Y. Rivenson, A. Alfalou, C. Brosseau, C. Guo, J. T. Sheridan, G. Situ, M. Naruse, T. Matsumoto, I. Juvells, E. Tajahuerce, J. S. Lancis, W. Chen, X. Chen, P. W. H. Pinkse, A. P. Mosk, and A. S. Markman, "Roadmap on optical security," *Journal of Optics*, vol. 18, 2016.

[152] "2-D correlation coefficient - MATLAB." `https://www.mathworks.com/help/images/ref/corr2.html`. Accessed: November 2022.

[153] T. Čižmár and K. Dholakia, "Exploiting multimode waveguides for pure fibre-based imaging," *Nat. Commun.*, vol. 3, 2012.

[154] M. Ploschner, T. Tyc, and T. Čižmár, "Seeing through chaos in multimode fibres," *Nat. Photon.*, vol. 9, pp. 529–535, 2015.

[155] S. Aisawa, K. Noguchi, and T. Matsumoto, "Remote image classification through multimode optical fiber using a neural network," *Opt. Lett.*, vol. 16, pp. 645–647, 1991.

[156] R. K. Marusarz and M. R. Sayeh, "Neural network-based multimode fiber-optic information transmission," *Appl. Opt.*, vol. 40, pp. 219–227, 2001.

[157] R. Takagi, R. Horisaki, and J. Tanida, "Object recognition through a multi-mode fiber," *Opt. Rev.*, vol. 24, pp. 117–120, 2017.

[158] N. Borhani, E. Kakkava, C. Moser, and D. Psaltis, "Learning to see through multimode fibers," *Optica*, vol. 5, pp. 960–966, 2018.

[159] B. Rahmani, D. Loterie, G. Konstantinou, D. Psaltis, and C. Moser, "Multimode optical fiber transmission with a deep learning network," *Light Sci. Appl.*, vol. 7, 2018.

[160] P. Caramazza, O. Moran, R. Murray-Smith, and D. Faccio, "Transmission of natural scene images through a multimode fibre," *Nat. Commun.*, vol. 10, 2019.

[161] G. Cohen, S. Afshar, J. Tapson, and A. van Schaik, "Emnist: Extending mnist to handwritten letters," in *2017 International Joint Conference on Neural Networks (IJCNN)*, pp. 2921–2926, 2017.

[162] D. P. Kingma and J. Ba, "Adam: A method for stochastic optimization." arxiv:1412.6980. Published as a conference paper at the 3rd International Conference for Learning Representations, San Diego, 2015.

[163] S. Santurkar, D. Tsipras, A. Ilyas, and A. Mądry, "How does batch normalization help optimization?," in *Proceedings of the 32nd International Conference on Neural Information Processing Systems*, NIPS'18, (Red Hook, NY, USA), p. 2488–2498, Curran Associates Inc., 2018.

[164] J. C. D. Brand, *Lines of Light: The Sources of Dispersive Spectroscopy, 1800-1930.* Routledge, 1st ed., 1995.

[165] R. Łobiński, D. Schaumlöffel, and J. Szpunar, "Mass spectrometry in bioinorganic analytical chemistry," *Mass Spectrometry Reviews*, vol. 25, no. 2, pp. 255–289, 2006.

[166] J. W. Chan, D. Motton, J. C. Rutledge, N. L. Keim, and T. Huser, "Raman spectroscopic analysis of biochemical changes in individual triglyceride-rich lipoproteins in the pre- and postprandial state," *Analytical Chemistry*, vol. 77, no. 18, pp. 5870–5876, 2005.

[167] M. N. Fiddler, I. Begashaw, M. A. Mickens, M. S. Collingwood, Z. Assefa, and S. Bililign, "Laser spectroscopy for atmospheric and environmental sensing," *Sensors*, vol. 9, no. 12, pp. 10447–10512, 2009.

[168] A. Nitkowski, L. Chen, and M. Lipson, "Cavity-enhanced on-chip absorption spectroscopy using microring resonators," *Opt. Express*, vol. 16, pp. 11930–11936, Aug 2008.

[169] M. Laubscher, S. Bourquin, L. Froehly, B. Karamata, and T. Lasser, "Spectroscopic optical coherence tomography based on wavelength de-multiplexing and smart pixel array detection," *Optics Communications*, vol. 237, no. 4, pp. 275–283, 2004.

[170] T. Matsumoto, S. Fujita, and T. Baba, "Wavelength demultiplexer consisting of photonic crystal superprism and superlens," *Opt. Express*, vol. 13, pp. 10768–10776, Dec 2005.

[171] R. F. Wolffenbuttel, "Mems-based optical mini- and microspectrometers for the visible and infrared spectral range," *Journal of Micromechanics and Microengineering*, vol. 15, pp. S145–S152, 2005.

[172] L. P. Schuler, J. S. Milne, J. M. Dell, and L. Faraone, "Mems-based microspectrometer technologies for nir and mir wavelengths," *Journal of Physics D: Applied Physics*, vol. 42, 2009.

[173] M. Manley, "Near-infrared spectroscopy and hyperspectral imaging: non-destructive analysis of biological materials," *Chemical Society Reviews*, vol. 43, pp. 8200–8214, 2014.

[174] E. Ryckeboer, R. Bockstaele, M. Vanslembrouck, and R. Baets, "Glucose sensing by waveguide-based absorption spectroscopy on a silicon chip," *Biomed. Opt. Express*, vol. 5, pp. 1636–1648, May 2014.

[175] J. Malinen, A. Rissanen, H. Saari, P. Karioja, M. Karppinen, T. Aalto, and K. Tukkiniemi, "Advances in miniature spectrometer and sensor development," in *Proc. SPIE 9101, Next-Generation Spectroscopic Technologies VII*, vol. 9101, p. 91010C, SPIE, 2014.

[176] M. Ebermann, N. Neumann, K. Hiller, M. Seifert, M. Meinig, and S. Kurth, "Tunable MEMS Fabry-Perot filters for infrared microspectrometers: a review," in *Proc. SPIE 9760, MOEMS and Miniaturized Systems XV*, vol. 9760, p. 97600H, SPIE, 2016.

[177] P. S. Edwards, C. Zhang, B. Zhang, X. Hong, V. K. Nagarajan, B. Yu, and Z. Liu, "Smartphone based optical spectrometer for diffusive reflectance spectroscopic measurement of hemoglobin," *Scientific Reports*, vol. 7, 2017.

[178] A. J. S. McGonigle, T. C. Wilkes, T. D. Pering, J. R. Willmott, J. M. Cook, F. M. Mims, and A. V. Parisi, "Smartphone spectrometers," *Sensors*, vol. 18, 2018.

[179] R. A. Crocombe, "Portable spectroscopy," *Appl. Spectrosc.*, vol. 72, pp. 1701–1751, Dec 2018.

[180] M. Mazilu, T. Vettenburg, A. D. Falco, and K. Dholakia, "Random super-prism wavelength meter," *Opt. Lett.*, vol. 39, pp. 96–99, Jan 2014.

[181] P. Wang and R. Menon, "Computational spectroscopy via singular-value decomposition and regularization," *Opt. Express*, vol. 22, pp. 21541–21550, Sep 2014.

[182] T. Yang, X. L. Huang, H. P. Ho, C. Xu, Y. Y. Zhu, M. D. Yi, X. H. Zhou, X. A. Li, and W. Huang, "Compact spectrometer based on a frosted glass," *IEEE Photonics Technology Letters*, vol. 29, no. 2, pp. 217–220, 2017.

[183] M. Chakrabarti, M. L. Jakobsen, and S. G. Hanson, "Speckle-based spectrometer," *Opt. Lett.*, vol. 40, pp. 3264–3267, Jul 2015.

[184] H. Cao, "Perspective on speckle spectrometers," *Journal of Optics*, vol. 19, p. 060402, May 2017.

[185] E. G. Rawson, J. W. Goodman, and R. E. Norton, "Frequency dependence of

modal noise in multimode optical fibers," *J. Opt. Soc. Am.*, vol. 70, pp. 968–976, Aug 1980.

[186] W. Freude, C. Fritzsche, G. Grau, and L. Shan-da, "Speckle interferometry for spectral analysis of laser sources and multimode optical waveguides," *Journal of Lightwave Technology*, vol. 4, no. 1, pp. 64–72, 1986.

[187] B. Redding and H. Cao, "Using a multimode fiber as a high-resolution, low-loss spectrometer," *Opt. Lett.*, vol. 37, pp. 3384–3386, Aug 2012.

[188] B. Redding, S. M. Popoff, and H. Cao, "All-fiber spectrometer based on speckle pattern reconstruction," *Opt. Express*, vol. 21, pp. 6584–6600, Mar 2013.

[189] B. Redding, S. F. Liew, R. Sarma, and H. Cao, "Compact spectrometer based on a disordered photonic chip," *Nature Photonics*, vol. 7, pp. 746–751, Jul 2013.

[190] B. Redding, M. Alam, M. Seifert, and H. Cao, "High-resolution and broadband all-fiber spectrometers," *Optica*, vol. 1, pp. 175–180, Sep 2014.

[191] B. Redding, S. M. Popoff, Y. Bromberg, M. A. Choma, and H. Cao, "Noise analysis of spectrometers based on speckle pattern reconstruction," *Appl. Opt.*, vol. 53, pp. 410–417, Jan 2014.

[192] N. H. Wan, F. Meng, T. Schröder, R.-J. Shiue, E. H. Chen, and D. Englund, "High-resolution optical spectroscopy using multimode interference in a compact tapered fibre," *Nature Communications*, vol. 6, p. 7762, 2015.

[193] S. F. Liew, B. Redding, M. A. Choma, H. D. Tagare, and H. Cao, "Broadband multimode fiber spectrometer," *Opt. Lett.*, vol. 41, pp. 2029–2032, May 2016.

[194] B. Redding, S. F. Liew, Y. Bromberg, R. Sarma, and H. Cao, "Evanescently coupled multimode spiral spectrometer," *Optica*, vol. 3, pp. 956–962, Sep 2016.

[195] N. Coluccelli, M. Cassinerio, B. Redding, H. Cao, P. Laporta, and G. Galzerano, "The optical frequency comb fibre spectrometer," *Nature Communications*, vol. 7, Oct 2016.

[196] M. N. Zervas, "Chapter 1 - Advances in Fiber Distributed-Feedback Lasers," in *Optical Fiber Telecommunications (Sixth Edition)* (I. P. Kaminow, T. Li, and

A. E. Willner, eds.), Optics and Photonics, pp. 1–24, Boston: Academic Press, 6th ed., 2013.

[197] E. Yüce and S. Kürekci, "Compact holographic slm spectrometer," Pending-patent, Turkish Patent and Trademark Office application number: 2020/22701. International application number: PCT/TR2021/051613.

[198] Z. Xu, Z. Wang, M. E. Sullivan, D. J. Brady, S. H. Foulger, and A. Adibi, "Multimodal multiplex spectroscopy using photonic crystals," *Opt. Express*, vol. 11, pp. 2126–2133, Sep 2003.

[199] T. W. Kohlgraf-Owens and A. Dogariu, "Transmission matrices of random media: means for spectral polarimetric measurements," *Opt. Lett.*, vol. 35, pp. 2236–2238, Jul 2010.

[200] E. Yüce and S. Kürekci, "Interference-based spectrometer with multi-mode medium," Pending-patent, International application number: PCT/TR2021/051305.

[201] D. Takhar, J. N. Laska, M. B. Wakin, M. F. Duarte, D. Baron, S. Sarvotham, K. F. Kelly, and R. G. Baraniuk, "A new compressive imaging camera architecture using optical-domain compression," in *Proc. SPIE 6065, Computational Imaging IV*, vol. 6065, p. 606509, SPIE, Feb 2006.

[202] M. F. Duarte, M. A. Davenport, D. Takbar, J. N. Laska, T. Sun, K. F. Kelly, and R. G. Baraniuk, "Single-pixel imaging via compressive sampling," *IEEE Signal Processing Magazine*, vol. 25, pp. 83–91, 2008.

[203] P. Gattinger, I. Zorin, C. Rankl, and M. Brandstetter, "Spectral-coding-based compressive single-pixel nir spectroscopy in the sub-millisecond regime," *Sensors*, vol. 21, p. 5563, Aug 2021.

[204] M. P. Edgar, G. M. Gibson, and M. J. Padgett, "Principles and prospects for single-pixel imaging," *Nature Photonics*, vol. 13, pp. 13–20, Dec 2019.

[205] I. M. Vellekoop, E. G. van Putten, A. Lagendijk, and A. P. Mosk, "Demixing light paths inside disordered metamaterials," *Optics Express*, vol. 16, pp. 67–80, Jan 2008.

[206] I. M. Vellekoop, "Feedback-based wavefront shaping," *Optics Express*, vol. 23, pp. 12189–12206, May 2015.

[207] S. Donati, *Photodetectors: Devices, Circuits and Applications*. New Jersey: Wiley-IEEE Press, 2nd ed., 2021.

[208] M. Xia, D. Li, L. Wang, and D. Wang, "Fast optical wavefront engineering for controlling light propagation in dynamic turbid media," *Journal of Innovative Optical Health Sciences*, vol. 12, no. 04, p. 1930007, 2019.

[209] Q. Hang, B. Ung, I. Syed, N. Guo, and M. Skorobogatiy, "Photonic bandgap fiber bundle spectrometer," *Applied Optics*, vol. 49, pp. 4791–4800, Sep 2010.

[210] Q. Wei, L. Huang, T. Zentgraf, and Y. Wang, "Optical wavefront shaping based on functional metasurfaces," *Nanophotonics*, vol. 9, no. 5, pp. 987–1002, 2020.

[211] Y. Guo, Y. Guo, C. Li, H. Zhang, X. Zhou, and L. Zhang, "Integrated optical phased arrays for beam forming and steering," *Applied Sciences*, vol. 11, no. 9, 2021.

CURRICULUM VITAE

EDUCATION

■ M.Sc. in Physics   Middle East Technical University   **2013-2015**
CGPA: 3.81/4.00

   – **Thesis Title:** Basics of Spin-2 Theories

   – **Advisor:** Prof. Dr. Bayram Tekin

■ B.Sc. in Physics   Middle East Technical University   **2008-2013**
CGPA: 3.78/4.00

   – **Graduation Project:** Quantum Hall Effect in Noncommutative Space

   – **Advisor:** Prof. Dr. Seçkin Kürkçüoğlu

WORK EXPERIENCE

■ Teaching Assistant   Middle East Technical University   **2017-ongoing**

General Physics I & II (First-year courses for engineering students)

   – tutoring, lab coordination

Physics I & II (First-year courses for physics students)

   – homework grading, problem solving

Applied Modern Physics Laboratory (Third-year course for physics students)

   – experiment supervision, lab coordination

Electromagnetism (Third-year course for physics students)

   – homework grading

Classical Mechanics I & II (Third-year courses for physics students)

- homework grading

Quantum Mechanics I (Fourth-year course for physics students)

- homework grading

Electromagnetism I (Graduate-level course for physics students)

- homework grading, problem solving

Quantum Mechanics I (Graduate-level course for physics students)

- homework grading

■ Tutoring Assistant   Middle East Technical University   **2012-2013**

Mathematical Methods in Physics (Second-year course for physics students)

- homework grading, problem solving

■ PC Lab Assistant   Middle East Technical University   **2011-2012**

HONORS, AWARDS, FELLOWSHIPS

■ Best poster prize (2nd place) in *FOTONİK 2022 – National Optics, Electro-Optics, and Photonics Workshop*	**2022**
■ Ranked 1st in the graduating class	**2013**
■ Enrolled in High Honor Roll five times	**2008-2013**
■ Enrolled in Honor Roll one time	**2008-2013**

TECHNICAL SKILLS

■ Technical Computing, Simulation	**Matlab, Mathematica, Python**
■ Technical Drawing	**Powerpoint, Inkscape**
■ Operating Systems	**Windows, Linux**
■ Other Software	**MS Office, LaTeX**

PUBLICATIONS & PREPRINTS

- **S. Kürekci**, S. S. Kahraman, and E. Yüce, "Single-Pixel Multimode Fiber Spectrometer via Wavefront Shaping," arXiv.2210.13292 [Preprint]

- **S. Kürekci**, A. T. Temür, M. E. Odabas, G. Afshari, and E. Yüce, "Deep learning-based image transmission through a multi-mode fiber," Proc. SPIE 11351, Unconventional Optical Imaging II, 1135126 (2020)

- G. D. Ozen, **S. Kürekci**, and B. Tekin, "Entropy in Born-Infeld Gravity," Phys. Rev. D, 96, 124038 (2017)

PATENTS

- E. Yüce, and **S. Kürekci**, "Interference-based spectrometer with multimode medium," (Pending-patent, International application number: PCT/TR2021/051305)

- E. Yüce, and **S. Kürekci**, "Compact Holographic SLM Spectrometer," (Pending-patent, Turkish Patent and Trademark Office application number: 2020/22701. International application number: PCT/TR2021/051613)

CONFERENCE PRESENTATIONS

- **S. Kürekci**, and E. Yüce, "Single-Pixel, Picometer Scale Spectral Characterization of Light Through Scattering Media," NANOTR-16 - 16th Nanoscience & Nanotechnology Conference (2022)

- **S. Kürekci**, A. T. Temür, M. E. Odabas, G. Afshari, and E. Yüce, "Deep learning-based image transmission through a multi-mode fiber," Unconventional Optical Imaging II (2020)

POSTER PRESENTATIONS

- **S. Kürekci**, S. S. Kahraman, and E. Yüce, "Picometer-Resolution Single-Pixel Spectrometer Across Scattering Media," FOTONİK 2022 - Ulusal Optik, Elektro-Optik ve Fotonik Çalıştayı

- **S. Kürekci**, A. T. Temür, M. E. Odabaş, and E. Yüce, "Deep Learning Image Transmission Through a Multi-mode Fiber," FOTONİK 2019 - 21. Ulusal Optik, Elektro-Optik ve Fotonik Çalıştayı

- G. Afshari, **S. Kürekci**, and E. Yüce, "Improving Fiber Bend Sensor via Wavefront Shaping," FOTONİK 2019 - 21. Ulusal Optik, Elektro-Optik ve Fotonik Çalıştayı

- **S. Kürekci**, C. Yeşil, G. Afshari, M. Tabak, and E. Yüce, "Focusing Light Through Scattering Medium," FOTONİK 2018 - 20. Ulusal Optik, Elektro-Optik ve Fotonik Çalıştayı